Nanosecond Laser Processing of a Zr-based Bulk Metallic Glass for Potential Orthopaedic Implant Applications

Yang Jiao

School of Engineering

Cardiff University

This thesis is submitted in fulfilment of the requirement of the degree of

Doctor of Philosophy

April 2020

Abstract

With continuously improving living standards, the demand for biomaterials in orthopaedic implant applications has increased substantially in recent years. Bulk metallic glasses (BMGs) have recently emerged as promising candidate biomaterials due to their unique mechanical and chemical properties as well as attractive processing capabilities, which result from their amorphous nature. A number of studies exploring the bio-compatibility of BMGs have been reported in the literature, the outcome of which has generally shown the potential of Zr-based, Mg-based and Ti-based BMGs for bio-medical applications. At the same time, surface treatments have also been successfully used on traditional biomedical alloys, especially titanium alloys, to further enhance their bio-compatibility. In this context, the focus of this Thesis was on applying a number of nanosecond (ns) laser surface processing techniques on a specific type of Zr-based BMG, also known as Vitreloy 105, to investigate the potential of this combination of material and surface treatments for the development of a new candidate biomaterial.

In the first part of the thesis, reported in Chapter 4, a 2D theoretical model was developed to simulate the thermal history within a Vitreloy 105 workpiece in the context of multiple and moving ns pulses irradiation. In particular, the model was used to predict the ablated feature dimensions and to reveal possible thermal events occurring during the laser micromachining process that could explain the formation of the resulting topography. The combined experimental and theoretical approach also enabled the identification of a suitable set of laser parameters with respect to the process efficiency over a range of pulse durations, fluence values, scanning speeds and track distances between machined grooves.

In the second part of the thesis, which is the focus of Chapter 5 and 6, laser surface texturing was employed to fabricate two types of surface patterns, dimple and groove, to study the resulting wettability of Vitreloy 105, and associated bio-compatibility characteristics. Firstly, the effect of different laser parameters, including laser fluence, scanning speed, surface texture type and track distance, on the wettability of this BMG was investigated. Following this, through *in-vitro* cell culture experiments, the bio-compatibility of Vitreloy 105 samples with different surface textures was assessed. The underlying mechanism associated with laser surface texturing which affected the *in-vitro* bio-compatibility of the material was discussed based on the laser-induced modifications to surface chemistry and surface roughness. In line with the obtained wettability results, the bio-compatibility findings showed that cells on groove-textured surfaces had a higher viability and better adhesion compared to those on the as-cast and dimple-textured surfaces. Moreover, it was also found that cells aligned along the direction of laser-induced groove patterns.

In the last part of the thesis, presented in Chapter 7, it was confirmed that laser surface melting (LSM) could be employed to modify the hardness and the shear banding behaviour of Vitreloy 105. More specifically, by conducting ns LSM operations in ambient atmosphere, it was found that surface hardening could be achieved, in addition to the well-known surface softening effect. In addition, it was found that the presence of compressive residual stress and an increased introduction of crystalline precipitates accompanied LSM-induced surface hardening. On the contrary, tensile residual stress and a reduced fraction of crystalline precipitates were observed for the softened surface post-LSM. Finally, differences in shear-banding mechanisms were detected near the surface of the laser irradiated regions. More specifically, overall reduced serrated flow but important surface shear bands events were observed following the LSM-based introduction of compressive residual stress. In contrast, more pronounced serrated

flows and the likely distribution of shear banding activity well beneath the irradiated BMG surface was promoted when LSM resulted in the introduction of tensile residual stress.

Overall, the results reported in this thesis suggest that nanosecond laser-based surface micromachining, texturing and melting represent promising methods for promoting the potential application of Vitreloy 105 as orthopaedic implants.

Acknowledgements

Firstly, I would like to express my sincere gratitude to my supervisors, Dr Emmanuel Brousseau, Dr Hanxing Zhu and Dr Samuel Bigot for giving me this opportunity to further my PhD study at Cardiff University. Particularly, I would like to thank my first supervisor, Dr Emmanuel Brousseau, for his valuable guidance, unquestionable support, his rigorous academic attitude and his constant encouragements, which has helped me bring it to a completion. Dr Emmanuel Brousseau not only provides me with a good experimental platform to conduct my research at Cardiff University but also helps me establish cooperative relationships with other universities and research institutes to finish the relevant experiments.

I would also like to thank Prof. Weifeng He, Prof. Jiwang Yan, Prof. Hu Huang, Mr Xiaoxiang Wang, Mr Koji Kosai, Mr Xiaojun Shen and Dr Alexander Lunt for their help with the XPS analysis and nanoindentation test as well as the wettability and FIB-DIC based residual stress measurements. My gratitude also extends to the Dentistry School of Cardiff University, in particular, Dr Wayne Nishio Ayre and Mr Edward Gait-Carr for their assistance with the cell culture experiment. Dr Quanquan Han is gratefully appreciated for his assistance with the SEM experiments and discussions about the results. In addition, I gratefully appreciate the financial support from Chinese Government and Cardiff University.

Last but not least, I would like to thank my parents and my brother for their unconditional support and endless love. A special thanks to my wife, Mrs Yiwei Zhao, for her constant love, support, thoughtfulness and encouragements. I cannot imagine that I can finish my PhD study without their constant support.

List of Publications

Journal Publications directly related to the work reported in the Thesis

- **Yang Jiao**, Emmanuel Brousseau, Quanquan Han, Hanxing Zhu and Samuel Bigot. “Investigations in nanosecond laser micromachining on the $Zr_{52.8}Cu_{17.6}Ni_{14.8}Al_{9.9}Ti_{4.9}$ bulk metallic glass: experimental and theoretical study.” *Journal of Materials Processing Technology* 273 (2019): 116232.

- **Yang Jiao**, Emmanuel Brousseau, Xiaojun Shen, Xiaoxiang Wang, Quanquan Han, Hanxing Zhu, Samuel Bigot, Weifeng He. “Investigations in the fabrication of surface patterns for wettability modification on a Zr-based bulk metallic glass by nanosecond laser surface texturing.” *Journal of Materials Processing Technology* (2020) (Accepted).

- **Yang Jiao,** Emmanuel Brousseau, Wayne Nishio Ayre, Edward Gait-Carr, Xiaojun Shen, Xiaoxiang Wang, Samuel Bigot, Hanxing Zhu, Weifeng He. “*In vitro* bio-compatibility of a Zr-based metallic glass modified by laser surface texturing for potential orthopaedic and dental applications.” (In preparation).

- **Yang Jiao,** Emmanuel Brousseau, Koji Kosai, Alexander Lunt, Jiwang Yan, Quanquan Han, Hanxing Zhu, Samuel Bigot, Weifeng He. “Nanosecond laser-induced softening and hardening in a Zr-based bulk metallic glasses.” (In preparation).

Journal Publications associated with the wider laser processing work achieved:

- **Yang Jiao**, Weifeng He and Xiaojun Shen. “Enhanced high cycle fatigue resistance of Ti-17 titanium alloy after multiple laser peening without coating.” *International Journal of Advanced Manufacturing Technology* 104 (2019): 1333-1343.

- Quanquan Han, **Yang Jiao**. “Effect of heat treatment and laser surface remelting on AlSi10Mg alloy fabricated by selective laser melting.” *International Journal of Advanced Manufacturing Technology* 102 (2019): 3315 -3324.

Conference Publications

- **Yang Jiao,** Emmanuel Brousseau, Hanxing Zhu and Samuel Bigot. “Investigation of microstructural changes in a Zr-based amorphous alloy with nanosecond laser surface melting.” Presented at: *19th International Symposium on Laser Precision Microfabrication*, Edinburgh, UK, 25-28 June 2018.

Contents

List of figures

List of tables

List of abbreviations

BMGs	Bulk Metallic Glasses
2D	Two-dimensional
3D	Three-dimensional
PBS	Phosphate-buffered Solution
SBF	Simulated Body Fluids
HAECs	Human Aortic Endothelial Cells
FIB	Focussed Ion Beam
LST	Laser Surface Texturing
LSM	Laser Surface Melting
BSE	Backscattered Electron
SE	Secondary Electron
GFA	Glass Forming Ability
XRD	X-ray Diffraction
AFM	Atomic Force Microscope
DSC	Differential Scanning Calorimetry
SEM	Scanning Electron Microscope
EDX	Energy Dispersive X-ray
XPS	X-ray photoelectron spectroscopy
EDM	Electrical Discharge Machining

MOPA	Master Oscillator Power Amplifier
MRR	Material Removal Rate
VSI	Vertical Scanning Interferometry
SCA	Static Contact Angle
DD water	Distilled-deionized Water
SFE	Surface Free Energy
OWRK	Owens-Wendt-Rabel-Kaeble
DIC	Digital Image Correlation
α-MEM	Alpha Minimum Essential Medium
FBS	Fetal Bovine Serum
CCK-8	Cell Counting Kit-8
TBS	Tris Buffered Saline
RT	Room Temperature
FE	Finite Element
KH	Kelvin-Helmholtz
SLR	Supercooled Liquid Region
LPBF	Laser Powder Bed Fusion
GT	Groove Textured
DT	Dimple Textured
AC	As-Cast
OD	Optical Density
FE-SEM	Field Emission Scanning Electron Microscope

Nomenclature

A	Distance between two successive laser pulses
ρ	Density
T_g	Glass Transition Temperature
T_x	Crystallization Temperature
T_m	Melting Point
R_c	Critical cooling rate
E	Young's modulus
G	Shear modulus
B	Bulk modulus
v	Poisson's ratio
M	Molar mass
H_v	Vickers's Hardness
C_p	Specific Heat Capacity
k	Thermal Conductivity
h_a	Heat transfer coefficient
ε	Emissivity
α	Absorption coefficient
R	Reflectivity
E_{max}	Maximum pulse energy

L	Length of the cavity
W	Width of the cavity
d	Depth of a removed layer
$t_{processing}$	Total processing time
N_{pulses}	Number of tracks in one layer
N_{pulses}	Number of pulses for one track
D_s	Track distance between two adjacent laser tracks
V	Scanning speed
f	Pulse repetition frequency
θ_c	Equilibrium contact angle
γ_S	Surface free energy of the solid
γ_{SL}	Interfacial tension between the solid and liquid phase
γ_L	Surface tension of the liquid
γ_S^d	Dispersive component of the solid SFE
γ_S^p	Polar component of the solid SFE
γ_L^d	Dispersive part of the surface tension for testing liquids
γ_L^p	Polar part of the surface tension for testing liquids
γ^T	Total surface free energy
γ^p	Sum of polar components
γ^d	Sum of dispersive components
W_a	Work of adhesion

F	Vickers indentation loads
D	Mean value of two indentation diagonal lengths
P_0	Peak output intensity of the pulsed laser
x	Coordinate along the surface of the irradiated material
x_0	Centre of the laser spot
r	Radius of the laser beam at the focal point
t_0	The time at which the pulse starts
t_p	Full duration of the pulse at half maximum
z	Coordinate along the depth
q_a	Heat flux
F	Fluence
S_a	Surface roughness
E_{pit}	Pitting potentials

Chapter 1 Introduction

1.1 Motivation

With continuously improving living standards, the demand for biomaterials in orthopaedic implant applications has increased substantially in recent years (Li and Zheng, 2016). It was reported that millions of hard-tissue replacement and repair surgeries were carried out in the United States alone annually within the time period from 1990s to 2010s (Demetriou et al., 2010). Despite the high success rate of such surgical operations, there still remains a number of associated issues. For example, 7% of patients have to receive a second revision surgery 10 years after the original operation. With an aging population, the revision rate is growing at an accelerated rate of approximately 60% (Hallab et al., 2004). Currently, crystalline metallic alloys, such as titanium alloys, stainless steel, cobalt alloys or magnesium alloys are widely used for the fabrication of orthopaedic implants (Kaiser et al., 2015). However, improvements on existing solutions are still sought out to address a number of issues. These include Young's modulus mismatch-induced stress shielding (Long et al., 2018), fracture failure (Igarashi and Afrashtehfar, 2018) and degradation or abrasion-induced inflammation (Demetriou et al., 2010). As a result, a risk exists for patients, who have already received implant surgeries, to require another replacement surgery eventually, which has associated negative consequences in terms of pain and cost. In order to eliminate the need for further surgery and reduce the infection risks for patients, exploring novel biomaterials with high bio-compatibility and suitable mechanical properties

is important for both material scientists and clinical surgeons. In this context, bulk metallic glasses (BMGs), which display unique mechanical and chemical properties as well as attractive processing capabilities, have been proposed as promising candidate materials for orthopaedic implants, cardiovascular stent and surgical devices (Meagher et al., 2016).

BMGs, especially the family of Zr-based compositions, one of which being the focus of this study, exhibit excellent mechanical properties, such as high yield strength, high hardness, good wear resistance and excellent corrosion resistance as well as good glass forming ability (GFA). Such BMGs could provide solutions for the problems encountered by crystalline metallic biomaterials (Löffler, 2003; Schroers et al., 2009). However, some issues still remain to be addressed for the actual application of Zr-based BMGs as biomedical implants and devices. Firstly, micro-scale biomedical implants, such as cardiovascular stents and dental fixation screws, require high-precision machining, while their brittle and hard nature mean that they are difficult-to-machine materials, as is the case with most BMGs. In this context pulsed nanosecond (ns) laser processing is considered as a suitable method for micro-scale fabrication operations on BMGs. In addition to the fact that lasers are particularly suited for difficult-to-machine materials, the general advantageous features of short pulsed lasers include high resolution, localised heat input, cost efficiency and high flexibility (Yu et al., 2019). Therefore, one initial motivation behind this work, is concerned with understanding the interaction between a ns pulsed beam and a specific type of Zr-based BMG, namely Vitreloy 105, in a micro-scale machining context. This particular Zr-based amorphous alloy, with nominal composition of $Zr_{52.5}Cu_{17.9}Ni_{14.6}Al_{10.0}Ti_{5.0}$ (at%), is selected as the BMG of choice in the context of this Thesis because it contains neither toxic elements nor precious metals and exhibits excellent fatigue characteristics among most BMGs. The laser system used is a 20 W pulsed Yb-doped fibre laser. Secondly, when considering BMGs as implant materials, improving their bio-

compatibility with tissues is a key factor since the reaction of implants with the host tissue determines their long-term performance. It has been demonstrated (Kumari et al., 2015; Pfleging et al., 2015; Shen et al., 2019) that bio-compatibility depends on surface properties, including chemical composition, surface topography and wettability, to a great extent. Therefore, achieving suitable surface properties is critical to improve the bio-compatibility of implants. In this context, the development of engineering techniques to tune the properties of BMG surfaces constitute an important research topic. Laser surface texturing has become an effective method to achieve this, and hence to enhance the bio-compatibility of crystalline metallic alloys (Hsiao et al., 2016). In this context, a second important motivation behind the research reported is to employ the available ns fibre laser system to modify the surface properties (i.e. surface wettability, surface topography and surface chemistry) of a Vitreloy 105 workpiece, with the aim to enhance its bio-compatibility. Finally, the unique atomic structure of BMGs generally leads to brittleness and low plasticity, which seriously impede their applications as load-bearing structural orthopaedic implants and biomedical devices. In this context, the third motivation behind the present study is to employ the ns laser surface melting to modify the mechanical properties of Vitreloy 105, and particularly its resulting hardness and shear banding behaviours.

All these three motivations behind the work reported in this Thesis are ultimately focussed at investigating whether Vitreloy 105 could be suggested as a potential biomedical material for orthopaedic implant applications in a scenario where ns laser-based surface processing is applied on as-cast near net-shape Vitreloy 105 components.

1.2 Research aims and objectives

As introduced above, this study proposes to employ a nanosecond fibre laser system for conducting a number of processing operations, i.e. laser micromachining, laser surface texturing (LST) and laser surface melting (LSM), on Vitreloy 105 with the overall aim to investigate whether the potential biomedical application of this Zr-based BMG as orthopaedic implant can be enhanced. The specific objectives of this research include:

I. To study the material response of Vitreloy 105 under single and multiple moving laser pulses using experimental and numerical simulation methods with a view to optimise the laser parameters for micromachining.

II. To investigate the evolution of wettability of as-cast Vitreloy 105 surfaces following ns LST and explore the associated driving mechanisms behind the modification of the original wettability.

III. To investigate the feasibility of using ns LST as a method to improve the *in-vitro* bio-compatibility of Vitreloy 105 surfaces, and explore underlying mechanisms responsible for bio-compatibility enhancement from the perspective of resulting surface chemistry, topography and wettability.

IV. To investigate the evolution of the hardness and surface shear banding behaviour of Vitreloy 105 post-LSM with different laser parameters, and also to investigate associated modification mechanisms based on the residual stress distribution and microstructure changes induced by LSM.

1.3 Outline of the thesis

The remaining chapters of this thesis are organised as follow:

Chapter 2: this chapter reviews the relevant literature about the development of bulk metallic glasses and their biomedical applications, especially Zr-based bulk metallic glasses. The use of laser processing techniques, i.e. laser micromachining, laser surface texturing, laser surface melting, on bulk metallic glasses to promote their biomedical applications are also discussed. Finally, several knowledge gaps in the specific field of laser processing of bulk metallic glasses are presented.

Chapter 3: this chapter presents details about the employed Vitreloy 105 BMG materials, the experimental methods as well as the relevant experimental equipment used in this study.

Chapter 4: this chapter addresses the first objective of the work by investigating the material response under laser irradiation by single and multiple moving pulses. A 2D theoretical model is developed to predict the thermal behaviour within the material, including the transient temperature distribution and also, the laser-machined single crater size. In addition, the temperature evolution is used to explain the underlying material removal mechanism and optimise laser parameters for micromachining.

Chapter 5: this chapter addresses the second objective. Its focus is on the study of the wettability evolution of Vitreloy 105 surfaces processed with different laser parameters and textures. The influence of two texture types and laser parameters on the surface topography is discussed first. The surface chemistry of the Zr-based BMG before and after LST is also discussed using EDX and XPS measurements. Importantly, the mechanisms driving the laser-induced wettability modification are discussed based on the measured changes in surface topography and surface chemistry.

Chapter 6: this chapter addresses the third objective. It reports the investigation into the response of human MG-63 osteoblast-like cells on Vitreloy 105 surfaces modified with the considered two different laser-induced textures. This chapter also

discusses the effects of surface chemistry, roughness and wettability change before and after laser surface texturing on the observed cellular behaviour.

Chapter 7: this chapter addresses the last objective. It presents a study investigating the influence of laser surface melting on the evolution of surface mechanical properties of Vitreloy 105, namely hardness, residual stress and shear banding behaviour under nanoindentation. The influence of the surface residual stress distribution and the microstructure evolution on the resulting surface hardness and shear banding behaviour of the Zr-based BMG post-LSM is also discussed.

Chapter 8: This chapter highlights the conclusions and contributions of this Thesis. Recommendations for further work are also presented.

Chapter 2 Literature Review

In order to accomplish the research objectives described in Chapter 1, familiarity with a wide range of research backgrounds, including bulk metallic glasses, laser processing techniques, microstructure characterisation, mechanical property measurements, and *in-vitro* bio-compatibility evaluation procedures, are required. Therefore, a review of the current literature on BMGs and their biomedical applications together with the application of laser micromachining, laser surface texturing and laser surface melting on BMGs is presented in this chapter. This first section introduces the development of BMGs, especially the Zr-based family, and related biomedical applications. Next, the implementation of different laser processing techniques, including laser micromachining, laser surface texturing and laser surface melting, on BMGs are reviewed. The Chapter concludes by the presentation of the knowledge gaps identified, particularly in relation to the application of laser processing techniques for enhancing the potential of BMGs, and more specifically Vitreloy 105, for biomedical applications.

2.1 Bulk metallic glasses and related biomedical applications

2.1.1 General review

Since being firstly discovered in the early 1990s, BMGs in metal-metal systems have received sustained attention from the research community during the past few decades as a result of their combined desirable physical and mechanical properties (Liaw and Miller, 2008). As the name implies, BMGs are amorphous

alloys made of metallic elements, thus combining the microstructures of conventional amorphous glasses and the chemical compositions of the conventional crystalline metallic alloys. As a result, these alloys display a unique atomic structure that features a lack of long-range order and which results in the absence of crystal defects and grain boundaries. These specific characteristics lead to BMGs exhibiting the desirable properties, such as high strength (Löffler, 2003), relatively low Young's modulus (Bian et al., 2001), high hardness (Telford, 2004), good wear resistance (Ashby and Greer, 2006) and excellent corrosion resistance (Liu et al., 2006; Morrison et al., 2004) as well as high elastic limit (Li and Zheng, 2016). These unique properties could potentially address the problems associated with the utilisation of traditional metallic alloys for biomedical applications, ranging from orthopaedic, cardiovascular and dental implants to surgical devices (Li and Zheng, 2016). More specifically, Figure 2.1 and Table 2.1 shows the compressive strength and elastic modulus (Young’s modulus) for the biomedical use of metallic alloys, cortical bone and bulk metallic glasses. It can be seen that the metallic glasses have high strength and low Young’s modulus. With such low Young’s modulus (closer to cortical bone), the stress concentration and also the stress shielding effects can be avoided to a certain degree. As a result, such implants could achieve a longer service life after the implantation in the human’s body. With the high strength, smaller and thinner biomedical implants are possible, and thus leading to less rejection effects from the host tissues. In addition, the lack of grains makes the cutting of extremely sharp edges possible for surgical blades (Meagher et al., 2016). Furthermore, the high hardness and good wear resistance of BMGs would also benefit applications as cardiovascular stent materials (O’Brien and Carroll, 2009).

Table 2.1: Mechanical properties of potential biomedical materials (Li et al., 2017; Meagher et al., 2016).

Properties	Cortical bone	MgZnCa BMGs	Crystalline Mg alloys	Ti-6Al-4V	Stainless steel
Density (g cm^{-3})	1.8-2.1	2.0-2.8	1.74-2.2	4.4-4.5	7.9-8.1
Elastic modulus (GPa)	3-30	22-50	41-45	110-117	189-205
Compressive yield strength (MPa)	130-180	400-1190	100-560	758-1117	170-310
Fracture toughness ($MPa^{1/2}$)	3-6	NA	NA	55-115	50-200

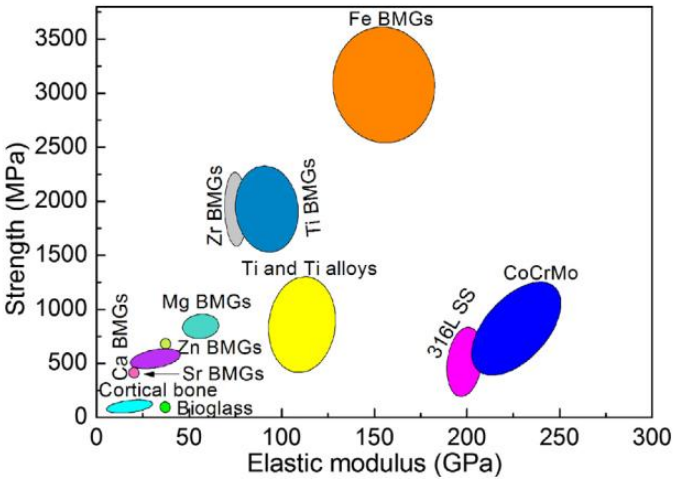

Figure 2.1: Mechanical comparisons of conventional glasses, metallic alloys and the BMGs (Li and Zheng, 2016).

During the past decades, numerous research studies have been conducted on the development of new metallic glasses for different biomedical application backgrounds, such as surgical devices (Tsai et al., 2012), orthopaedic implants (Horton and Parsell, 2002) and cardiovascular stents (Huang et al., 2015). According to the function of these BMGs, they can be categorised into two groups, biodegradable and non-biodegradable materials. To be more specific, the Mg-based, Ca-based, Zn-based and Sr-based metallic glasses were developed as

potential biodegradable materials based on the nutritional functions of the main alloying elements Mg, Ca and Sr. These biodegradable materials can be used for the manufacturing of the temporary implants and devices for some clinical cases, such as bone fracture and cardiovascular diseases, in which the fixation or mechanical support are temporarily needed during the healing process of the bones or tissues. After the healing process, these implants do not need to function in the human body anymore. Previously, a second surgery was always done to remove the fixation implants, which can bring pain and economic pressure to the patients and their families. However, with biodegradable materials, implants can be degraded into metallic ions and these metallic ions can be absorbed by the human body. Figure 2.2 shows the radiographs of mice distal femora with and without implanted high-entropy Ca-Mg-Zn-Sr-Yb alloy, immediately after implantation, and 4 weeks postoperatively. It is shown that there is no gas formation, no inflammation, and enhanced circumferential osteogenesis in the implanted bone (yellow arrow), indicating the new bone formation (Li et al., 2013a).

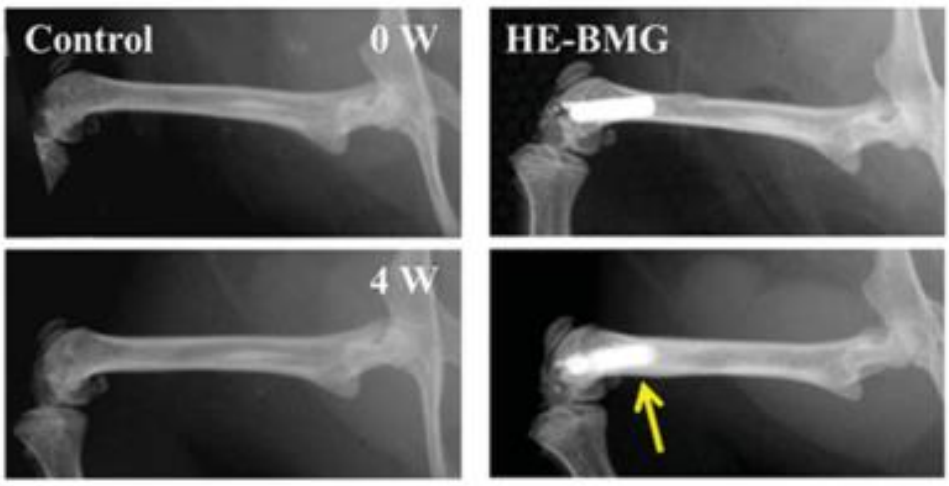

Figure 2.2: Radiographs of mice distal femora with and without implanted high-entropy CaMgZnSrYb alloy, immediately after implantation, and 4 weeks postoperatively (Li et al., 2013a).

The considered non-biodegradable BMG materials for biomedical applications mainly include the Ti-based, Zr-based and Fe-based compositions, for the long-term use of implants and devices. Figure 2.3 shows examples of biomedical devices made from BMGs, including surgical blades coated with a BMG film (Tsai et al., 2012), medical stapling anvils and minimally invasive medical devices made from BMGs (Li and Zheng, 2016). With amorphous coatings, the lack of grain boundaries makes the cutting of extremely sharp edges possible for surgical blades. Moreover, the superior surface finish, excellent manufacturing processing ability and enhanced durability can make BMGs good candidate materials for medical stapling and minimally invasive medical devices. In addition, these non-biodegradable BMGs can also be used for prosthetic replacements for human bone due to their excellent mechanical properties. For any candidate biomedical material, bio-compatibility plays a very important role, which is described as the non-acceptable degree of harm for the hosting tissue to the material. It mainly depends on two factors, the cell-biological activity of implants and the material degradation in the human body. The higher bioactivity of the implant material could lead to the higher bio-compatibility of the implant with the surrounding tissues. The material degradation rate is related to the wear and corrosion resistance of the material, which could result in the release of metallic ions and particles into the human body causing damage to organs and the blood circulatory system. The three kinds of non-biodegradable BMG compositions mentioned earlier have their own advantages and disadvantages. Compared to Ti-based and Zr-based BMGs, Fe-based compositions have lower costs, which makes them quite attractive for any large-scale biomedical applications. Since Zr element is recognised as a bio-compatible element and is the main constituent element of Zr-based BMGs, these tend to have relatively good bio-compatibility. In addition, Zr-based BMGs are the most developed and investigated glass-forming system, and their properties have been widely reported. In the following sections, the literature review is conducted

on the development of Zr-based BMGs and their applications as orthopaedic implants and biomedical devices.

(a) (b) (c)

Figure 2.3: Illustrations of biomedical devices made from BMGs. (a) surgical blades coated with amorphous metallic film; (b) medical stapling anvils; (c) Minimally invasive medical devices (Li and Zheng, 2016; Tsai et al., 2012).

2.1.2 Zr-based bulk metallic glasses

Due to the limitation associated with the critical glass-forming ability of amorphous alloys, the size of metallic glasses discovered before the late 1980s was less than 1 cm. However, with the discovery of the multicomponent Zr-based BMGs by Inoue et al. (1989), the critical casting thickness was increased to 1 cm or more. Soon afterwards, Peker and Johnson (1993) developed a new Zr-based BMG with the composition of $Zr_{41.2}Ti_{13.8}Cu_{12.5}Ni_{10.0}Be_{22.5}$ under the financial support of US Department of Energy and NASA. With the help of silica containers, a critical casting thickness of up to 10 cm became possible. This amorphous alloy became known as Vitreloy 1 (Vit 1) and was the first commercialised BMG. Since the toxic element beryllium is present in his composition, it is not suitable as a biomedical material. Therefore, Lin et al. (1997) from Caltech Uni developed its cousin

$Zr_{52.5}Cu_{17.9}Ni_{14.6}Al_{10}Ti_5$ (Vitreloy 105) without the toxic element beryllium – one of the best glass-forming alloys, which is employed in the present study.

For any good candidate material for biomedical applications, mechanical properties, corrosion and bio-compatibility have great significance. Table 2.2 summarises the mechanical properties of the available biomedical Zr-based BMGs and the crystalline biomedical alloys. It can be seen from Table 2.2 that the hardness of the biomedical Zr-based BMGs are about twice of that for the conventional crystalline biomedical 316L SS (320 Hv), Ti-6Al-4V (365 Hv) and CoCrMo alloy (345-390 Hv) (Long and Rack, 1998; Niinomi, 1998). In addition, the yield strength of the Zr-based BMGs is also considerably higher than the above-mentioned crystalline biomaterials (Long and Rack, 1998; Niinomi, 1998). It can be seen from Figure 2.4 that three Ni-free Zr-based BMGs exhibit a high yield strength (>1300 MPa) and fracture strength (>1600 MPa). In addition, the elastic modulus of these Zr-based BMGs is lower than that of the 316L SS (200 GPa) and Ti-6Al-4V (110-125 GPa) (Long and Rack, 1998; Niinomi, 1998). The high strength of the Zr-based BMGs could enable the design of thinner structures for cardiovascular stents and smaller structures for the fixation screws. In addition, the low elastic modulus (much closer to the cortical bone) of these Zr-based BMGs can lead to more uniformly distributed stress and reduced stress shielding effects. Hence, a better long-term performance of biomedical implants and devices made from these metallic glasses could be envisaged in principle.

Table 2.2: Summary of biomedical Zr-based BMGs and their mechanical properties.

Chemical compositions (at. %)	Critical diameter/ thickness (mm)	Strength (MPa)	Elastic modulus (GPa)	Hardness (kg/mm^2)	Reference
$Zr_{52.5}Al_{10}Ti_5Cu_{17.9}Ni_{14.6}$	7	1700 (tensile)	90	590	(Liu et al., 1998)
$Zr_{61}Cu_{17.5}Ni_{10}Al_{7.5}Si_4$	-	1800 (compressive)	-	510	(Lin et al., 2012a)
$Zr_{60}Nb_5Cu_{20}Fe_5Al_{10}$	-	1795 (compressive)	72	-	(Liu et al., 2009)
$Zr_{51}Ti_5Ni_{10}Cu_{25}Al_9$	-	1962 (compressive)	100	542	(Sun et al., 2014)
$Zr_{62.5}Al_{10}Fe_5Cu_{22.5}$	6	1700 (compressive)	80	459	(Huang et al., 2015)
$Zr_{60.14}Cu_{22.31}Fe_{4.85}Al_{9.7}Ag_3$	10	1720±28	82±1.9	-	(Liu et al., 2013)
316 stainless steel	-	170-310 (compressive)	200	320	(Niinomi, 1998)
Ti-6Al-4V	-	758-1117 (compressive)	110-125	365	(Long and Rack, 1998)

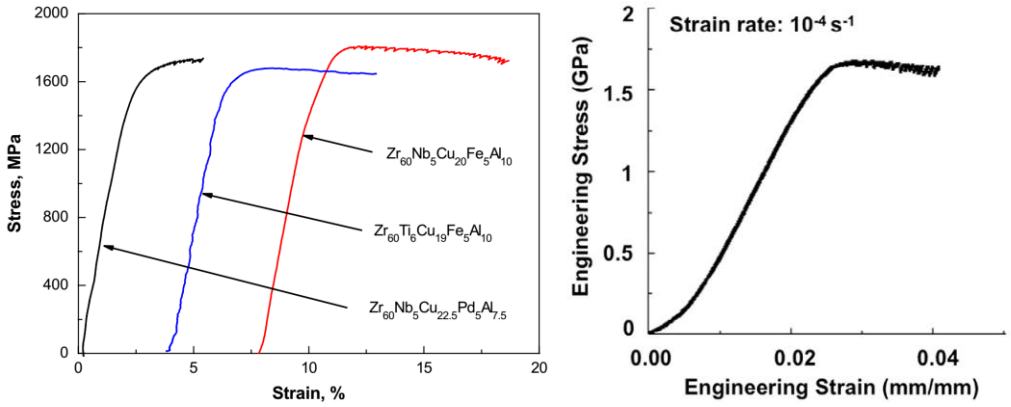

(a) (b)

Figure 2.4: (a) Compressive stress-strain curve of three Ni-free Zr-based BMGs at a strain rate of 1×10^{-4}/s; (b) Engineering stress-strain curve of the $Zr_{62.5}Al_{10}Fe_5Cu_{22.5}$ BMG (Huang et al., 2015; Liu et al., 2009).

Apart from the excellent mechanical properties of Zr-based BMGs, the investigation of their corrosion behaviour is also important to understand their chemical and environmental stability. As for biomedical materials, the corrosion behaviour is related to the electrochemical reactions between the implant's constituents and the human physiological solutions. Researchers have investigated the corrosion behaviour of Zr-based BMGs in different types of simulated body fluids, including phosphate-buffered solution (PBS) (Huang et al., 2009), Hank's solution (Lin et al., 2012a), artificial saliva solution (Wang et al., 2011b) and specific simulated body fluids (SBF) (Liu et al., 2013). Figure 2.5 shows the cyclic-anodic polarisation curves of the $Zr_{55}Al_{10}Cu_{30}Ni_5$ BMG, $(Zr_{55}Al_{10}Cu_{30}Ni_5)_{99}Y_1$, Ti-6Al-4V, Co-Cr-Mo and 316L stainless steel. It can be seen that the Zr-based BMGs show a relatively lower passive current density and a wide passive region, indicating a good corrosion resistance (Huang et al., 2009). The good corrosion resistance of these two biomedical Zr-based BMGs should be attributed to the formation of uniform and protective passive films on the exposed material surface. Moreover, the sudden anodic current increases at the pitting

potentials (E_{pit}) indicate that both Zr-based BMGs and the 316L SS were susceptible to pitting corrosion. Some researchers tried to improve the pitting corrosion resistance of BMGs via chemical composition modification. The results obtained show that the addition of new elements, Nb (Liu et al., 2009) and Ag (Liu et al., 2013), is able to enhance the corrosion resistance against pitting corrosion.

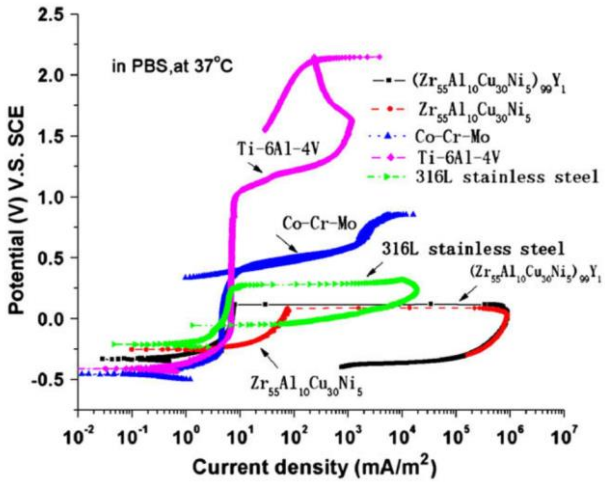

Figure 2.5: Polarisation curves of the $Zr_{55}Al_{10}Cu_{30}Ni_5$ BMG, $(Zr_{55}Al_{10}Cu_{30}Ni_5)_{99}Y_1$, Ti-6Al-4V, Co-Cr-Mo and 316L stainless steel (Huang et al., 2009).

Prior to being used in the body, the bio-compatibility of a candidate biomaterial is an essential property in order to avoid any adverse effects in the human body. The bio-compatibility of biomedical Zr-based BMG has been widely investigated via both in-vitro cellular response and in-vivo animal tests. The in-vitro tests mainly include the cytotoxicity/viability of the cells with the material in the human physiological solutions using the MTT/CCK-8 assay and cell morphology observation using scanning electron microscopy or fluorescence microscopy. Numerous kind of cells have been tested, including mouse pre-osteoblast cells MC 3T3 E1 (Hua et al., 2012; Huang et al., 2011), murine fibroblast cells (L929cells and NIH3T3 cell) (Liu et al., 2008; Liu et al., 2009; Qiu et al., 2006; Wang et al., 2011b), human umbilical vein endothelial cells (Li et al., 2013b), MG63 human pre-osteoblast cells (Li et al., 2012; Li et al., 2013b) and human aortic endothelial cells

(HAECs) (Liu et al., 2009). Since the potential envisaged application of the Zr-based BMG considered in this study is for orthopaedic implants, the human pre-osteoblast cells -MG63 was chosen to investigate its bio-compatibility. In addition to in-vitro tests, in-vivo tests were achieved by the implantation of various Zr-based BMGs in rabbits (Liu et al., 2009). Figure 2.6(a) shows the cytotoxicity results of MTT assays for three different Zr-based BMGs and Ti-6Al-4V alloys after cell culture for 7 days. It can be seen that all metallic glass compositions showed higher absorbance values than that of the Ti-6Al-4V alloys, indicating that Zr-based BMGs have higher cell viability and proliferation activity than Ti-6Al-4V alloys. Figure 2.6(b) shows the morphology of cells grown on the surface of $Zr_{60}Nb_5Cu_{20}Fe_5Al_{10}$ BMG after culturing for 7 days. It can be seen that cells were closely attached and well spread on the BMGs surface, implying excellent bio-compatibility (Liu et al., 2009). Figure 2.7 shows the HE stained results of the tissue around the BMG and Ti alloy after implantation for 12 weeks. It can be seen that slight inflammation existed in these two cases, but that the inflammatory reaction is only inside the fibrous capsule. The tissue in the circles was infiltrated with multinucleated giant cell and lymphocytes, which can reflect the inflammatory reactions. These results demonstrate that the in-vivo bio-compatibility of Zr-based BMGs can be as good as Ti-6Al-4V titanium alloys.

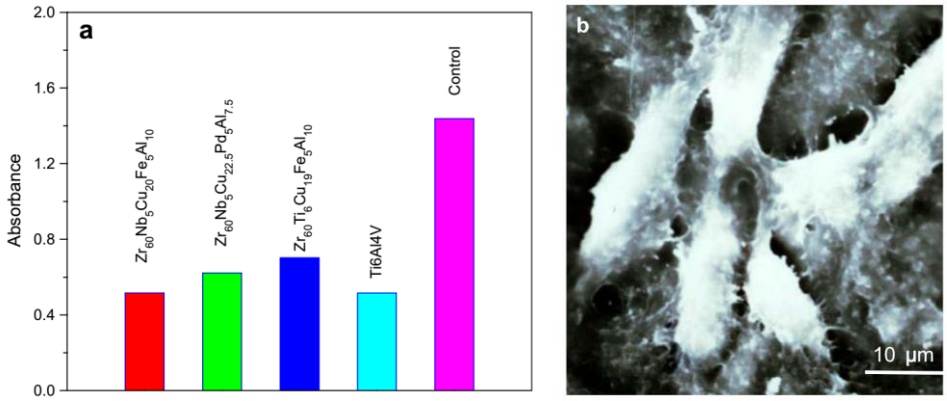

Figure 2.6: (a) Cytotoxicity measurements of three different Zr-based BMGs and Ti-6Al-4V alloys after cell culture for 7 days in comparison with the control group; (b) The morphology of cells grown on the surface of $Zr_{60}Nb_5Cu_{20}Fe_5Al_{10}$ BMG after culturing for 7 days (Liu et al., 2009).

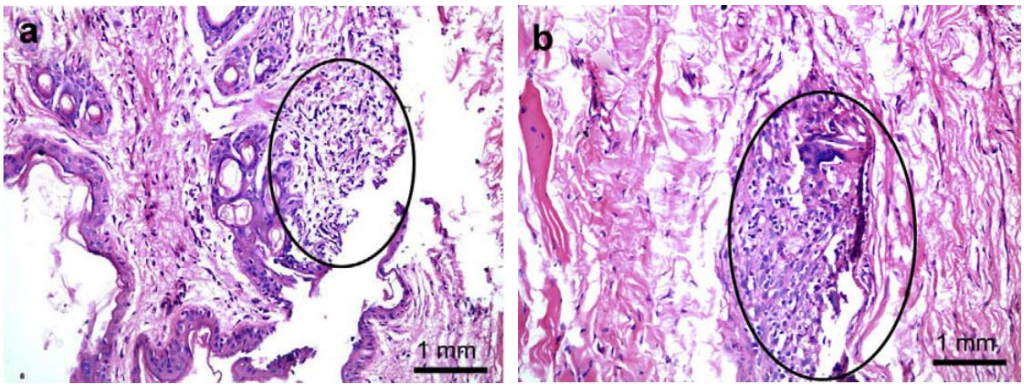

Figure 2.7: HE stained results of the tissue around the BMG and Ti-6Al-4V alloys after being implanted into rabbits for 12 weeks. The tissue in the circles was infiltrated with multinucleated giant cell and lymphocytes, which can reflect the inflammatory reactions (Liu et al., 2009).

2.2 Laser micromachining of bulk metallic glasses

As discussed above, the excellent mechanical properties of BMGs mean that they could be considered candidate material for the manufacturing of micro-scale

biomedical implants and devices, like cardiovascular stents, dental fixation screws and minimally invasive medical devices, which requires high-precision machining. At the same time, BMGs are generally hard-to-machine materials. A number of material removal technologies for micro and nano-scale fabrication have been applied on BMG substrates, such as mechanical machining (Kuriakose et al., 2017) and focussed ion beam (FIB) milling (Zhang et al., 2016). However, mechanical machining can lead to high tool wear and crystallisation of the machined area (Samant and Dahotre, 2009), while FIB milling has a low efficiency in addition to the commonly associated issue of ion implantation. Processing with high-power lasers, on the other hand, provides an alternative solution that can overcome such limitations. Thus, it is perhaps not surprising that several applications of laser irradiation of BMG materials have been reported in the past 20 years, as described in a recent review on the subject by Williams and Lavery (2017). These applications include laser welding, laser additive manufacturing, laser surface treatment and laser micromachining.

In the specific context of laser micromachining of BMGs, which is one of the specific motivations of the research reported in this thesis, investigations have been conducted by a few researchers. The literature on this particular subject can broadly be categorised into single and multiple pulse studies. For single pulse irradiation, the majority of the work has been targeted at the understanding of the surface morphology in and around individual craters. In this context, Liu et al. (2011b) and Zhu et al. (2016) mainly concentrated their efforts on the peculiar formation of surface ripple patterns outside isolated craters (shown in Figure 2.8) when irradiating the well-known Zr-based BMG Vitreloy 1 with a single ns pulse. Liu et al. (2011a) also conducted a study in the ns regime with a similar purpose but on another type of Zr-based BMG. The surface morphological evolution within craters generated on a slightly different Zr-based BMG composition was also studied by Ma et al. (2010). A key difference compared to related single pulse

studies is that these authors used a fs laser to deliver successive pulses on the same spot. This led to the formation of three types of concentric rings structures within the irradiated area depending on the laser fluence and the number of pulses delivered. The surface morphology of single craters was also the focus of the work from Williams and Brousseau (2016) in the context of single ns laser irradiation of Vitreloy 1. In contrast to the investigations reported earlier, these authors also analysed the output of a thermal model, which could predict temperature profiles under different laser parameter conditions, as a means to support the interpretation of experimental observations. It is worth noting that Jiang et al. (2015) and Quintana et al. (2009) also reported single pulse experiments on amorphous metals but not for the specific purpose of studying crater morphology. More specifically, the work from Jiang et al. (2015) was targeted at the understanding of the explosive boiling process when irradiating a Vitreloy 1 specimen with a ns pulse while Quintana et al. (2009) explored whether the single pulse ablation of a Ni-based amorphous material could lead to the formation of crystalline precipitates. To achieve this, a foil 40 µm thick was used as the workpiece and experiments were conducted both in the ps and µs regimes. The results showed that single pulse irradiation in both regimes did not lead to crystallisation of the amorphous sample.

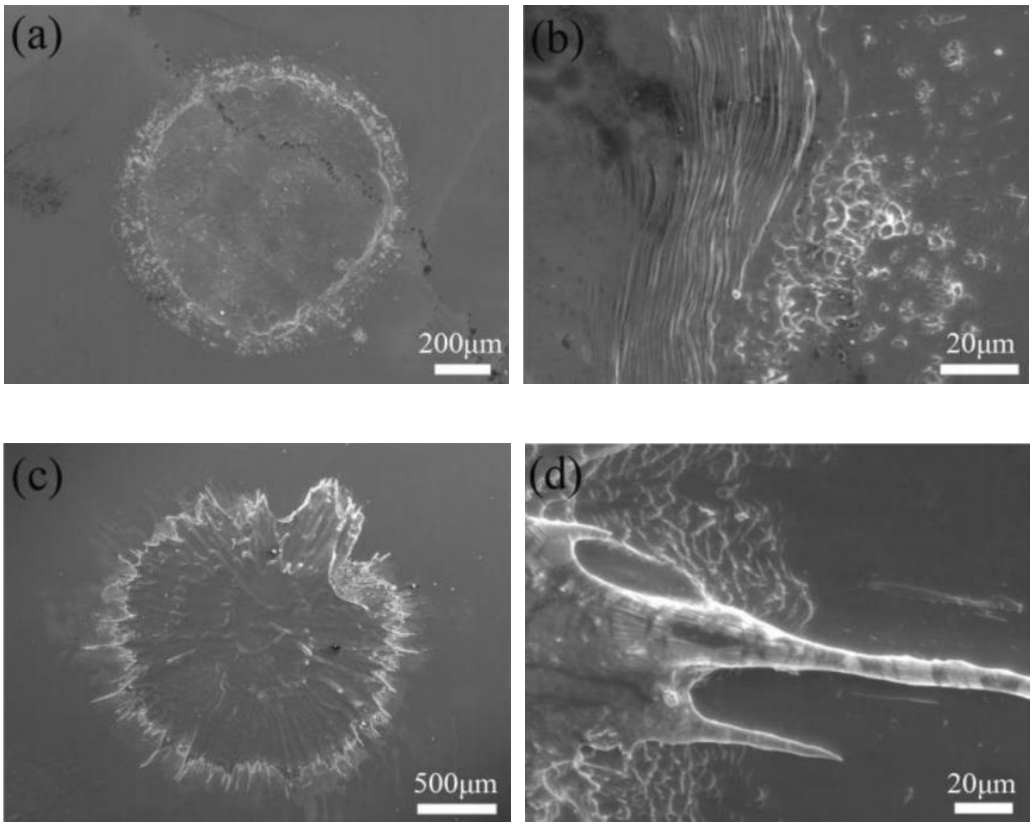

Figure 2.8: Surface morphologies of Vitreloy1 irradiated by a single ns laser pulse at the laser energy of 200 mJ. (a) without confinement; (b) enlarged view of (a); (c) with confinement; (d) enlarged view of (c) (Zhu et al., 2016).

Exploring the microstructure of BMG specimens after laser processing was also the aim of a few reports in the second category of studies of interest here, i.e. those concerned with multiple and moving pulses for achieving laser milling, drilling or cutting operations. Lin et al. (2012b) successfully used a ns laser to cut a Mg-based BMG while being able to maintain its amorphous nature by appropriately controlling laser power and scan speed. Wang et al. (2007) performed several laser micromachining operations, namely drilling and trenching (shown in Figure 2.9), of a Zr-based amorphous alloys using fs laser pulses. In this regime, these authors found that crystallization, molten trace and spatter could be avoided. In the area of multiple pulse micromachining of BMGs, it is also of interest to mention two studies

that reported the application of laser processing as one possible step in a process chain to fabricate micro-components. These include the work of Chen et al. (2013), who demonstrated the machining of periodic micro and nano-structures on a Pd- and Ni-based BMG using a fs laser and also, the work of Vella et al. (2014). These latter authors described the successful application of ps and ns laser processing to produce patterns in a Vitreloy 1b BMG workpiece, which was subsequently used as a mould for the replication of micro-structured polymer components.

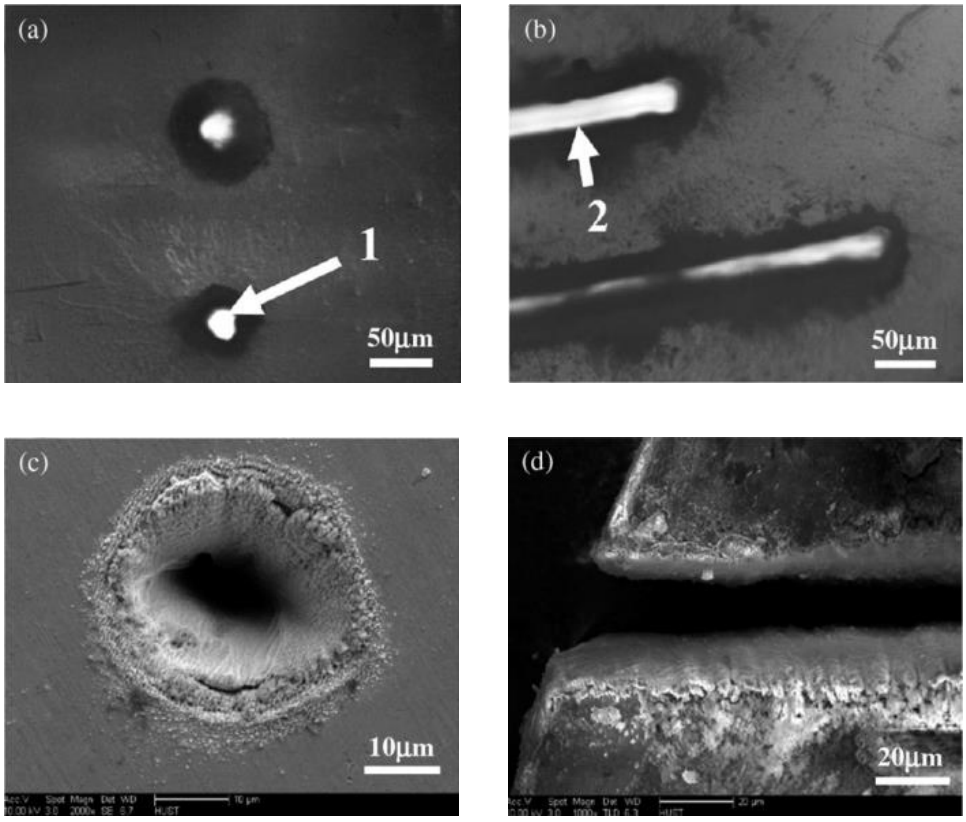

Figure 2.9: (a) SEM micrographs of the fs laser machined holes; (b) SEM micrographs of the fs laser machined trenches; (c) enlarged view of (a); (d) enlarged view of (b) (Wang et al., 2007).

2.3 Laser surface texturing of bulk metallic glasses

When considering implant materials, improving the bio-compatibility with tissues is also a key factor since the reaction of implants with the host tissue determines their long-term performance. It has been demonstrated (Kumari et al., 2015; Pfleging et al., 2015; Shen et al., 2019) that bio-compatibility depends on the surface wettability, surface topography and surface chemistry to a certain degree. In particular, a higher wettability, i.e. enhanced hydrophilicity, has a beneficial influence on the cell/protein attachment, growth, proliferation, and differentiation (Hallab et al., 2001). In addition, rough surface can also benefit the cell attachment and cell alignment (Anselme et al., 2002). Therefore, achieving a suitable surface property is critical to improve the bio-compatibility of implants. Surface treatments, like coating (Yang et al., 2005), ion implantation (Rautray et al., 2011) and laser surface texturing (Kumari et al., 2015), have been successfully used on traditional biomedical alloys, especially titanium alloys, to enhance the hydrophilicity, modify the surface roughness and chemical composition, thus enhancing the bio-compatibility. Among these methods, the laser surface texturing has been considered as a very promising technique for modifying the surface properties of biomaterials due to associated characteristics of flexibility, simplicity, controllability and reproducibility. In addition, laser surface texturing also can avoid introducing toxic substances on processed surfaces (Cunha et al., 2016).

2.3.1 Introduction to laser surface texturing

Laser surface texturing (LST) is a novel method that relies on a laser's rapid and precise removal technology to fabricate micro- or nano-scale structures on different types of materials, including ceramics, metals, polymers and composites (Wahab et al., 2016). LST already has been successfully used to modify tribological

performance (Etsion, 2005), wettability (Yang et al., 2017), bio-compatibility (Kumari et al., 2015) and optical properties (Iyengar et al., 2010) as well as to enhance adhesion joint strength (Man et al., 2010). With regards to the wettability and bio-compatibility modification, several types of structures fabricated by LST have been reported on titanium alloys and stainless steels (Cai et al., 2018; Chen et al., 2007; Raimbault et al., 2016; Ta et al., 2015). However, in the specific field of laser texturing of BMG materials, the literature is still scarce regarding efforts to tune the wettability and bio-compatibility of such surfaces. Therefore, the literature review presented in this section mainly reports former studies of LST-induced wettability and bio-compatibility modification for conventional biomedical metallic alloys. Such studies can still provide guidance regarding characterisation methods, measurements and analysis procedures for the application of LST on BMGs.

2.3.2 Laser surface texturing for wettability modification

Pfleging et al. (2015) fabricated two kinds of surface patterns, i.e. dimples and grooves (shown in Figure 2.10), on a Ti-6Al-4V alloy using a ns ArF excimer laser. Figure 2.11 shows the surface contact angle measurements of the obtained dimple and linear laser textured surface, it can be seen that dimple and linear texturing both can enhance the hydrophilicity, and that the linear texture leads to better outcomes compared to the dimple texture. These authors attributed the hydrophilicity enhancement to the increased surface area. The same research group further investigated the bio-compatibility of this titanium alloy with these two surface structures in a study from Kumari et al. (2015). In this case, it was shown that laser texturing could increase the bio-activity of the alloy in Hank's solution and that no cytotoxic substances were produced. It was also found that the groove textured surface resulted in a better cell attachment compared to the as-received and dimple textured surfaces. Li et al. (2016) fabricated stable hydrophilic and

super-hydrophobic surfaces on a titanium alloy via laser texturing coupled with the silanization process. In particular, the direct laser textured surface was hydrophilic, and it became super-hydrophobic after silanization. Mukherjee et al. (2013) investigated the effect of microgroove dimensions on the wettability and protein absorption of a Ti-6Al-4V titanium alloy surface and found that the surface structures dimensionally closer to the cell dimensions could positively affect the viability and spreading of cells. Most recently, Huerta-Murillo et al. (2019) modified the wettability of Ti-6Al-4V titanium alloy via the fabrication of hierarchical surface structures, and wettability modification mechanism was explained from the evolution of surface chemistry .

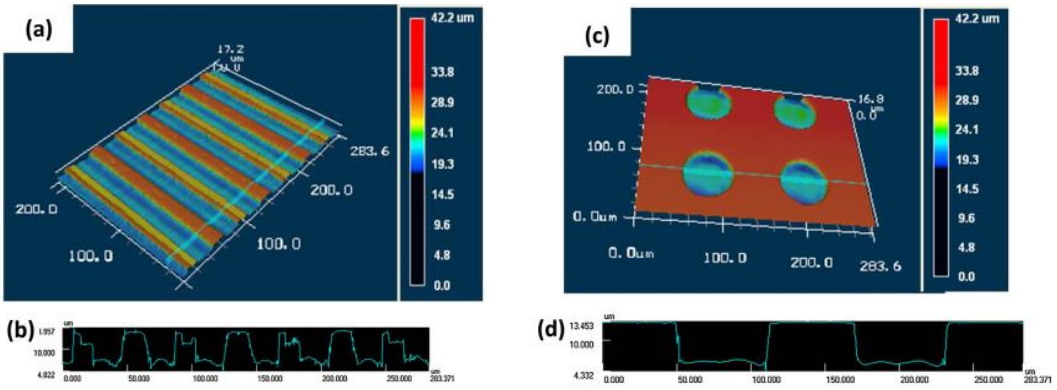

Figure 2.10: Surface topography of the laser textured surface of Ti-6Al-4V (a) 3D topography of the linear textured surface; (b) cross-sectional profile of (a); (c) 3D topography of the dimple textured surface; (d) cross-sectional profile of (c) (Pfleging et al., 2015).

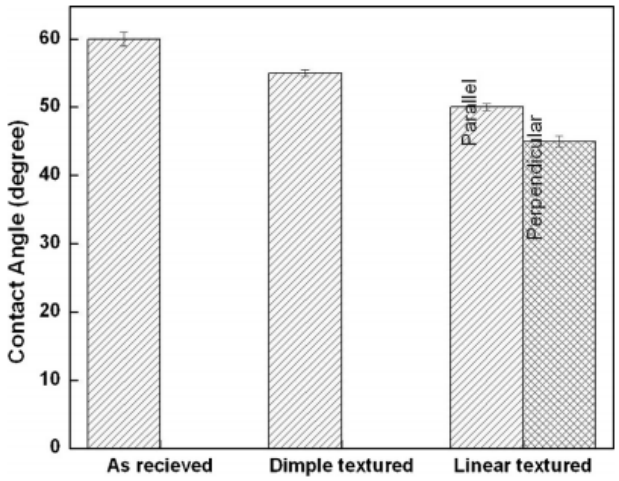

Figure 2.11: Surface contact angle measurements of the as-received and laser textured surface with dimple and linear textures (Pfleging et al., 2015).

2.3.3 Laser surface texturing for bio-compatibility enhancement

In the past several decades, numerous investigations have been reported that focused on the bio-compatibility enhancement of traditional biomedical alloys treated by LST (Hsiao et al., 2016; Kumari et al., 2015; Lee et al., 2018; Mukherjee et al., 2013; Ohtsu et al., 2017; Yu et al., 2018). LST was utilised by Kumari et al. (2015) to improve the bio-compatibility of Ti-6Al-4V titanium alloy. Figure 2.12 shows the fluorescent micrographs and XTT results of MC3T3-E1 mouse fibroblast cells on the surface of as-received, linear textured and groove textured Ti-6Al-4V samples. It can be seen that the laser textured Ti-6Al-4V shows a comparable cell viability with the as-received titanium alloy, but that laser-induced linear textures can make the cell to align along them. Hsiao et al. (2016) used an ultraviolet laser to produce micro-grooves on a Ti-6Al-4V surface and compared the osteogenic cell growth on the as-received and laser-textured surfaces. It was found that the laser-induced groove texture could provide a favourable environment for osteogenic cell to grow on the surface. A femtosecond laser was also successfully exploited by Lee et al. (2018) to generate sub-micrometre patterns to improve cell

viability on a titanium substrate. Mukherjee et al. (2013) further concluded that laser-induced surface features dimensionally close to the size of cells could positively affect cell viability and spreading. Moreover, Ohtsu et al. (2017) improved the cellular adhesiveness and cell proliferation by LST conducted on a titanium surface. Yu et al. (2018) also investigated the effect of picosecond laser texturing on the bio-compatibility of a titanium alloy, and concluded that micro-grooves were helpful for cell adhesion, cell growth and contact guidance.

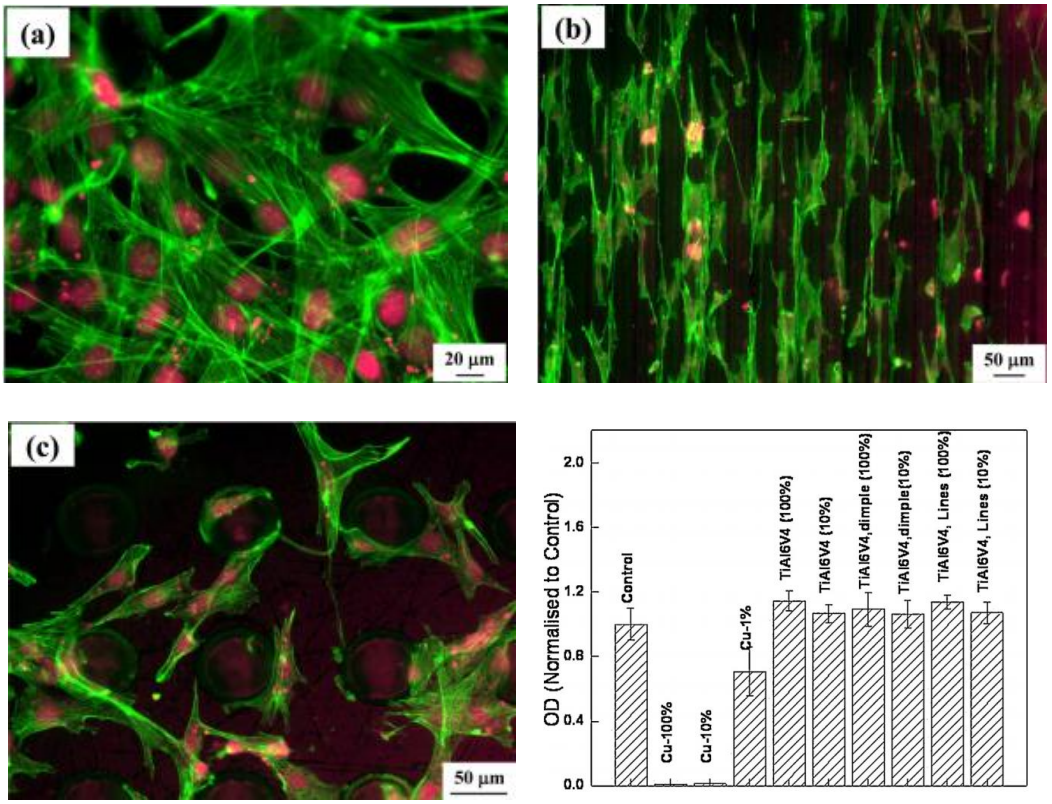

Figure 2.12: Fluorescent micrographs of the MC3T3-E1 mouse fibroblast cells on the surface of as-received (a), linear textured (b) and dimple textured samples (c); (d) XTT results of these three kinds of samples (Kumari et al., 2015).

2.4 Laser surface melting of bulk metallic glasses

As reported earlier, it is well-documented that, in comparison with their crystalline counterparts, BMGs exhibit high strength and hardness (Chen, 2011), large elastic

limit (Ashby and Greer, 2006) and good corrosion resistance (Löffler, 2003). However, it is also well-known that BMGs generally deform via highly localised individual shear banding events (Schuh et al., 2007; Trexler and Thadhani, 2010). The initiation and propagation of such shear bands result in very limited macroscopic plasticity before catastrophic failure, thus seriously impeding their applications in load-bearing engineering scenarios (Li and Zheng, 2016; Telford, 2004; Zhang et al., 2006). In recent years, extensive research studies have been completed in an attempt to improve the plasticity of BMGs. The approaches reported can be categorised into two groups, namely intrinsic and extrinsic (Fu et al., 2016; Gao et al., 2016; González et al., 2013; Wang et al., 2014; Wu et al., 2012; Yokoyama et al., 2009; Yu et al., 2012). The intrinsic methods rely on the addition of chemical elements (Yu et al., 2012). Extrinsic strategies mainly comprise surface treatments, including shot peening (González et al., 2013), surface mechanical attrition treatment (Wang et al., 2014), laser shock peening (Fu et al., 2016) and laser surface melting (Wu et al., 2012). These have been applied on a variety of BMG compositions and proved efficient methods to improve their mechanical properties. Among these, laser surface melting (LSM) has been demonstrated to be an effective method to improve the plasticity of BMGs as reported in a number of studies in the past decades (Chen et al., 2012; Chen et al., 2010; Cheng et al., 2016a, b; Huang et al., 2018; Wu et al., 2012; Zuo et al., 2018). One of the earliest reports on this topic is from Chen et al. (2010), who showed that the compressive plastic strain of a Zr-based BMG could be increased from 0.3% to 5.3% after LSM (shown in Figure 2.13), while the amorphous nature of the alloy could be retained. Subsequent investigations further confirmed the positive effect of LSM on retarding brittle fracture in BMG substrates. For example, when trialling the LSM process on a Cu-Zr-based BMG, Wu et al. (2012) reported that improvements in compressive plastic strain (shown in Figure 2.14) could also be achieved when crystalline precipitates (shown in Figure 2.15) were introduced in

the glassy matrix as a result of laser processing. In another example, and while working with a very similar Cu-Zr-based BMG to that of Wu et al. (2012), Cheng et al. (2016b) observed that LSM could also enhance tensile plasticity (shown in Figure 2.16). Collectively, these studies have suggested that the improved plasticity could be a combination of factors, which include 1) the increase in free volume resulting from the high cooling rate typically associated with localised high-power laser irradiation (Chen et al., 2010), 2) the influence of residual stress redistribution (Chen et al., 2010) and 3) the introduction of structural heterogeneities in the glassy matrix (Huang et al., 2018), such as residual shear bands and/or crystalline phases.

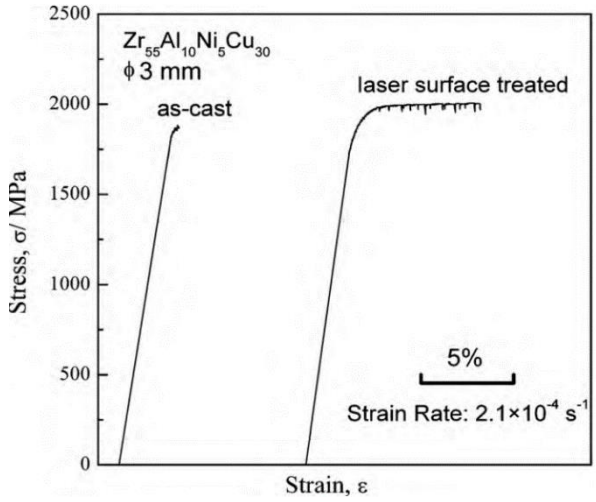

Figure 2.13: Compressive stress-strain curves of as-cast and the LSM treated glassy rods (Wu et al., 2012).

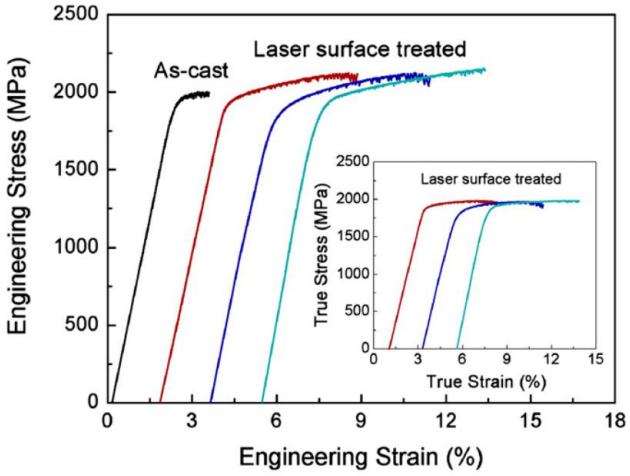

Figure 2.14: Compressive stress-strain curves of as-cast and the LSM treated glassy rods (Chen et al., 2010).

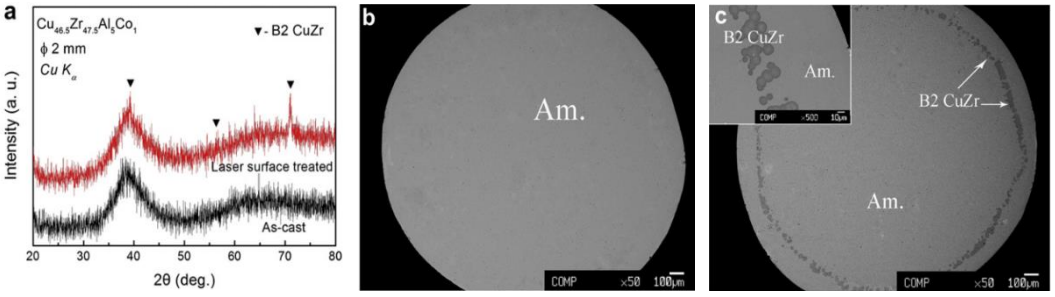

Figure 2.15: (a) XRD patterns of as-cast and treated glassy rods. SEM images of the cross sections of CuZr-based metallic glass rods before (b) and after (c) laser surface treatment (Wu et al., 2012).

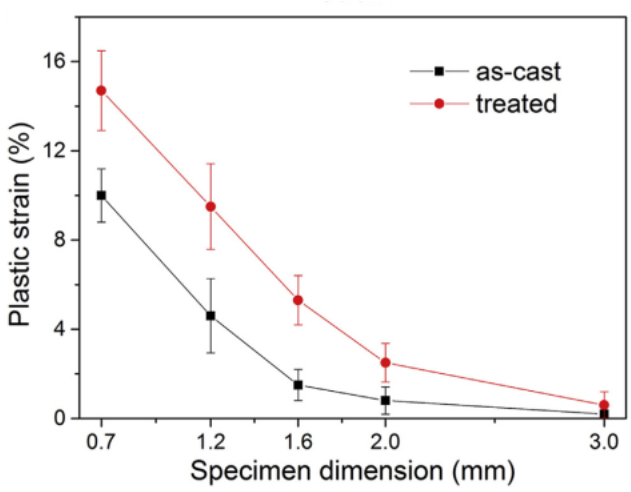

Figure 2.16: Plastic strains of as-cast and LSM treated specimens for different sample dimensions (Cheng et al., 2016a).

Regardless of the specific physical mechanism, or combination of mechanisms, driving the observed enhanced plasticity of BMGs following laser processing, it is interesting to point out that, in many of the experimental conditions reported to date, LSM was also accompanied by a softening of the irradiated surfaces (Chen et al., 2012; Chen et al., 2010; Huang et al., 2018). Only in a few reports, namely those from Tariq et al. (2009), Mudry et al. (2013), and more recently, Huang et al. (2019), an increase in hardness was also observed following laser surface treatment. However, it is also worth noticing that these particular studies were most likely to be carried out when ablation, rather than melting, was the dominant processing regime. This was certainly the case for Huang et al. (2019) based on the observation of the Scanning Electron Microscope (SEM) images (shown in Figure 2.17) that the authors reported. Tariq et al. (2009) and Mudry et al. (2013) did not provide such SEM images or made any comments on the topography of the resulting surfaces. However, it is reasonable to suggest that laser ablation was also likely the dominant regime given that the estimated fluence employed (in J/cm^2) was one order of magnitude higher for Mudry et al. (2013) and two orders of magnitude higher for Tariq et al. (2009), compared to that of Huang et al. (2019).

Thus, for practical applications, it is of interest to find out whether the surface hardening of BMGs could also be achieved in the LSM regime, in addition to the well-known LSM-induced surface softening effect. It has to mention that surface hardening can improve its anti-abrasion resistance and further enhance its longeivity within the human body. Indeed, if a BMG part is cast near net-shape, it may not be desirable to apply a post-processing step leading to substantial laser-based material removal on the surface.

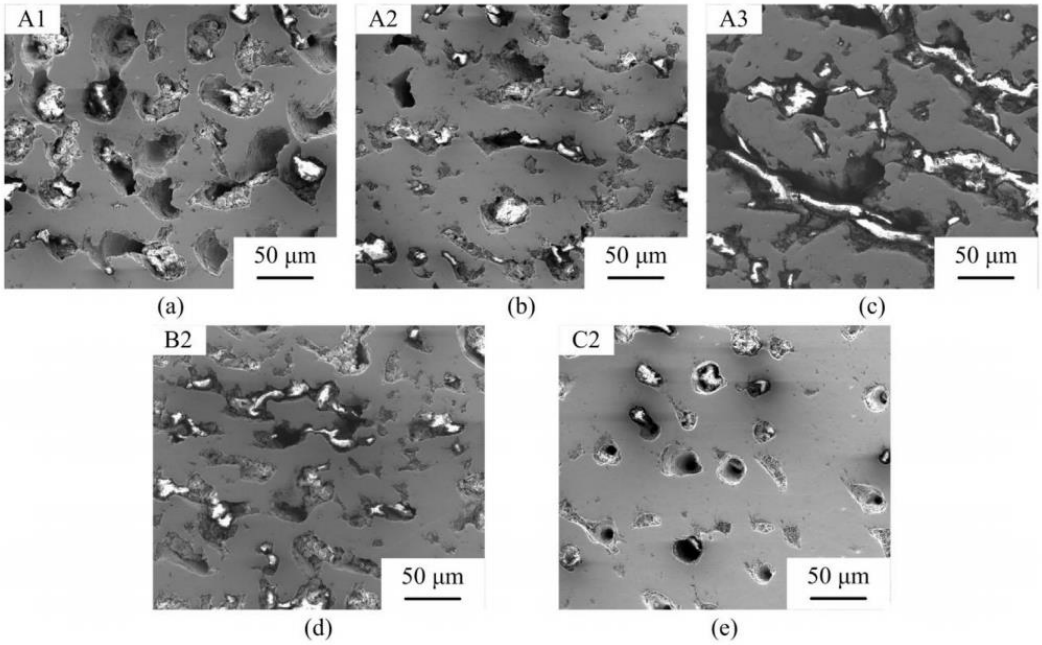

Figure 2.17: SEM morphologies of laser irradiated regions on a Vitreloy 1 BMG after polishing (Huang et al., 2019).

It is also important to note that in all three studies highlighted above (i.e. Tariq et al. (2009), Mudry et al. (2013), and Huang et al. (2019)), a common observation is that the increase in hardness was always accompanied by the formation of crystalline precipitates. Tariq et al. (2009) selected three different laser processing conditions when irradiating an amorphous $Zr_{55}Cu_{30}Al_{10}Ni_5$ workpiece. While the resulting hardness was systematically higher than that of the as-cast specimen, these authors also observed that, as the laser power was raised, and consequently

the size of the primary secondary phase increased, the hardness reduced. On the contrary, Mudry et al. (2013) found that the hardness of laser irradiated Fe-based amorphous ribbons increased linearly with the percentage increase of the introduced crystalline phase. So far, the report from Huang et al. (2019) is the only example in which both hardening and softening effects were observed depending on the laser processing conditions utilised (shown in Figure 2.18). In this specific study, the well-known Vitreloy 1 amorphous alloy was irradiated in a nitrogen-rich environment. From the range of process parameters selected, these authors found that only one combination led to a hardness value higher than that of the as-cast specimen. Perhaps not surprisingly given the earlier results from Tariq et al. (2009) and Mudry et al. (2013), the sample with an increased hardness was also the specimen which exhibited the most pronounced laser-induced introduction of a secondary phase.

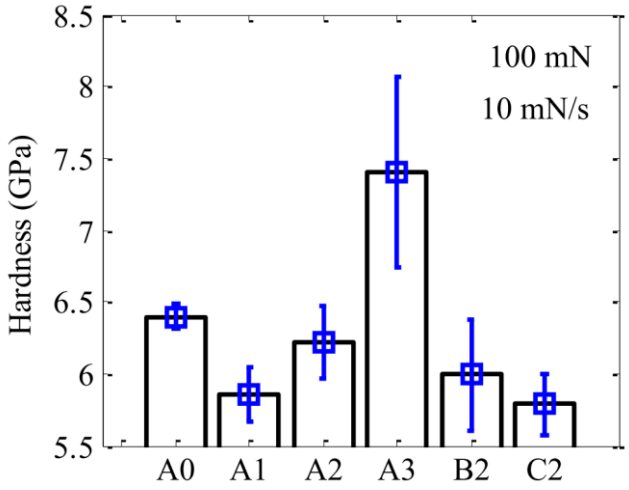

Figure 2.18: Surface hardness values for different samples; A0 represents the as-cast sample, A1, A2, A3, B2 and C2 represent the BMG samples treated with different laser parameters (Huang et al., 2019).

2.5 Summary and knowledge gaps identified

This chapter presented a review about the development of bulk metallic glasses, their biomedical applications as envisaged by the research community, as well as methods for the bio-compatibility evaluation of BMGs. Furthermore, the present state-of-the-art in the laser processing of BMGs for 1) micromachining, 2) surface texturing for bio-compatibility enhancement purpose and 3) surface melting for the improvement of their mechanical properties was discussed in detail as well. Based on the studies reviewed, a number of conclusions and knowledge gaps relevant to the context of this Thesis are identified as follows:

I. Investigations in nanosecond laser micromachining on Vitreloy 105 via a combined experimental and theoretical study. It can be said that investigations in the laser micromachining of BMGs with multiple pulses have essentially been experimental in nature. For this reason, a combined theoretical and experimental study was conducted by further developing the thermal model reported in the single pulse work of Williams and Brousseau (2016) to simulate the incident energy from multiple and moving pulses. It is anticipated that knowledge of the theoretical thermal history of a BMG substrate can assist in the selection of appropriate laser processing parameters. Also, it is expected that by combining experimental observations and theoretical outcomes, an enhanced understanding of the laser micromachining of Vitreloy 105 could be achieved. A numerical simulation model that incorporates temperature dependent thermo-physical properties and transient physical process is developed to predict the thermal behaviour. The underlying material removal mechanism and the influence of laser parameters are discussed according to the temperature evolution during the process in Chapter 4.

II. Investigations in the fabrication of surface patterns for wettability modification on Vitreloy 105 by nanosecond laser surface texturing. In the specific field of laser texturing of BMG materials, the literature is still scarce regarding efforts to tune the wettability of such surfaces. However, based on the wider body of literature about laser-based studies focussed on wettability modification of orthopaedic titanium alloys, it is expected that the tuning of surface wettability should depend on both the alteration of the surface topography and its chemistry. Therefore, further research efforts towards modifying the wettability of BMGs and also, focussed on understanding the associated driving mechanisms, are important to promote such amorphous alloys in bio-applications. Therefore, the nanosecond fibre laser was utilised in this study to fabricate two types of surface structures, i.e. dimple and groove patterns, on Vitreloy 105. Importantly, the surface chemistry of the laser textured surfaces was also investigated, using EDX mapping and XPS elemental analysis to evaluate the role of both surface topography and chemistry in the laser-induced modification of surface wettability. The associated results and discussions are reported in Chapter 5.

III. Demonstration that laser surface texturing can be exploited to enhance the bio-compatibility of Zr-based BMGs. To the best of the author's knowledge, no previous study has reported the application of laser surface texturing to enhance the bio-compatibility of the BMGs. In the present study, laser surface texturing of Vitreloy 105 was undertaken with the groove and dimple patterns using the ns fibre laser. The surface topography, chemical composition and wettability of these surfaces were characterised and measured via non-contact three-dimensional confocal microscopy, scanning electron microscopy, X-ray photoelectron spectrometry and contact angle measurements. The viability, attachment and morphology of

MG63 cells on different textured surfaces was evaluated by applying specific instruments and test formats. Finally, relationships between bio-compatibility and surface chemical composition, surface roughness and surface wettability of the Vitreloy 105 surface with and without laser texturing was discussed. This work is the focus of Chapter 6.

IV. Investigations in hardness, residual stress distribution, shear banding behaviour and microstructure evolution of Vitreloy 105 after laser surface melting. Given the body of literature reported earlier, one of the motivations behind the study conducted in Chapter 7 was to investigate whether it is possible to induce surface hardening while still operating in a melting-dominated regime during laser processing. Indeed, if a BMG part is cast near net-shape, it may not be desirable to apply a post-processing step leading to substantial laser-based material removal on the surface. To achieve this aim, it is proposed to conduct LSM in ambient atmosphere rather than under inert gas shielding, as it has typically been the case in previous research. It is expected that processing in an oxygen environment promotes the formation of nucleation sites, and the subsequent growth of crystalline precipitates. In addition to the evaluation of the hardness, a further motivation was to assess the residual stress on the surface of irradiated regions. This aspect was not considered in any of three laser-based studies described earlier that led to surface hardening. To achieve this, it is proposed to implement a relatively recent technique, which is still rather unknown in the field of BMG research. This technique relies on micro-scale focused ion beam milling and digital image correlation analysis (see e.g. the review from Lunt and Korsunsky (2015)). With the exception of reports by Cao et al. (2015) and Wang et al. (2016) in the context of laser shock peening, and by Korsunsky et al. (2016) when synthesising a Zr-based BMG, this approach has rarely been employed for residual stress

measurements in amorphous alloy research. It is expected that this technique is particularly suited for the current investigation of LSM-induced hardness modification because the literature suggests limited correlation between hardness and compressive residual stress in BMGs (see, e.g. (Wang et al., 2011a)). Thus, traditional hardness tests alone may not be suitable to present a comprehensive assessment of how processing conditions affect the residual stress following LSM treatment. In addition, due to the size limitation of the Vitreloy 105 samples that were available in this study, compressive or tensile tests could not be conducted to complement the hardness and residual stress measurements by the additional assessment of the plasticity modification induced by LSM. To overcome this issue, nanoindentation tests were carried out as a means to analyse serrated flow characteristics of as-cast and laser irradiated samples, and thus to gain some insights into the localised shear banding behaviour associated with plasticity change under different LSM conditions. This study is reported in Chapter 7.

Chapter 3 Materials, experimental devices and methodology

In this study, experimental and numerical simulation methods were exploited. The nanosecond fibre laser system, which was a key experimental device in this study, was capable of being used over a wide range of parameters in order to fit different purposes, including laser micromachining, laser surface texturing (LST) and laser surface melting (LSM). Further, a number of surface topography characterisation techniques were employed, i.e. 3D optical microscopy, contact micro-profilometry and atomic force microscopy (AFM). The microstructural characterisation of specimens was completed via X-ray diffraction (XRD), differential scanning calorimetry (DSC), scanning electron microscopy (SEM), energy dispersive X-ray (EDX) and X-ray photoelectron spectroscopy (XPS). The evaluations of mechanical properties, in particular hardness and shear banding behaviour, were conducted via Vickers micro-hardness, nanoindentation tests and complemented by combined micro-scale focused ion beam (FIB) milling operations and digital image correlation (DIC) analyses for residual stress measurements.. In-vitro cell culture and associated tests, i.e. cell viability, cell attachment and morphology observation, were also conducted to verify the bio-compatibility of the laser textured Vitreloy 105 surfaces. Finally, a commercial software platform, COMSOL™ was used to perform thermal analyses. This Chapter presents details about the Vitreloy 105 material and the range of experimental equipment used while the methodology behind the thermal simulations will be reported in Chapter 4.

3.1 BMG material

The BMG investigated in this work is commonly named Vitreloy 105. It has a nominal composition of $Zr_{52.5}Cu_{17.9}Ni_{14.6}Al_{10}Ti_5$ (composition given in atomic percent, at%). The Vitreloy 105 specimens were commercially available and produced by the company Visser Precision (Denver, USA). These were cast using vacuum injection moulding to produce rods, which were 3 mm in diameter and 10 mm in length. Thus, in addition to the favourable fatigue properties of Vitreloy 105 mentioned earlier, the BMG parts processed in this study exhibited the interesting characteristic of being synthesised with an industrial process rather than a laboratory-based technique. Furthermore, the physical, thermo-dynamical and mechanical properties of Vitreloy 105 are well documented in the literature (Table 3.1). The composition of the alloy delivered by Visser Precision was $Zr_{52.8}Cu_{17.6}Ni_{14.8}Al_{9.9}Ti_{4.9}$ and thus, very slightly different from the standard composition of Vitreloy 105, which is $Zr_{52.5}Cu_{17.9}Ni_{14.6}Al_{10}Ti_5$. The specimens used for the laser experiments were cut from the as-received 10 mm long cylindrical rods with micro wire electrical discharge machining (μEDM) with as minimum energy as possible to obtain samples 3 mm in diameter and 4 mm thick, as shown in the inset of Figure 3.1. The structure of the as-fabricated alloys was characterised by X-ray diffraction (XRD) with Cu Kα (λ=1.789 Å) radiation at 35 kV and 40 mA in continuous scan mode. As can be seen in Figure 3.1, the XRD pattern of the as-cast specimens shows an overall amorphous halo and two crystalline peaks within the glassy matrix. Thus, it can be said that the specimens were not fully amorphous as they contained a crystalline phase, which was identified as $CuZr_2$. Due to the small size of the Vitreloy 105 amorphous alloys available in this study, to ease handling and subsequent characterisation, all the BMG samples were mounted in the conductive resin and the top surface was left for exposure. Although extreme care was taken to cut the as-delivered 10 mm long rod with wire-EDM using as low

energy as possible, this initial process may result in the formation of a crystallisation layer and a rough surface. Hence, before and after the microstructural characterisation with XRD and the laser processing experiments, the exposed surfaces of the specimens were mechanically grinded using 1200 and 2000 grit SiC papers followed by a final polishing step using a 1 μm diamond gel suspension until a mirror-like appearance was achieved. The specimens were also cleaned with acetone in an ultrasonic bath for 15 minutes to remove impurities and small particles from their surface. It has to mention that the only polished samples with no subsequent processing were named as-cast (AC) samples. In addition, before and after laser processing, all the samples were cleaned using the above-mentioned method and dried in the air within 1 h.

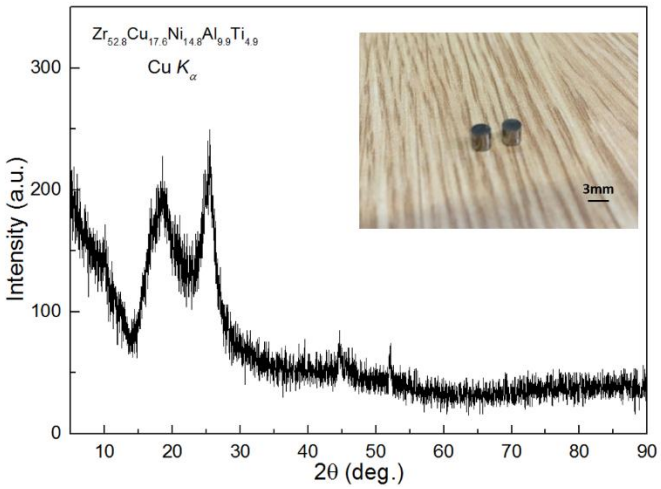

Figure 3.1: XRD pattern and photo (inset) of Vitreloy 105 metallic glass specimens.

Table 3.1: Material property values of the $Zr_{52.8}Cu_{17.6}Ni_{14.8}Al_{9.9}Ti_{4.9}$ BMG (Bian et al., 2002; Glade et al., 2000).

Material Property Parameter (units)	Symbol	Parameter Value
Density (g/cm^3)	ρ	6.73
Glass Transition Temperature (K)	T_g	675
Crystallization Temperature (K)	T_x	727
Melting Point (K)	T_m	1069
Critical cooling rate (Ks-1)	R_c	10
Young's modulus (GPa)	E	88.6
Shear modulus (GPa)	G	32.3
Bulk modulus (GPa)	B	114.1
Poisson's ratio	v	0.37
Molar mass (kg/mol)	M	0.0729
Vickers's Hardness ($HV_{0.2}$)	H_v	579

3.2 Nanosecond fibre laser system

The system utilised in this study was a fibre laser with 20 W output power manufactured by SPI Lasers (Southampton, United Kingdom). The actual spatial profile of the intensity of the delivered laser beam was near Gaussian with an M^2 value less than 2 while the focal length was 100 mm. This particular laser system is a Master Oscillator Power Amplifier (MOPA) laser which uses a seed laser accompanied with two amplifiers to achieve a high-power output laser pulse. With this unique MOPA configuration, the full average power can be maintained even as the repetition rate increases. The wavelength of the emitted laser was 1064 nm, and the maximum frequency is 500 kHz. Most importantly, this fibre laser had the "Pulse Tune" technique which can modify the pulse duration of the emitted laser ranging from 15 ns to 220 ns. Each pulse duration possesses a maximum pulse

energy and a frequency referred to as “PRF0” at which the peak power is achieved. Each pulse duration corresponds to one waveform, which can be pre-set via a software. The waveforms used in the present study are presented in the following table (Table 3.2) together with their pulse duration and maximum pulse energy, E_{max}, at PRF0.

Table 3.2: Preset waveforms with their corresponding pulse duration, PRF0, and the maximum energy at PRF0.

Waveform number	Pulse duration (ns)	PRF0 (kHz)	Emax (mJ) at PRF0
11	220	35	0.57
16	140	51	0.39
22	65	80	0.25

Figure 3.2 presents the generic evolution of the average power and pulse energy as a function of repetition rate for all the laser waveforms. Even though this behaviour is applied to every waveform, each of them has a specific PRF0 value at which it reaches the peak power. It can be seen from Figure 3.2 that, when the pulse repetition frequency is above the PRF0, the pulse energy decreases while the average power remains constant with the increase of the repetition rate. The relationship can be described using Equation 3.1:

$$Pulse\ Energy\ = \frac{Average\ Power}{Frequency} \tag{3.1}$$

When the pulse repetition frequency is below the PRF0, the average power decreases with the decrease of pulse frequency to a certain value. With the abovementioned features of the fibre laser, the pulse energy always maintains in its maximum value, E_{max}.

In order to calculate the delivered fluence, the effective diameter (*D*) of the laser spot was estimated first. Using the method presented by Liu (1982), it was found

to be 32 μm. This was described in more details in a previous work conducted by Williams and Brousseau (2016). The delivered laser fluence was then calculated by dividing the laser energy per pulse by the laser spot area, as shown in Equation 3.2:

$$Fluence = \frac{Energy}{laser\ spot\ area} \quad 3.2$$

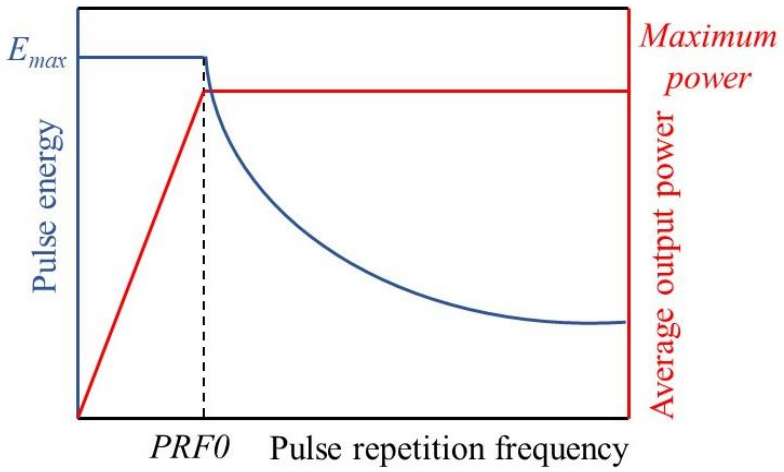

Figure 3.2: Evolution of pulse energy and average power as a function of the pulse repetition frequency (From SPI Manual)

This fibre laser source was integrated into a LaserTech system (DMG, Germany). This machine tool displayed a high-resolution 5-axis motion platform to achieve the cooperative control of the laser and the translation stage. All laser processing operations were conducted in ambient atmosphere. The laser was kept stationary to ensure the consistency of the delivered laser energy. Thus, the laser path on specimen surfaces was dictated via the movement of the machine tool stage. Schematic diagram of the nanosecond fibre laser system used in the present study is shown in Figure 3.3. As can be seen from this figure, the fibre laser, the translation motion platform, the clamping stage, the built-in probe and other accessories are enclosed in the box for the purpose of operation safety. A computer was used to control the laser and the motion platform via the LSPwin

software (DMG. Germany). The delivered laser energy, frequency, pulse duration, scanning speed and track distance could also be pre-set via this software. The clamp stage was specifically designed for the fixation of the specimen. The built-in probe was used to measure the thickness of the specimen, to adjust the distance from the specimen surface to the delivery optic laser.

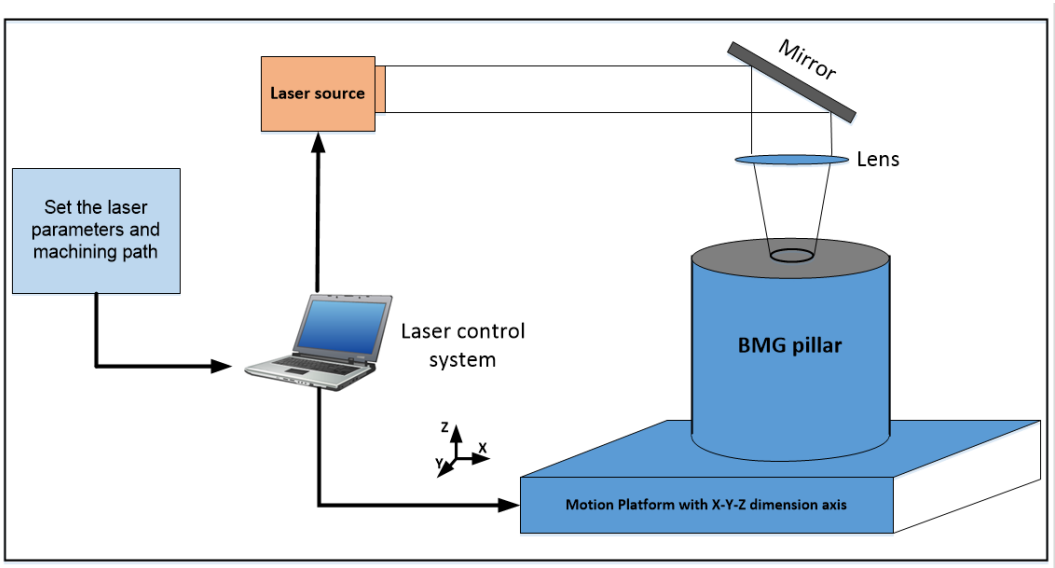

Figure 3.3: Schematic diagram of the nanosecond fibre laser system used in the present study.

3.3 Surface characterisation

3.3.1 Atomic force microscope (AFM)

An Atomic Force Microscope (XE-100 from Park Systems, South Korea) was used to measure the dimensions of single craters on the Vitreloy 105 amorphous alloy surface generated by the laser. This AFM device mainly consisted of a CCD camera, objective lens, clamping device, AFM head and nano-scale positioning stage. Since the maximum scan area of the AFM was a 40 by 40 μm square area, the AFM could only be used to measure the dimension of single craters. Thus, laser machined grooves and larger cavities could not be scanned with this

instrument. Obtained 3D AFM images were processed by the XEI software, also from Park Systems. In order to determine the size of a crater, its boundary was defined at the point where the height of the crater edge, prior to the crater rim, was the same as that of the height of the surface of the sample as illustrated with a typical example in Figure 3.4. Besides, three measurements of depth and diameter were taken for each crater and the average values were then used.

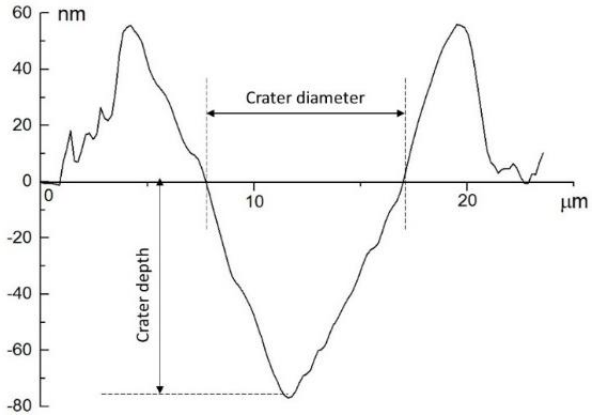

Figure 3.4: schematic diagram of the method used to evaluate the diameter and depth of the crater.

3.3.2 Contact surface profilometer

The bottom of a laser machined cavity is typically black and uneven, which seriously affects the reflection of light from an optical microscope. Thus, non-contact inspection techniques were not readily applicable for dimensional measurements of such features. Therefore, a contact surface profilometer (Talysurf Series 2, Taylor Hobson) was employed to measure the dimensions of the laser-machined cavities (shown in Figure 3.5). The Talymap software (Taylor Hobson) was employed for obtaining the machined cavity dimensional data. In this study, the laser-machined cavity was pre-set to be a 1 by 1 mm square and the surface profiler only used to measure the depth of the cavities after laser machined with one layer. With the dimensional information, the material removal rate (MRR)

of laser micromachining under one particular set of laser parameters was calculated to evaluate the machining efficiency.

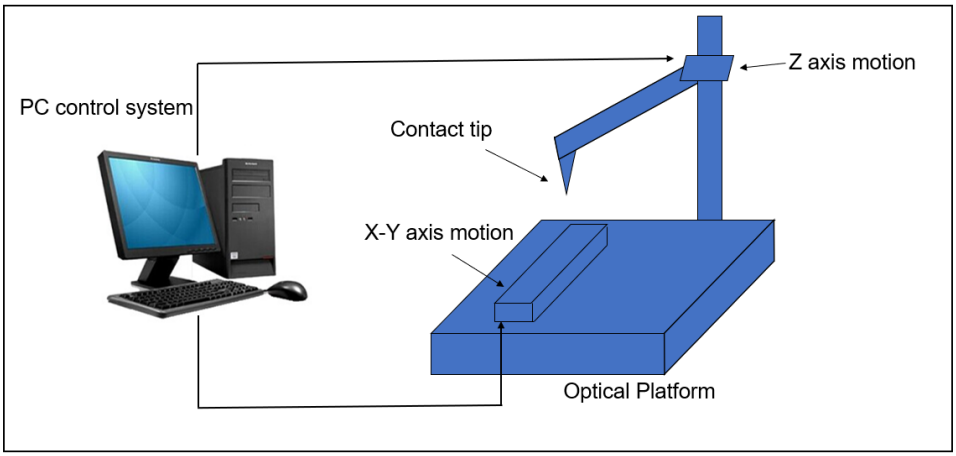

Figure 3.5: Schematic diagram of the Taylor Hobson Talysurf Series 2 surface profilometer.

The efficiency of machining a cavity was assessed by calculating the material removal rate for one layer, MRR, as follows (Wang and Zeng, 2007):

$$MRR = \frac{\rho \times L \times W \times d}{t_{processing}} \tag{3.3}$$

where ρ is the density of Vitreloy 105, L is the length of the cavity, W is the width of the cavity and d is the depth of a removed layer, which was measured with the Talysurf instrument, and $t_{processing}$ is the total processing time defined as the time when the laser beam is on.

For machining one layer, $t_{processing}$ is given by:

$$t_{processing} = N_{pulses} \times N_{tracks} \times t_p \tag{3.4}$$

where t_p is the pulse duration, N_{tracks} is the number of tracks in one layer and N_{pulses} is the number of pulses for one track.

The number of tracks in one layer is expressed as:

$$N_{tracks} = (W/D_s) + 1 \quad (3.5)$$

where D_s is the track distance between two adjacent laser tracks.

The number of pulses for one track of length, L, is given by:

$$N_{pulses} = \frac{L}{A} \quad (3.6)$$

where A is the distance between the centres of two successive laser pulses.

The value A is simply given by:

$$A = \frac{V}{f} \quad (3.7)$$

where V is the scanning speed and f is the pulse repetition frequency.

3.3.3 3D non-contact surface profiler

A Sensofar S mart series non-contact three-dimensional surface profiler (Sensofar Co., Barcelona, Spain) was used (see Figure 3.6), This instrument consisted of several key components which work together to obtain the useful surface information of the samples, namely a sensor head mounted on a motorized Z-axis, three magnification objective lenses (10×, 20×, 50×, 150×), a vibration-isolation table integrated with a manual X-Y sample platform, a computer installed with SensoMap™ and SensoScan™ (Sensofar Co., Barcelona, Spain) software. The SensoSCAN software was used to control the surface profiler and obtain the data, and the SensoMap was used to analyse the data, for example, calculating the surface dimensional parameters (roughness, height or volume).

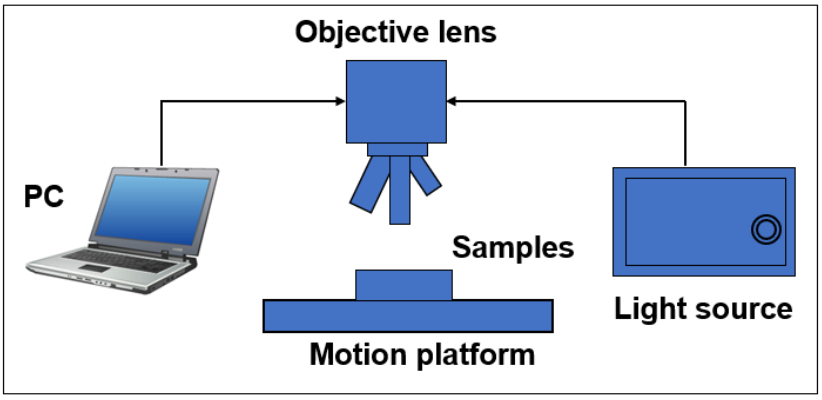

Figure 3.6: Schematic diagram of Sensofar non-contact three-dimensional surface profile.

This system can implement three different measurement technologies, namely confocal, interferometry and focus variation, combined into a single sensor head via a micro-display approach to measure the sample surface before and after laser processing. The SensoSCAN software can be employed to support the user in selecting the most appropriate measurement technique. The confocal mode has been developed for measuring smooth to very rough surfaces, which can provide the highest lateral resolution that can be reduced to 0.01 μm. The white-light vertical scanning interferometry (VSI) is a widely used and powerful technique for measuring surface characteristics such as topography or transparent film structure. It is suitable for the measurement of smooth to moderately rough surfaces and provides the nanometre vertical resolution. The Focus Variation technology has been developed for measuring the shape of large rough surfaces. The detailed comparisons between each technology are listed in Table 3.3.

Table 3.3: Technologies of the Sensofar S mart surface profiler (From Sensofar manual).

Technologies	Features	Applications
Confocal	smooth to very rough surfaces, micro-scale feature	Critical dimension measurements
White-light vertical scanning interferometry (VSI)	smooth surfaces, micro-scale and nano-scale features	Topography or transparent film structure
Focus variation	Large rough surface, high slope surfaces	Tooling measurements

Based on the abovementioned features and applications of the corresponding imaging technologies, the confocal mode was used for the dimensional measurement of laser-machined grooves, and the VSI technique was applied to the surface topography measurement and surface roughness calculation. As an example, Figure 3.7(a) illustrates the 3-D topography of a laser-machined groove on Vitreloy 105 when being scanned with the confocal mode. The sectional profile of the groove is presented in Figure 3.7(b). The colour bar represents the depth information of the laser-machined grooves. Since the sample surface is not very flat, a plane tilt correction was carried out using the SensoMap software before obtaining the final sectional profile. The depth and width were measured for three consecutive grooves, and the average value was taken to represent the dimensions of the laser-machined grooves under a given set of parameters.

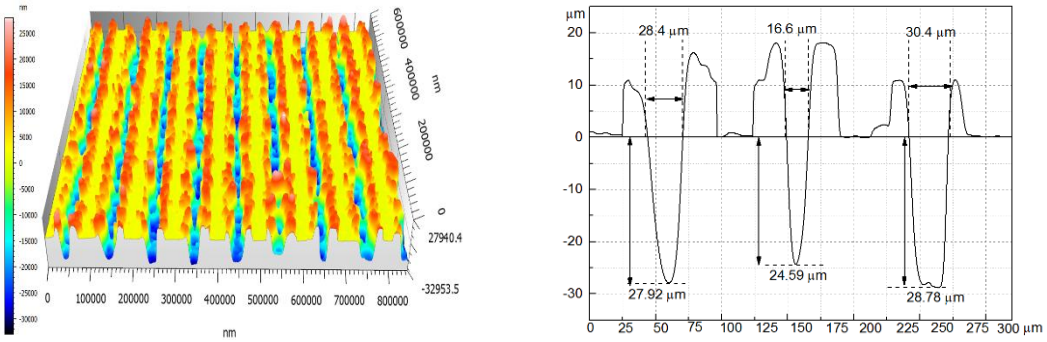

(a) (b)

Figure 3.7: (a) Example of the Sensofar measurement of a groove machined by the multiple laser pulses with the laser fluence of 30 J/cm^2, scanning speed of 100 mm/s and at 20KHz; (b) Sectional profile of Fig. 3.7 (a).

3.3.4 Scanning electron microscope (SEM)

In order to acquire more information about the laser processed surfaces, a high-resolution method, i.e. scanning electron microscopy, was exploited. Compared to 3D optical microscopy, SEM can provide a wider range of focal depths, improved resolution and a simple interpretation of obtained images. A field-emission scanning electron microscope (1540XB from Carl Zeiss, Germany) was used in this study to examine the surface topography of the processed specimens from a qualitative perspective. Two kinds of signal, secondary electrons (SE) and backscattered electrons (BSE), can be detected. The BSE detector is particularly suited to distinguish different phases, providing imaging information about the composition distribution of a sample. The SE detector is beneficial for the surface topography inspection. In this study, both of these two signals have been used. In addition, a focused ion beam gun and energy dispersive X-ray detector were also incorporated into this system.

3.3.5 Surface microstructure and chemistry analysis

As described in section 3.1, the amorphous structure of the as-cast Vitreloy 105 specimens was confirmed by X-ray diffraction (XRD). The surface microstructural evolution of Vitreloy 105 after laser surface treatment was also characterised via XRD. The instrument used was a Philips PW3830 X-ray diffraction equipment using Cu-Kα radiation (λ=1.789 Å) with a scanning speed of 0.02°/s at the generator settings of 35KV, 40mA in a continuous mode. The data was collected over a 2θ range of 5° to 90°, a counting time of 0.5 s/step. The data were analysed using the X-pert Hi score plus software.

As discussed earlier, the surface wettability of materials also depends on the chemical composition distribution of the specimen surface to some extent. The surface chemistry analysis of the Vitreloy 105 specimens without and with laser processing was conducted via a qualitative method, energy dispersive X-ray (EDX) and a quantitative method, X-ray photoelectron spectroscopy (XPS). EDX analyses were achieved by an energy dispersive X-ray (EDX) micro-analyzer (INCA X-sight, Oxford Instruments, UK) which was integrated into the SEM. The mapping figure of each chemical element was obtained using the associated INCA software. In addition to EDX, the more precise elemental analysis method was performed by XPS using an ESCALABTM Xi+ spectrometer microprobe (Thermo Fisher Scientific, USA) to evaluate the chemical composition variation of BMG samples before and after laser processing. The X-ray spectra were acquired using the monochromated Al Kα X-ray source. All XPS data were analysed with the XPS PEAK4.1 software using the Shirley backgrounds. Both the survey and narrow scan spectra were recorded from an analysis area 300 × 700 μm^2 on the surface of inspected amorphous alloy samples.

3.4 Wettability analysis

3.4.1 Contact angle measurement

The wettability of a solid surface can be quantified by contact angle measurement, which can be described by the Young-Dupre equation, as illustrated in Figure 3.8 and described as follows:

$$\gamma_S = \gamma_{SL} + \gamma_L \cos\theta_c \tag{3.8}$$

where θ_c is the equilibrium contact angle, γ_S is the surface free energy of the solid, γ_{SL} represents the interfacial tension between the solid and liquid phase and γ_L is the surface tension of the liquid. Due to the size limit of the available Vitreloy 105 samples (i.e. only 3 mm in diameter), the dynamic contact angle measurements (advancing and receding contact angle) were not carried out. Therefore, the static contact angle was taken as the equilibrium contact angle in this study.

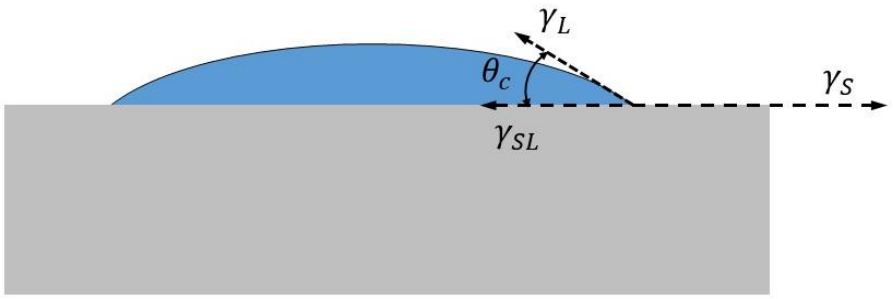

Figure 3.8: Schematic diagram for the contact angle of a liquid drop on a solid surface according to Young's equation.

Static contact angles (SCA) were measured by a contact angle goniometer (DataPhysics OCA100, DataPhysics Co., Germany) using the sessile drop technique along with a video-based optical angle measuring system at room conditions of constant temperature 25 ℃ and air humidity around 50%. Prior to the

measurements, the samples were cleaned with an isopropanol solution and left to dry in the desiccator at room temperature. A 0.5 µL droplet of distilled-deionized (DD) water was dispensed on the sample surfaces. The contact angles were captured by a camera when the dispensed droplet reached the equilibrium state on the surfaces. The contact angle was then determined by analysing the droplet images using the software SCA20 provided by DataPhysics. The establishment of the equilibrium state is considered regarding the measure duration when the drops remain steady on the sample surface (no spreading of the drop). The process of placing the liquid droplet on the sample surface is shown in Figure 3.9. When the liquid droplet was dropped on the specimen surface and stayed still, the side view was captured by a camera. The contact angle values calculated were the average value of the left and right CA as shown in Figure 3.10. As it takes a very short time to complete one measurement, the evaporation effect was considered to be negligible.

Figure 3.9: The process of placing the liquid droplet on the sample surface.

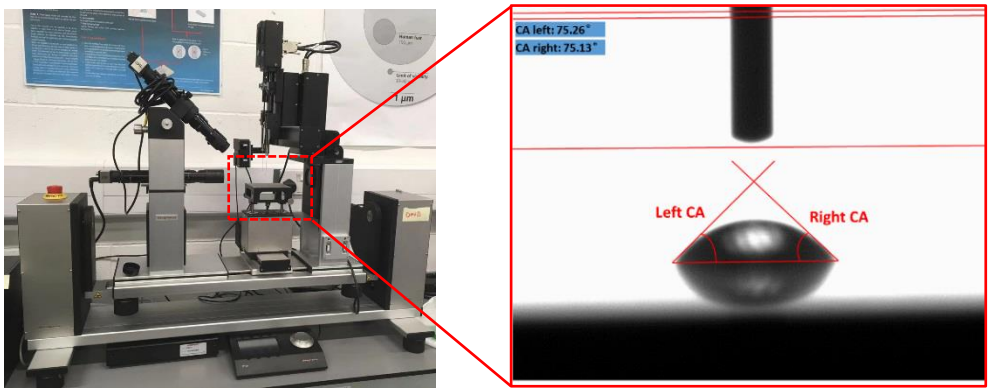

Figure 3.10: Contact angle measurement (Coventry University).

3.4.2 Surface free energy

The literature reports that the surface free energy also plays an important role in cell attachment and protein adsorption (Satriano et al., 2003). Therefore, the surface free energy (SFE) of all the sample surfaces was calculated in this study. In the open literature, the surface free energy is widely determined via the Owens-Wendt-Rabel-Kaeble (OWRK) method (Luo et al., 2011; Owens and Wendt, 1969). In the present work, the OWRK method was chosen for the calculation of the surface free energy as well (Waugh and Lawrence, 2010). In this method, the SFE of a solid is considered to be the compromise of two components: dispersive and polar components. The equation is as follows:

$$\gamma_{SL} = \gamma_s + \gamma_L - 2\sqrt{\gamma_S^d \gamma_L^d} - 2\sqrt{\gamma_S^p \gamma_L^p} \tag{3.9}$$

where γ_S^d is the dispersive component and γ_S^p is the polar component of the solid SFE, while γ_L^d is the dispersive part and γ_L^p is the polar part of the surface tension for testing liquids, γ_{SL}, γ_s and γ_L have already been defined in Equation 3.8. In combination with Young's equation, a linear equation ($y = mx + c$) can be obtained as follows:

$$\underbrace{\frac{\gamma_L(1+cos\,\theta_C)}{2\sqrt{\gamma_L^d}}}_{y} = \underbrace{\sqrt{\gamma_S^p}}_{m} \cdot \underbrace{\sqrt{\frac{\gamma_L^p}{\gamma_L^d}}}_{x} + \underbrace{\sqrt{\gamma_S^d}}_{c} \tag{3.10}$$

The total surface free energy (SFE) γ^T is the sum of polar components γ^p and the dispersive components γ^d, as shown in Equation 3.11:

$$\gamma^T = \gamma^p + \gamma^d \tag{3.11}$$

It can be seen that two testing liquids are needed to calculate the surface free energy of a solid surface. Therefore, in the present study, apart from the deionized-distilled water, the ethylene glycol was also used as the testing media to quantify the surface free energy of Zr-based alloys before and after laser surface texturing. The polar and dispersive components of the surface free energy for the testing liquids employed are listed in Table 3.4.

Table 3.4: Surface free energy characteristics of the liquids.

Liquid	Dispersive energy (γ^d) (mN/m)	Polar energy (γ^p) (mN/m)	Total surface energy (γ^T) (mN/m)
Distilled-deionized water	21.8	51	72.8
Ethylene glycol	29	19	48

3.4.3 Work of adhesion

The work of adhesion is defined as the reversible thermodynamic work required to separate the solid-liquid interface from the equilibrium state to a separation distance of infinity, which is of great importance for solid-liquid contacts (Ebnesajjad and Ebnesajjad, 2013). The interfacial attraction increase can result in enhanced work of adhesion. Equation 3.12 shows the work of adhesion (W_a) calculation for a liquid-solid combination based on the OWRK equation:

$$W_a = 2\left(\sqrt{\gamma_S^d \gamma_L^d} + \sqrt{\gamma_S^p \gamma_L^p}\right) \tag{3.12}$$

The definition of $\gamma_S^d, \gamma_L^d, \gamma_S^p, \gamma_L^p$ have already been described previously in the current section.

3.5 Mechanical property measurement

Biomaterials made for orthopaedic implants typically experience very complex and severe conditions during servicing. These include corrosion, fatigue, abrasion and irregular loading, which may cause the failure of these devices (Chen and Thouas, 2015). Therefore, suitable mechanical properties are basic requirements of the materials for biomedical applications. As described in previous chapters, short pulse laser can be used to process the surface of BMGs samples to enhance their surface mechanical properties via the laser-induced rapid heating and cooling rate. In this study, Vickers micro-hardness tests, FIB-DIC based residual stress measurements and nanoindentation tests were conducted to evaluate particularly the hardness and shear banding behaviour of Vitreloy 105 after laser processing.

3.5.1 Vickers micro-hardness test

A Vickers micro-hardness instrument (Innovatest, Maastricht, Netherlands), set with a load of 2 kg and a dwell time of 10 s, was accessed to measure the surface Vickers micro-hardness distributions before and after laser surface melting treatment. The Vickers hardness (H_v) with the following expression:

$$H_v = 0.1891\, F/\mathrm{D}^2 \tag{3.13}$$

where F is the load (N) and D is the mean value from two lengths of the diagonal left by the indent (mm).

The hardness on ten randomly selected positions on each surface was measured to obtain a value for each sample. In order to compare the hardness data between

different processing conditions, the t-test procedure was applied where a P-value less than 0.05 was considered statistically significant.

3.5.2 FIB-DIC residual stress measurement

Due to the amorphous structure of BMGs, residual stress quantification is challenging using diffraction-based methods. Macro-scale destructive techniques, such as hole drilling, are also not applicable as these methods do not have the resolution required to capture the highly localised stresses within the first few micrometres of a sample surface.

For this reason, the method relying on micro-scale FIB milling and Digital Image Correlation (DIC) analysis was implemented (Lunt et al., 2015). Within this study the Zeiss 1540 XB FIB-SEM was used to incrementally mill micropillars on the surface of selected samples. The introduction of these traction free surfaces leads to stress relaxation within the core which is recorded by sequential SEM images of the sample surface. For example, a surface in a state of compression leads to pillar expansion during the milling process, with the inverse being true of a tensile surface stress. DIC is then used to quantify this strain change, which is compared with the results of finite element simulations in order to provide an estimate of the residual stresses originally present within the core.

The samples were mechanically mounted using SEM grip stubs in order to minimise drift during the FIB and SEM procedure. A trench width of 1 µm was used to determine the average residual stress within a 5 µm diameter pillar. At each data point a milling current of 500 pA and accelerating voltage of 30 keV were then used to incrementally remove 350 nm of material in the shape of an annulus. Between each milling step, tilt corrected secondary electron SEM images were collected using an imaging voltage of 5 kV and current of 2.6 nA. The brightness and contrast of these images were adjusted to maximise surface contrast of the imaged features.

In total 14 milling increments, and images were collected at each measurement location in a total time of approximately 30 minutes. A representative example of such a ring-core feature milled in this way in the current study is given in Figure 3.11.

Three nominally identical measurements were made on each sample selected for residual stress analysis. These were spaced at approximately 50 μm intervals in order to ensure that the stress state being recorded at each location was nominally influenced by <1% by the previous measurement (Lunt and Korsunsky, 2015).

In order to process the data, DIC was performed using a freely available MATLAB code specifically developed for this milling geometry (Eberl, 2019). Low resolution DIC was initially performed to correct for bulk drift of the samples, with a reduction factor of 5. Several thousand markers were then digitally selected across the centre of the core where strain relief is known to be uniform (Salvati et al., 2015). A correlation window size of 15 × 15 pixels was used for automated 2D tracking of the markers through the entire image set. Automated outlier removal following the routine implemented by Lunt et al. (2015) was then applied.

As a final step, least squares fitting was then used to obtain estimates of strain relief at each milling increment as well as the full strain relief at infinite depth. The following estimates of Young's modulus E=88.6 GPa and Poisson's ratio of v=0.37 (Bian et al., 2002) were used to convert these strain relief values into estimates of the average residual stress and associated confidence interval at each data point.

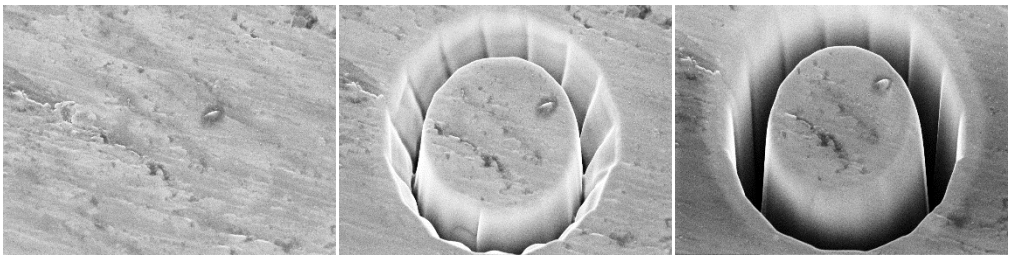

(a) (b) (c)

Figure 3.11: Representative SEM images taken during FIB milling of a ring-core feature on the as-cast sample: (a) original surface; (b) after milling two layers (c) upon completion of the process, i.e. after milling 14 layers.

3.5.3 Nanoindentation test

The plastic deformation of BMGs originates from local shear bands with micro/nano-scale characteristics (Huang et al., 2016). Since nanoindentation has the advantages of high temporal and spatial measurement resolution, small probing volume, and good compatibility for brittle materials, the literatures show that it can be been used for the investigation of the shear banding behaviour of BMGs (Fucheng Li, 2014; Fucheng Li, 2016; R.Maab, 2014). To be more specific, the serrated flows on the load-depth curves obtained from the nanoindentation instrument are directly related to the shear band operations (Huang et al., 2016; Schuh et al., 2007).Therefore, in the present study, the nanoindentation tests were conducted with a ENT-1100 nanoindentation instrument (Elionix Inc., Japan) using a Berkovich indenter under the load-control mode, while recording the load-displacement curve for each test. This nanoindentation instrument is shown in Figure 3.12. It mainly consists of a computer-controlled translation platform for lateral motions, an optical microscope, a nanoindenter and a computer, which is used to control the indenter and motion platform as well as to record the data. An indentation load of 100 mN and loading/unloading rates of 2 mN/s were selected.

The holding time at the maximum indentation load was set to be 1 s for all the indentation tests. For each case, three nanoindentation tests (1×3 arrays) were carried out. In order to avoid interaction effect, the distance between adjacent indents along the horizontal direction was set to be 50 μm.

Figure 3.12: ENT-1100 nanoindentation instrument (accessed at Keio University, Japan).

In order to highlight the difference of serrated flows between the different sample surfaces, the depth-difference method (Huang et al., 2012b) was employed. The mechanism behind this method can be summarised as:

$$\Delta h_1 = h_1 \tag{3.14}$$

$$\Delta h_n = h_n - h_{n-1}\ (n = 2, 3 \cdots) \tag{3.15}$$

$$\Delta P_1 = P_1 \tag{3.16}$$

$$\Delta P_n = P_n - P_{n-1} \tag{3.17}$$

where Δh_n, ΔP_n are the depth difference and load difference of the n-th sampling point (h_n, P_n), and (h_{n-1}, P_{n-1}) is the previous sampling point.

The loading rate and the sampling rate of the nanoindenter were kept constant during the indentation process. Thus, the load difference ΔP_n is a constant but the depth difference Δh_n changes with the penetration depth, particularly when

serrated flow events are visible in the *P-h* curves. As shown in the enlarged view of a typical serrated flow (Figure 3.13(b)), the value of depth difference Δh_n increases quickly during such event. This translates into one peak on the derived depth-difference curve. Thus, each peak on the depth-difference curve extracted from load-displacement (*P-h*) data denotes one serrated flow event. Moreover, the height of these peaks indicates the size of serrated flows. Therefore, the number and height of these peaks are good indicators that can be easily used to evaluate the surface plasticity of BMGs. An example of a depth difference-load curve extracted from the *P-h* data shown in Figure 3.13(a) in the load range of 10-100 mN is shown in Figure 3.14. It can be seen that there are many sharp peaks on the depth difference-load curve, which indicates a large number of serrated flows on the *P-h* curve.

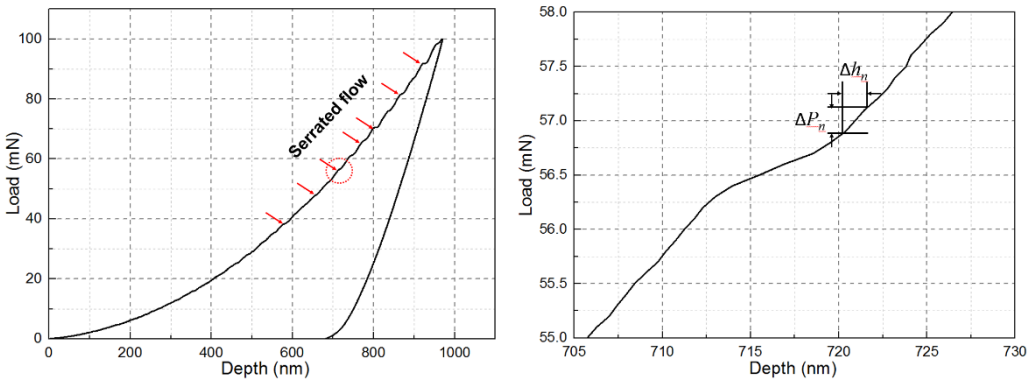

(a) (b)

Figure 3.13: (a) Example of load-depth (*P-h*) curves obtained on Vitreloy 105; (b) enlarged view of one serrate flow shown in (a).

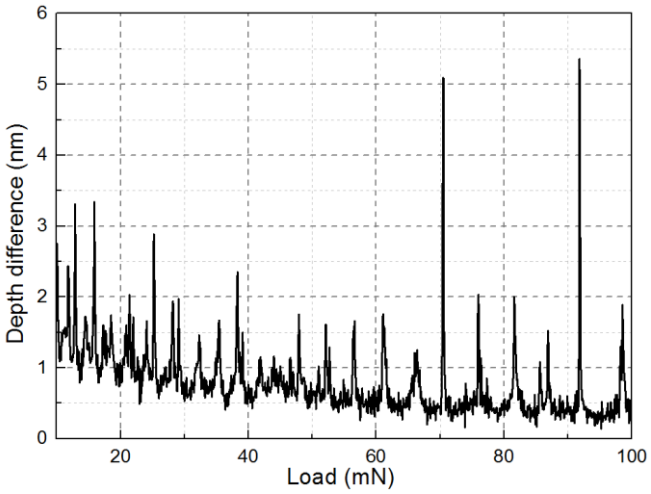

Figure 3.14: Example of a depth difference-load curve extracted from the *P-h* data shown in Figure 3.13(a), in the load range of 10-100 mN.

3.6 *In-vitro* bio-compatibility test

Prior to being used in clinical applications, bio-compatibility is an essential property to be tested for the sake of avoiding any adverse effect in the human body. This is typically assessed through *in-vitro* cellular response and *in-vivo* animal implantation (Li and Zheng, 2016). In general, *in-vitro* test is always the first step to evaluate bio-compatibility. In the present study, the cell viability test, cell morphology and attachment observation on the Vitreloy 105 samples with and without laser surface texturing treatment was conducted.

3.6.1 Cell culture

Human MG-63 osteoblast-like cell lines were used in this study. Cell lines (passages 28-32) were cultured in the T75 cell culture flasks in the cell medium, comprising of alpha minimum essential medium (α-MEM) supplemented with 10% (v/v) heat-inactivated fetal bovine serum (FBS), 100 units/mL penicillin G sodium, 0.1 μg/mL streptomycin sulfate, and 0.25 μg/mL amphotericin. The cells were

incubated in a 5% CO_2 balanced air incubator (shown in Figure 3.15(a)) at 37℃. The cell culture medium was changed every 2-3 days. When changing the medium, the old cell medium was extracted by the pipette first, and then the cells were washed by the PBS three times before adding the fresh medium. Before cell passaging or cellular behaviour studies, the confluent cells were detached using the Trypsin, and the cell counting was conducted. During the cell counting process, the Trypan Blue was used to stain the cell and the haemocytometer was used in the invert optical microscope (shown in Figure 3.15(b)). Afterwards, the corresponding amount of the fresh culture medium was added to re-suspend the cells to obtain an intended density of cell suspension. Cells were cultured until approximately 80-90% confluent before being used for subsequent experiments. All the above-mentioned procedures were conducted in the hood (shown in Figure 3.15(c)) to avoid the contamination. All the *in-vitro* bio-compatibility tests were conducted in the Cardiff School of dentistry.

Before seeding the cells on the sample surface, all the BMGs samples were autoclaved for approximately 15 minutes at 121 ℃ and 1.4 bar and then put into the 96-well plates. Cells were seeded on the sample surface with the density of 15000 cells/cm^2 (approximately 1500 cells per sample) and incubated for 1h at 37℃ in 5% CO_2 incubator to allow attachment then flood the wells with the culture media followed by a 24 hours' incubation.

(a)

(b)

(c)

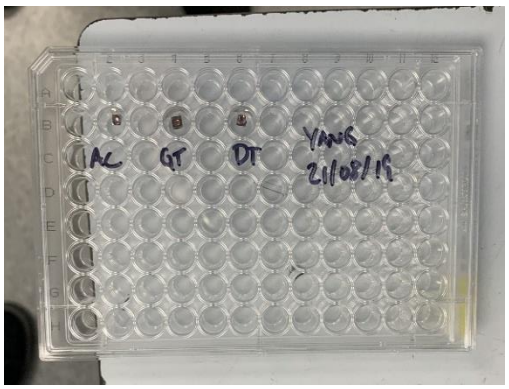

(d)

Figure 3.15: Devices used for cell culture (a) incubator (b) invert optical microscope (c) hood (d) cell-seeded samples in the 96 well plate (Cardiff School of Dentistry).

3.6.2 Cell viability

Cell viability was evaluated by the cell counting kit-8 (CCK-8) assay (Sigma-Aldrich, USA) due to its high detection sensitivity. This assay is based on the cellular conversion of a tetrazolium salt into a soluble formazan dye, which can be characterized by optical density measurements. The amount of formazan dye generated by the activity of dehydrogenases in the cells is directly proportional to

the number of living cells (Li and Ai, 2014; Li et al., 2013b). After culturing the cell-seeded samples for 24 hours in the incubator, the culture media was removed followed by the three times' wash with phosphate-buffered saline (PBS) to remove the non-adherent cells and then transferred to fresh 96-well plates. Afterwards, a 10 μL CCK-8 reagent was added to each well that contains the samples and incubated for 3 hours according the reagent instructions. Finally, colorimetric measurement of the formazan dye was performed on a microplate reader with an optical density reading at 450 nm. An empty well with no cells was used as the negative control and a well with 1500 cells was used as a positive control. The experiment was repeated in triplicate (n=3) and the average OD value was taken as the final results for each group.

3.6.3 Cell attachment and morphology

Following the absorbance measurements, the medium was replaced with 10% formalin to fix the attached cells, which were then incubated at 4°C overnight. Following incubation, the 10% formalin solution was removed, and the cells were washed three times with tris-buffered saline (TBS). The cells were permeabilised with filtered 1% Triton X-100 (Sigma-Aldrich) for 30 minutes at room temperature (RT) and washed again with TBS three times, followed by blocking of non-specific binding sites with 1% normal horse serum (Vector Laboratories, UK) in TBS for 1 hour at RT. The actin filament of the cells was stained with the freshly prepared phalloidin stain (phalloidin fluorescein isothiocyanate labelled, Sigma-Aldrich) at a ratio of 1:50 in TBS and left for 40 mins at RT. Cells were washed 3 times with TBS and left for 5 mins to dry. Then, 10 μL of DAPI (Vectashield Hard Set, Vector Laboratories, UK) was added to each sample surface to stain the nuclei of the cells. Cell attachment and morphology analysis was performed on the fluorescent images obtained via an AX70 Olympus Provis fluorescent microscope.

3.7 Summary

In this chapter, details about the Vitreloy 105 materials as well as its nominal mechanical and physical properties were described first. Next, the components of the laser system utilised, and its operational characteristics were presented. Next, all the devices and methods employed for the characterisation of laser processed surfaces, including atomic force microscopy, contact surface profilometry, three-dimensional optical microscopy, scanning electron microscopy and the material removal rate characterisation procedure as well as surface microstructure and chemistry analysis were presented. Following this, a comprehensive description of the facilities and methods employed for surface wettability analysis was reported. The methods used to assess mechanical properties, i.e. hardness and shear banding behaviour, of Vitreloy 105 surfaces were subsequently introduced. Finally, the devices, methods and techniques of analysis related to cell culture and cell viability, as well as cell attachment and cell morphology, were outlined.

Chapter 4 Laser micromachining of the $Zr_{52.8}Cu_{17.6}Ni_{14.8}Al_{9.9}Ti_{4.9}$ bulk metallic glass: experimental and theoretical study

4.1 Introduction

The study presented in this chapter aims to contribute to research efforts in laser micromachining of BMGs using multiple moving pulses given the potential application of this technique for the manufacturing of micro-scale orthopaedic implants and biomedical devices. In this study, a ns fibre laser was used to machine the Vitreloy 105 Zr-based BMG with different laser parameters. A numerical simulation model that incorporates temperature-dependent thermo-physical properties and transient physical process was developed to predict the thermal behaviour within the Vitreloy 105 workpiece material. The underlying material removal mechanism and the influence of laser parameters were discussed according to the temperature evolution during the process. Finally, the material removal rate (MRR) achieved during laser milling operations was analysed based on the distance between two linear tracks once all other parameters were determined.

4.2 Numerical modelling and experimental procedures

4.2.1 Computational modelling

Given the very short laser material interaction time in the ns regime, it is difficult to conduct in-situ experimental measurements to capture accurately thermal effects during processing. For this reason, a finite element (FE) based numerical computational model was developed using the commercial software platform, COMSOL™. A two-dimensional theoretical model was created to analyse the temporal and spatial evolution of the temperature on the surface, and within, the target material. This model was also used to predict the thermal history of the BMG specimens and the dimensions of machined craters when processed under different laser parameters.

In the ns regime, when the laser beam is irradiated on a surface, the delivered energy is absorbed by electrons within the lattice during a time length, which is shorter than the pulse duration. This means that the energy absorbed by the target material can be regarded as being transformed instantaneously into heat (Ready, 1965; Vora et al., 2013). Therefore, the constitutive equation used in this study was the classic Fourier heat equation (Steen and Mazumder, 2010). In addition, it was assumed that the laser energy followed a Gaussian distribution both temporarily and spatially. Furthermore, the laser intensity decay along the depth of the irradiated material can be described by the Beer-Lambert Law (Hitz et al., 2012).

Consequently, the heat input, $P(x,t)$, in the developed model was expressed as follows:

$$P(x,t) = \alpha \times (1-R) \times P_0 \times e^{-2\left(\frac{x-x_0}{r}\right)^2} \times e^{-4\times ln2\times\frac{(t-t_0)^2}{(t_p)^2}} \times e^{-\alpha z} \qquad (4.1)$$

where α represents the absorption coefficient ($1/m$), R denotes the reflectivity, P_0 is the peak output intensity of the pulsed laser (W/m^2), x is the

coordinate along the surface of the irradiated material (m), x_0 denotes the centre of the laser spot (m), r is the radius of the laser beam at the focal point (m), t_0 represents the time at which the pulse starts (s), t_p is the full duration of the pulse at half maximum (s), and z is the coordinate along with the depth (m).

The peak output intensity, P_0, is described as:

$$P_0 = \frac{E}{(\pi r^2 \times t_p)} \tag{4.2}$$

where E is the pulsed laser energy (J).

In this model, the heat loss resulting from the latent heat of fusion and the induced ablation is considered by introducing a heat flux term, q_a, as a thermal boundary condition. This term is expressed as:

$$q_a = h_a(T_m - T) \tag{4.3}$$

where T is the material temperature, T_m is the melt temperature and h_a is a temperature-dependent heat transfer coefficient, which is expressed with a ramp function equal to zero when $T < T_m$ and that increases linearly as $T > T_m$.

The prediction of the topography of single craters was achieved using a COMSOL™ built-in module named “deformed geometry”. In particular, the volume in the material for which the temperature is computed to be above T_m is removed from the target material and the remaining profile is taken as the crater topography. In order to improve the modelling accuracy, the specific heat capacity, C_p $(J/(kg\ K))$, and the thermal conductivity, k $(W/(m\ K))$, of Vitreloy 105 were set to be temperature-dependent. However, the density, ρ, and the absorption coefficient, α, were kept constant. Natural convection cooling and radiation were also incorporated in the model as boundary conditions. The specific values of the material parameters used in this model have already been given in the previous

section 3.1 (shown in Table 3.1), and the remaining thermal parameters are shown in Table 4.1. Finally, to simulate multiple and moving pulses conditions, the workpiece was defined to be stationary while the heat input was also modelled in COMSOL™ to be applied at regular time and space intervals along the x coordinate. More specifically, for the space interval, the position of the centre point of different laser spots along the x-axis is simply obtained by the product between the scanning speed and the period, while its z coordinate is kept constant. Regarding the time interval between pulses, an analytical function, β, is used, which is defined as:

$$\beta = Gauss\_time(mod(t, 1/f)) \tag{4.4}$$

where $Gauss\_time()$ is a temporal Gaussian function of the laser-induced heat input, $mod()$ is a built-in periodic function available in the COMSOL™ software and f is the frequency of the pulsed laser. The function $Gauss\_time()$ is simply expressed as:

$$Gauss\_time = e^{-4\times ln2\times\frac{(t-t_0)^2}{(tp)^2}} \tag{4.5}$$

for which the parameters have been defined earlier in this section before.

Table 4.1: Thermal parameters used in the model (Demetriou and Johnson, 2004; Glade et al., 2000; Kannatey-Asibu Jr, 2009; Kolev, 2011; Steen and Mazumder, 2010).

Parameter (units)	Symbol	Parameter Value
Specific Heat Capacity (J/(kg K))	C_p	$(1/M) \times (24.9 + 11.2\times 10^{-3}T + 6.43 \times 10^{6}/T^2)$
Thermal Conductivity (W/m K)	K	$0.0163T + 0.84$
Heat transfer coefficient (W/m^2 K)	h_a	100
Emissivity	ε	0.35
Absorption coefficient (1/m)	α	1e^7
Reflectivity	R	0.83

Note: The value of the thermal conductivity, *k*, adopted in this study was that of Vitreloy 1 due to the absence of any published data for this thermal property for Vitreloy 105.

4.2.2 Nanosecond laser processing: specific experimental plan

The details of the laser system were described in the previous section 3.2. Thus, this section only presents the more specific experimental details implemented to address the objective of this chapter.

Several waveforms corresponding to different pulse durations were employed, namely 65 ns, 140 ns and 220 ns. A range of different laser fluence values, scanning speeds and track distances were also considered for each pulse length. Machined cavities could be achieved by translating the motion platform of the system in x, y and z directions. As illustrated in Figure 4.1, the laser beam travelled from a given starting edge of the area defining a cavity and moved to a finishing edge in the x direction for a distance L, thus completing one track. The first irradiated spot for the subsequent track was set at a distance increment, D_s, of several micrometres in the y direction. This process was repeated until a whole rectangular area was machined. Even though the depth machined in this manner for one layer is only a few micrometres, a cavity could be achieved in a layer-by-layer sequence using multiple linear laser tracks.

One issue in laser machining is the varying surface height of the specimen as material removal progresses, which affects the positioning of the surface at the focal length. To overcome this with the laser system utilised, the built-in probe was used to detect the specimen surface automatically after removing one layer. In order to guarantee the reliability of the data, all experiments were repeated three times. The detailed laser parameters used in the present study are shown in Table 4.2.

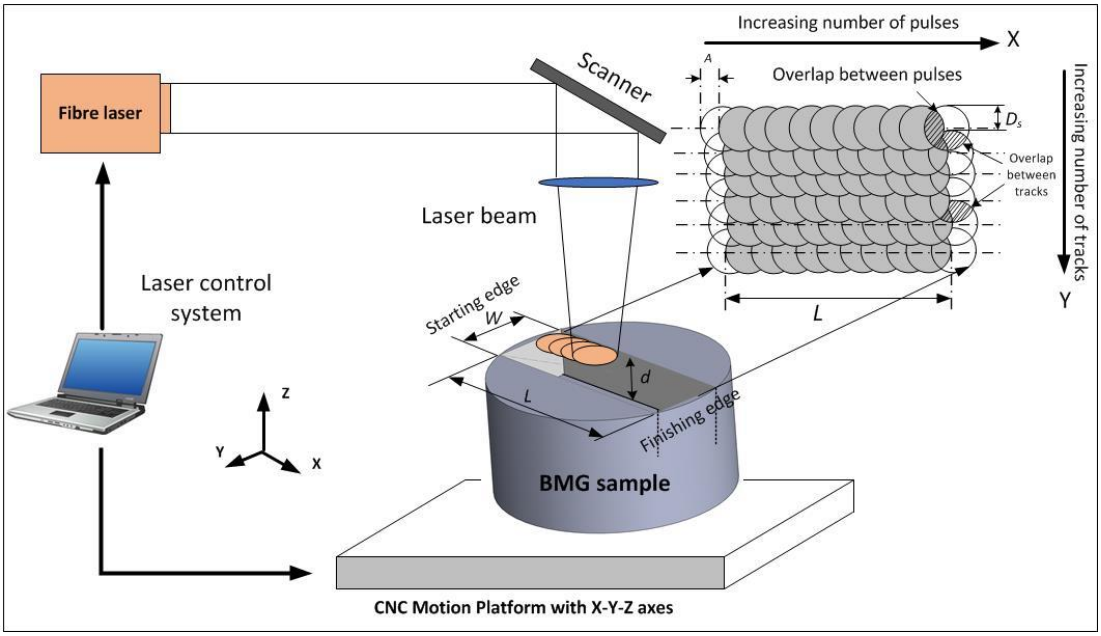

Figure 4.1: Schematic diagram of the laser machining process.

Table 4.2: Detailed laser parameter used for the laser irradiation experiments.

Wavelength (nm)	Spot diameter (μm)	Laser fluence (J/cm2)	Pulse duration (ns)	Frequency (kHz)	Scanning speed (mm/s)	Track distance (μm)	Machining operations
1064	32	30	220	35	-	-	Single pulse
		30	140	51	-	-	
		30	65	80	-	-	
		10	220	35	-	-	
		20	220	35	-	-	
		40	220	35	-	-	
		50	220	35	-	-	
		60	220	35	-	-	
		70	220	35	-	-	
		30	220	35	100	-	Multiple pulses; machining of grooves
		30	220	35	200	-	
		30	220	35	300	-	
		30	220	35	200	5	Multiple pulses; machining of cavities
		30	220	35	200	7	
		30	220	35	200	10	
		30	220	35	200	12	
		30	220	35	200	15	

4.3 Results and discussion

4.3.1 Single pulse study

Figure 4.2 shows the predicted thermal history on the surface of the BMG for different single pulses with various durations of 65 ns, 140 ns and 220 ns for a fixed laser fluence of 30 J/cm^2. The typical topography of a single crater for each laser irradiation condition is also included in this figure. As the heat source is assumed to follow a Gaussian distribution in space, the peak temperature is thereby in the centre of the laser spot. Hence, this point was always chosen to plot the data shown in this study for analysing the temperature evolution during laser machining. The theoretical model predicted that the surface temperature under all these three laser conditions reached values above the melting point. This is confirmed by the SEM micrographs also shown in Figure 4.2. In particular, it can be seen from this figure that melt pools were formed on all specimens and that the melted material could also be either partially or completely ejected from the craters. This is indicative of the formation of recoil pressure caused by the vapour from the melt pool. The partially ejected material is located on the edge of the crater and is still in contact with the solidified melt pool due to the surface tension force opposing its separation. Completely ejected material re-solidified outside the crater. The plotted data also show that under a fixed laser fluence, the peak temperature decreases as the pulse duration increases. This is a result of the higher peak power at lower pulse length. On the other hand, a reduced pulse duration led to a slight decrease in the diameter of the melted region. This should be due to the fact that a longer pulse provides more time available for the heat to propagate within the substrate and thus, for a larger volume of material to reach a temperature above the melting point.

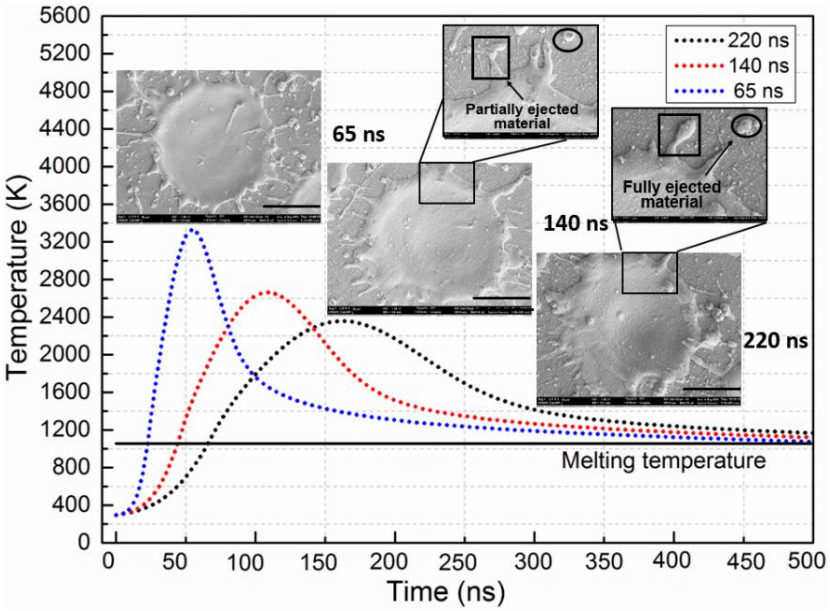

Figure 4.2: Simulated temporal thermal evolutions at a fluence of 30 J/cm^2 for pulse durations of 65 ns, 140 ns and 220 ns. The inset SEM micrographs show the corresponding topography of the single craters. The horizontal line shows the melting temperature. Scale bars: 30 µm.

The SEM micrographs displayed in Figure 4.3 provide more detailed surface topography data following single-pulse ablation with a duration of 65 ns at 30 J/cm^2. In particular, several laser-induced topographical features are reported in Figure 4.3(b), which include partially and fully ejected melt, surface ripples and vapour condensates. As suggested by the simulation data plotted earlier in Figure 4.2 under this specific laser processing condition, the surface temperature rises over 3000 K rapidly. This fast heating rate leads to the melt and vaporisation of the surface layer and the formation of a melt pool. In fact, the irradiance is estimated to be 4.6 x 10^8 W/cm^2 in this case, which may also initiate the formation of plasma (Steen and Mazumder, 2010). The recoil pressure over the melt pool leads to the ejection of molten material, leaving behind liquid droplets in a direction from the inside to the outside of the crater. The region of vaporised particles that condensed back onto the surface is observed both on and outside the re-solidified crater. The

surface ripples could be attributed to effects taking place on the surface as well as within the material. In particular, the surface effect may be due to the Kelvin-Helmholtz (KH) instability, which has been discussed by Liu et al. (2011b) in the case of Vitreloy 1. More specifically, KH-induced ripple features are typically generated at the interface between two fluids as a result of differences in their densities and velocities. For the work reported here, one of the fluids could be the vapour or plasma plume, and the other fluid would be the BMG material in its supercooled liquid state. Figure 4.3(c) illustrates the supercooled liquid region (SLR), which should form between the melt pool and the solid phase of the BMG. A second possible effect for the formation of ripples could be taking place within the material, also as a result of the recoil pressure. This pressure generates a radial force on the entire surface of the melt pool, which may be enough to “squeeze” the SLR. However, further work is necessary to test the validity of this hypothesis. Regardless of the specific cause for the formation of ripples, it is likely to be a consequence of the deformation of the material in the SLR. Using the thermal model developed in this study, it is estimated that the radial distance from the centre of the crater until the end of the SLR is 23 µm. As shown in Figure 4.3(d), this boundary corresponds to the isotherm for which the temperature is equal to T_g. This theoretical value is in relatively good agreement with the radial distance of 26 µm, measured experimentally from the SEM data, until the point where the surface ripples extend. Interestingly, no ripple patterns could be noticed on the specimens treated with longer pulses. Based on data displayed earlier in Figure 4.2, it is likely that this is due to a combination of two factors: (1) the longer pulse duration induced more material to be ejected from the melt pool and then to redeposit on the surface, possibly covering the ripple patterns and (2) the peak temperature of the material achieved with the longer pulse duration is lower than that reached with the shorter pulse length of 65 ns, which may affect the recoil pressure of the plume.

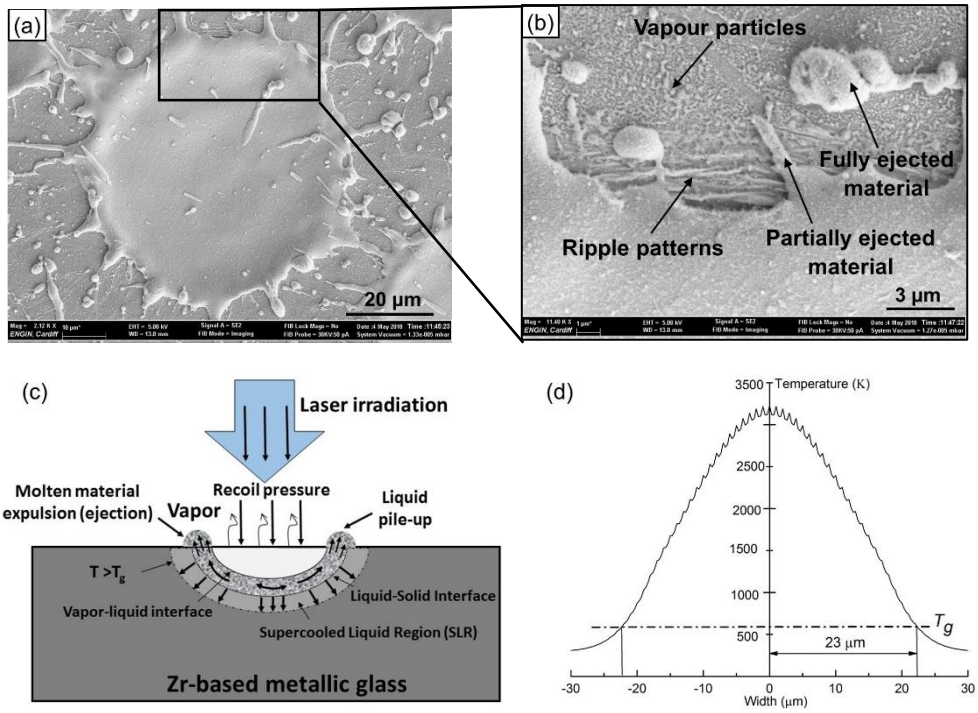

Figure 4.3: (a) Full view and (b) close-up view of the surface topography of a crater on the Zr-based BMG resulting from single laser pulse irradiation at 65 ns and 30 J/cm^2, (c) schematic diagram of the laser-material interaction process (d) predicted spatial temperature distribution on the centre of the irradiated spot based on the developed thermal model for irradiation at 65 ns and 30 J/cm^2.

Figure 4.4(a) shows the measured and simulated crater diameter and depth as a function of the laser fluence under the pulse duration of 220 ns. The simulated results were obtained by tracking the melt front and by assuming that all the melted material was removed from the crater. In spite of this simplifying assumption, it can be seen that the theoretical and experimental data generally agree quite well, except for the lowest fluence of 10 J/cm^2 and the higher fluence of 70 J/cm^2. In the first case, this discrepancy is most likely due to the fact that limited melt expulsion occurs at low fluence, which in turn would naturally result in simulated data overestimating the crater size, as is the case in Figure 4.4(a). This is also confirmed from the AFM topography displayed with Figure 4.4(b) where no splash or droplet

can be observed around the crater. Instead, a circular rim is visible on its edge which is caused by the hydrodynamic motion of the liquid phase. This motion is a consequence of the action from the vapour pressure on the melt and also, it results from the gradient in the surface temperature of the melt along the radial direction of the crater. In the second case, i.e. at the higher fluence of 70 J/cm^2, the discrepancy between the simulated and measured data, especially for the depth, could be the result of the possible formation of plasma, which would attenuate the delivered energy from the incident laser beam. Overall, it can also be observed that the data plotted in this figure follow an increasing trend when the laser fluence is raised and then, the rate of this increase tends to reduce after 30 J/cm^2 for the diameter and 40 J/cm^2 for the depth. This reduction in energy efficiency occurs when the ablation process changes from a melt-dominated to a vaporisation-dominated mechanism. This is also coupled with the possible initiation of plasma at the higher laser fluence values considered here. In addition to the discussion reported above regarding the discrepancies for the lowest and highest fluence data, it is also worth noting that between these two points, the predicted crater size is always a bit larger than the measured one. This may be due to a number of modelling assumptions, which have been made in this study. These include 1) the fact that the actual temporal beam shape of the fibre laser used is not Gaussian, 2) the thermal conductivity value employed being that of Vitreloy 1 and 3) the effect of the recoil pressure and surface tension force not having been taken into account. Figure 4.4(c) and (d) show the AFM topography of single craters for the fluence values of 30 and 40 J/cm^2, respectively. Figure 4.5 shows the corresponding section profile of a single crater corresponding to Figure 4.4(b), (c) and (d). The restricted range of motion for the AFM instrument utilised did not allow the scan to extend to areas where the droplets redeposited outside the crater. However, this was already observed in Figure 4.3 in the case of the 30 J/cm^2 laser irradiation. In summary, given the single pulse data reported here and based on cost and

efficiency considerations for potential micromachining applications, laser irradiation with 220 ns pulse length at 30 J/cm^2 was selected to conduct the subsequent multiple laser pulse operations.

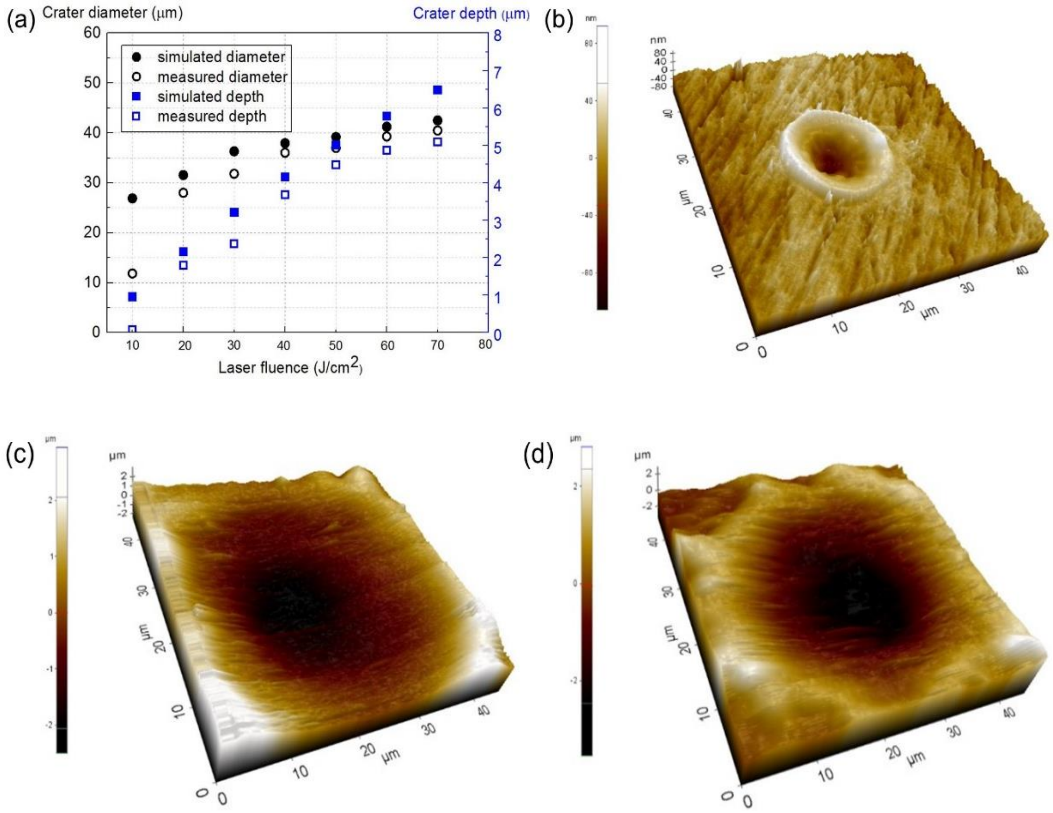

Figure 4.4: (a) Simulated and experimental crater diameter and depth as a function of the laser fluence for a pulse duration of 220 ns and AFM scans of a single crater generated with the laser fluence of (b) 10 J/cm^2, (c) 30 J/cm^2 and (d) 40 J/cm^2.

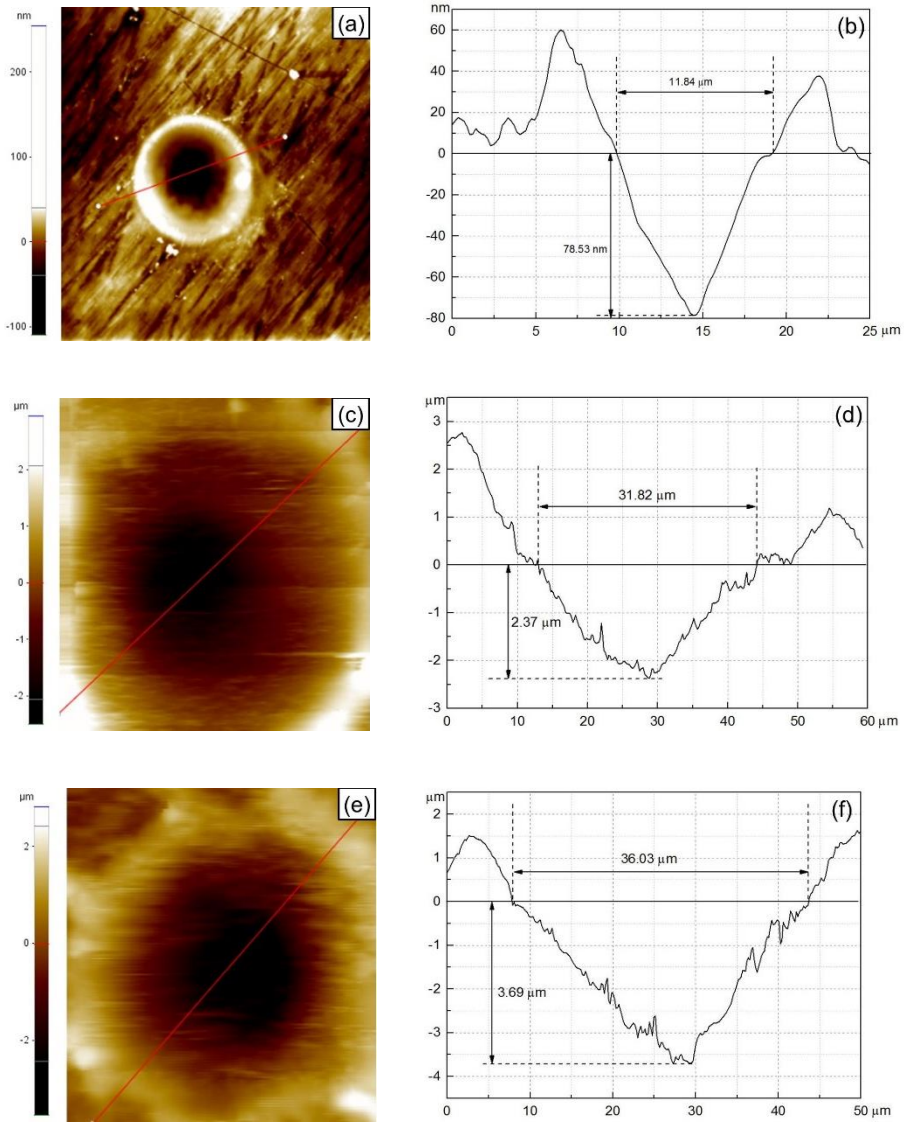

Figure 4.5: Location of cross-sections and corresponding profiles of single craters generated with the laser fluence of (a, b) 10 J/cm^2, (c, d) 30 J/cm^2 and (e, f) 40 J/cm^2.

4.3.2 Multiple pulse study

In this section, the effect of the scanning speed on the surface topography of individual machined tracks is investigated. Figure 4.6 shows secondary electron SEM micrographs of the Vitreloy 105 specimens with individual parallel tracks processed under a fixed laser fluence and pulse duration, i.e. 30 J/cm^2 and 220 ns, but using different scanning speeds, namely 100, 200 and 300 mm/s. These

corresponded to a pulse overlap of 91.1%, 82.1% and 73.2%, respectively. In addition, Figure 4.7 shows the corresponding back-scattered electron micrographs from Figure 4.6. In all cases, it is observed that the area between the laser tracks is a region dense in liquid droplets made of re-solidified molten material ejected from the grooves. In Figure 4.6(b), 4.6(d) and 4.6(f), it can also be seen that pores are formed within the micro-grooves, particularly for the lower scanning speed. These are caused by the viscous nature of the molten material during solidification. The distance between two adjacent laser tracks was 90 µm, which is much larger than the diameter of a single crater. This distance of 90 µm was set to eliminate the effect of the track distance on the surface topography and thus, to analyse results based on single groove data and observations. Qualitatively, it can be seen from Figure 4.6 that protrusions on the edge of the grooves, caused by the re-solidification of laser-induced molten material, are quite prominent for the lowest scanning speed of 100 mm/s (see Figure 4.6(a)). This results from the highest overlap between laser pulses, which in turn, increases the number of repeated cycles of melt expulsion for a given irradiated area along the track. This can be seen with the theoretical temperature data displayed in Figure 4.8, which reports the simulated successive heating and cooling cycles for a given point on the surface of the BMG specimen. In particular, this figure shows that a laser irradiated area always had enough time to fully solidify before the next incident laser pulse for the frequency used during this study, i.e. 35 kHz.

Figure 4.9 shows the topography of the machined grooves for the different scanning speeds considered. For the lowest scanning speed of 100 mm/s, the average width of the protrusion was found to be 22.8 µm. With an increase in laser scanning speed to 300 mm/s, the width of the protrusions was found to decrease to 17.2 µm. The simulation results reported in Figure 4.8 also show that the temperature of the first irradiated site rises to 2300 K (Figure 4.8(c)), 2150 K (Figure 4.8(b)) and 1950 K (Figure 4.8(a)) upon the delivery of the second laser

pulse, for scanning speeds of 100 mm/s, 200 mm/s and 300 mm/s, respectively. Hence, with an increase of the scanning speed from 100 mm/s to 300 mm/s, the effect of a subsequent laser pulse is reduced with respect to the induced temperature rise. As a result, the amount of molten material ejected from the melt pool is also reduced. Consequently, the width of the protrusion also decreases with the increase in scanning speed. In addition, based on the data displayed in Figure 4.9, the average width of the grooves was measured to be 29.4 µm, 29.4 µm and 30.87 µm while the depth was 27.33 µm, 11.33 µm and 8.2 µm, for increasing values of scanning speed considered here. Moreover, it can also be observed qualitatively from the SEM micrographs that the depth decreases with the increase of scanning speed. Compared to a single pulse generated under the same laser fluence and pulse duration, the widths of the groove under different scanning speeds are a slightly smaller than that of the single pulse while their depth values are much larger.

A number of comments can be made based on the observation of the back-scattered electron SEM micrographs shown in Figure 4.7. In particular, a qualitative analysis can be made with respect to the presence of regions with darker contrast. Such contrast should be indicative of a lighter elemental composition and in the context of this study, this could provide clues about the presence of oxides given that the laser processing experiments were conducted in ambient air. Although the scope of this chapter is not concerned with the analysis of the effect of the laser processing on the resulting microstructure of the Vitreloy 105 specimens, it is useful to keep in mind that the presence of oxygen impurities promotes the recrystallization of glassy alloys during solidification from the melt (Lin et al., 1997). From a purely qualitative comparison of Figure 4.7(c) and Figure 4.7(e), there seems to be a slightly more pronounced contrast between the centreline of a groove and the protrusion at its edge when the scanning speed increases from 200 mm/s to 300 mm/s. This may suggest that a reduced scanning

speed could favour the introduction of oxide impurities. These possible phenomena would need further investigations but in theory, this would be in-line with the fact that a lower scanning speed leads to a higher density of heating cycles above the melt temperature for a given region as observed with the output from the thermal model reported with Figure 4.8. A closer examination of the surface of the grooves reveals that the darker regions are composed of cotton-like vapour particles. This observation is similar to data presented by Gasper et al. (2018). In particular, these authors reported that vapour nano-particles which were formed during laser powder bed fusion (LPBF) contained almost one-third of the element oxygen. This happened even when the process was conducted in a controlled environment with less than 0.1% oxygen. However, in contrast with this LPBF work, the re-solidified droplets observed in Figure 4.7 do not seem to exhibit any dark patches on their surfaces, which would reveal the formation of discrete oxide spots on the droplets themselves. This may be due to the fact that, the LPBF process is typically conducted either with a continuous wave laser or in the microsecond regime and thus, with a much larger pulse length than that used here. Interestingly, the re-solidified droplets, which can be seen in Figure 4.7, are covered by such cotton-like vapour particles regardless of the scanning speed utilised.

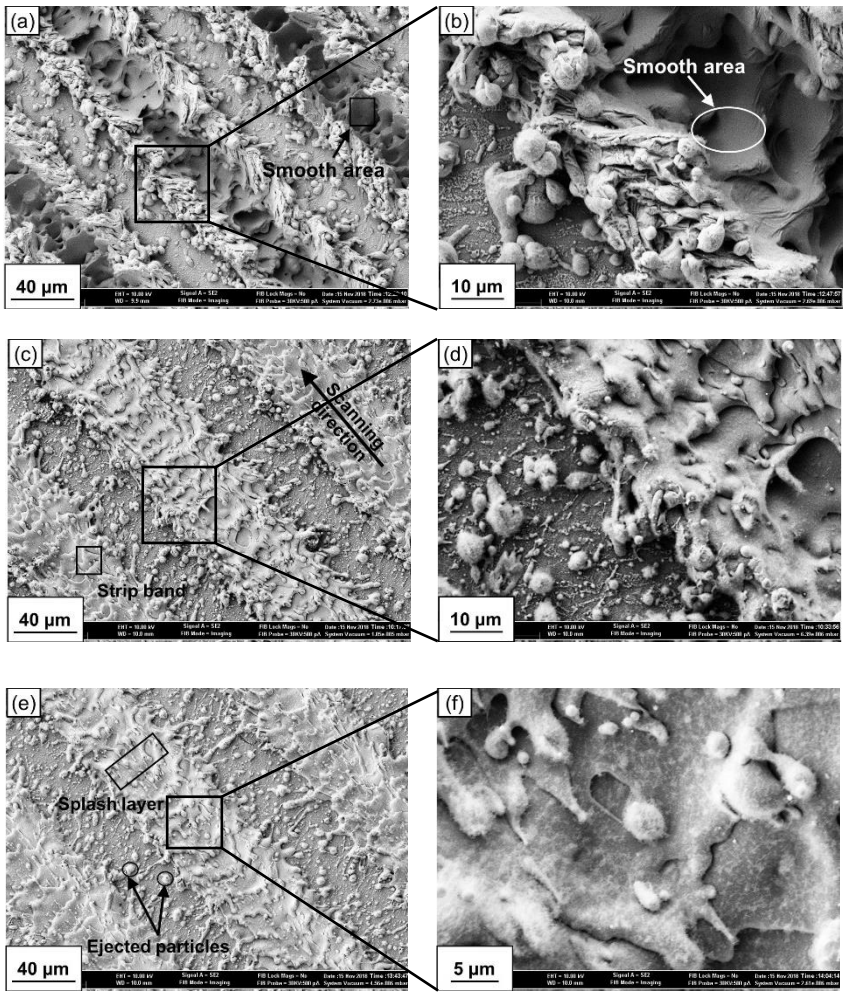

Figure 4.6: Secondary electron SEM micrograph on the surface of laser machined grooves for different scanning speed values of (a, b) 100 mm/s, (c, d) 200 mm/s and (e, f) 300 mm/s. The figures (b), (d) and (f) are the corresponding enlarged views on selected regions of figures (a), (c) and (e).

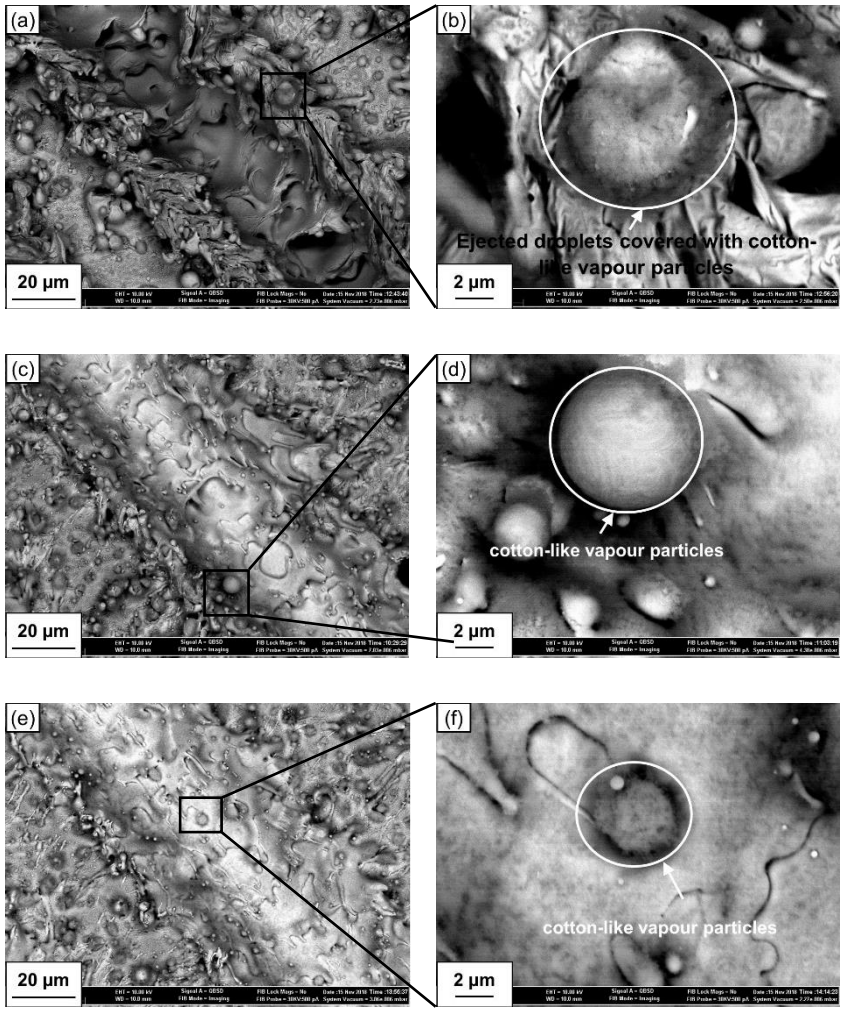

Figure 4.7: Back-scattered electron micrographs on the surface of laser machined grooves for different scanning speed of (a, b) 100 mm/s, (c, d) 200 mm/s and (e, f) 300 mm/s. The figures (b), (d) and (f) are the corresponding enlarged views on selected regions of figures (a), (c) and (e).

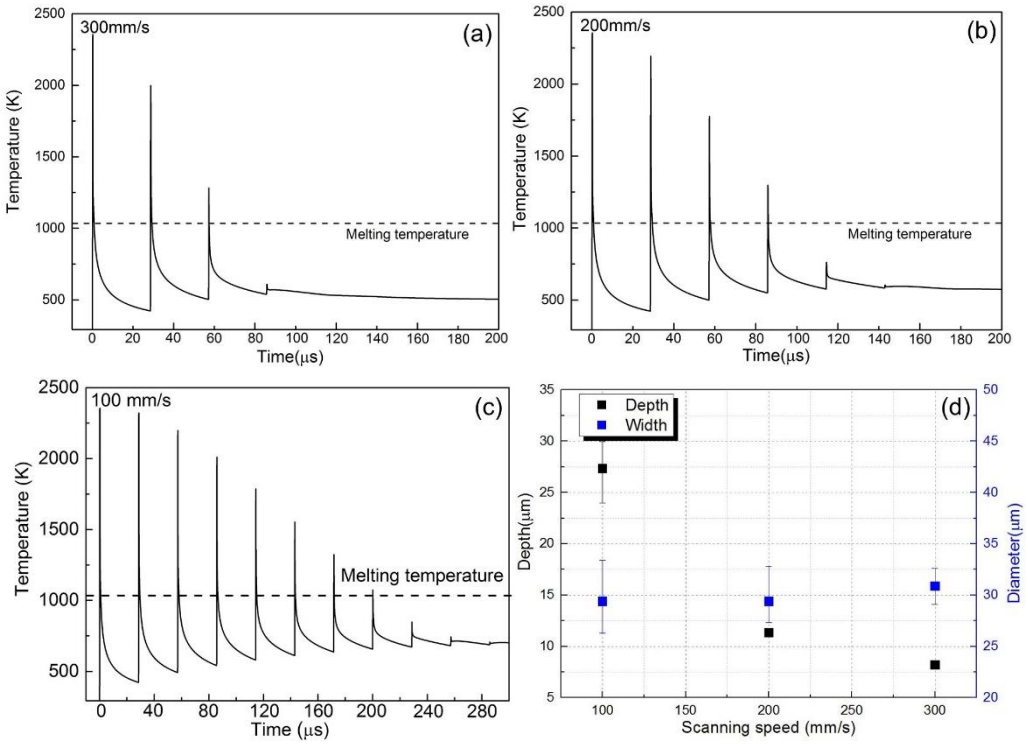

Figure 4.8: Simulated temperature evolution during multiple laser irradiation with different scanning speeds of (a) 300 mm/s, (b) 200 mm/s and (c) 100 mm/s.

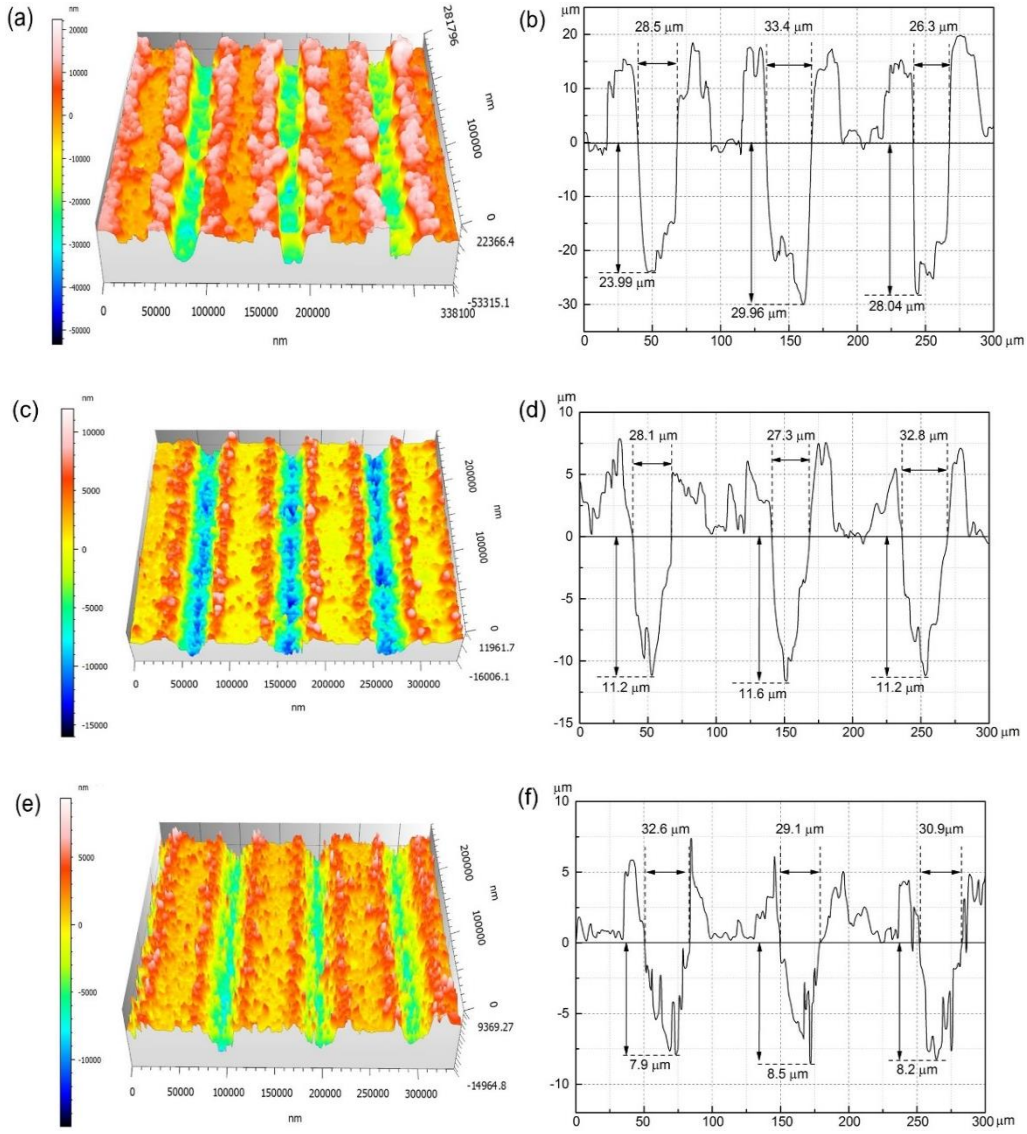

Figure 4.9: 3D profiles and their corresponding section profiles of the groove generated with the scanning speed of (a, b) 100 mm/s, (c, d) 200 mm/s and (e, f) 300 mm/s.

4.3.3 Machining efficiency

A final set of experiments was conducted to investigate the effect of the track distance on the machining efficiency. The material removal rate (MRR), calculated with Equation 3.3, was used as an indicator of the machining efficiency. Pockets with dimensions 2.4 mm x 1.2 mm were milled with a 220 ns pulse and based on the results obtained in the previous sections, a fluence of 30 J/cm^2 and a scanning

speed of 200 mm/s were selected. Given the pulse repetition frequency utilised, i.e. 35 kHz, this means that the overlap between two adjacent pulses along a track was 82% (with respect to the diameter of the laser spot size) and hence, that the specific distance between the centre of two consecutive pulses was 5.76 um (c.f. Equation 3.7). The total number of laser pulses, N_{pulses}, required to machine a single track was 411 (Equation 3.6). The required number of tracks, N_{tracks}, was calculated using Equation 3.5. MRR results against track distances values comprised between 5 µm and 15 µm are shown in Table 4.3 together with the measured depth achieved for one layer. Compared to the single line scan, the removed depth of the cavity is lower than that of the equivalent groove. This can be attributed to the fact that the protrusions created on the side of a single groove can lower the removing efficiency of the subsequent groove as these protrusions are not positioned at the focal point of the laser beam (Huang and Yan, 2017). The range of track distance values considered here corresponds to a track overlap comprised between 84.4% and 53.1%. It can be seen from Table. 4.3 that the removed depth decreases with the increase in track distance as one would expect, similarly to the observations made earlier in the case of varying pulse overlaps along a groove. Overall, with the increase in track distance, the removed depth reduces, which in turn lowers the removed volume of material for one layer, while at the same time, the processing time decreases which has the opposite effect on the MRR. In the experimental window reported in Table. 4.3, the MRR always increases with the increase of track distance. This means that the decrease of processing time dominates the evolution of the MRR.

Table 4.3: MRR values achieved as a function of the track distance.

Track distance, D_s (µm)	Percentage overlap between tracks	Removed depth for one layer, d (µm)	Total processing time, $t_{processing}$ (ms)	*MRR* (mg/s)
5	84.4%	9.03	21.79	8.03
7	78.1%	8.43	15.64	10.45
10	68.8%	8.15	10.85	14.56
12	62.5%	7.63	9.04	16.36
15	53.1%	7.04	7.23	18.87

4.4 Conclusions

Given the potential biomedical application of laser processing for the manufacture of BMG micro-components, this study combined theoretical and experimental investigations in a micromachining context, i.e. when multiple and moving pulse irradiations are applied. In particular, a nanosecond pulsed fibre laser system was employed to process Vitreloy 105. The material response during single and multiple pulse processing was studied under different parameters both theoretically and experimentally when considering laser material interaction phenomena and the evolution of simulated temperature data.

The output of the theoretical model showed a good agreement with the experimental results when analysing the dimensions of single craters. Besides, the simulated spatial temperature data could also be used to predict the width of the supercooled liquid region underneath the melt pool. Thus, the developed model was subsequently applied to multiple and moving pulses operations for interpreting experimental observations made about the effect of the scanning speed on micro-groove size and topography. In this case, it was seen that for the pulse repetition frequency utilised, i.e. 35 kHz, the laser-irradiated area had ample time to solidify before the next incident laser pulse, regardless of the scanning speed value selected. Thus, the Vitreloy 105 substrate was always subjected to repeated cycles of heating and cooling from its solid state. Such thermal cycles result in non-

standard conditions when considering crystal nucleation phenomena compared to the conventional synthesis of glassy alloys from the liquid state. In addition, the fact that vapour nano-particles were relatively easily formed under all scanning speeds should lead to increase the likelihood of oxygen impurities diffusing into the melt pool, which in turn, should affect the crystallisation kinetic. Finally, the effect of different track distances on the material removal rate was also investigated. It was found that the evolution of the material removal rate, for the fluence and pulse duration values identified, was dominated by the processing time rather than by variation in the volume of removed material.

Chapter 5 Laser texturing of the $Zr_{52.8}Cu_{17.6}Ni_{14.8}Al_{9.9}Ti_{4.9}$ bulk metallic glass for wettability modification

5.1 Introduction

The study presented in this chapter focuses on modifying the wettability of Vitreloy 105 with LST and gaining more insights into the understanding of the associated driving mechanisms, which is important to promote such amorphous alloys in bio-applications. The nanosecond fibre laser system was utilised to fabricate two types of surface structures, i.e. dimple and groove patterns. The topography of Vitreloy 105 surfaces irradiated with different laser parameters were measured by the 3D non-contact surface profiler and scanning electron microscope. The corresponding surface wettability was evaluated via the surface contact angle measurement, surface free energy and work of adhesion calculation using the contact angle goniometer. Finally, the surface chemistry of the laser textured surfaces was also investigated, using EDX mapping and XPS elemental analysis to evaluate the role of both surface topography and chemistry in the laser-induced modification of surface wettability.

5.2 Laser surface texturing: specific experimental plan

In the previous chapter (Chapter 4), the effect of pulse duration on the surface topography was investigated and the results showed that longer pulses could

remove a larger volume of material in a given time period. Therefore, the pulse duration of 220 ns was chosen for the study reported in this chapter. Unlike the micromachining of cavities presented in Chapter 4, achieving higher accuracy and quality of surface patterns is the aim of the laser texturing process here. Hence, a lower machining frequency of 20 kHz was chosen. The selected fluence values ranged from 10 to 50 J/cm^2. Two kinds of structures, i.e. dimples and grooves, were fabricated on the surface of the specimens via controlling the motion of the computer-controlled three-axis translation platform of the laser system. The scanning speed values considered, V, ranged between 100 and 300 mm/s. The lateral distance, A, between two subsequent laser pulses was determined and controlled via the scanning speed as follows:

$$A = V/f \tag{5.1}$$

The longitudinal displacement, D_s, was directly set by the parameter track distance and ranged from 60 to 110 μm. Compared to the spot diameter of 32 μm, this interval was always large enough, to avoid the overlapping of two neighbouring lines of laser irradiation. A schematic explanation for the laser texturing of these two types of structures is shown in Figure 5.1. In the case of the dimple structure, the values of D_s and A were set to be equal.

The parameters varied in the present study were fluence (F), scanning speed (V), track distance (D_s) in order to explore their influence on the surface topography and wettability of the Vitreloy 105 samples. Surfaces areas of 2 × 2 mm were patterned with different laser parameters and scanning strategies. The detailed laser parameters used in this study are shown in Table 5.1.

Table 5.1: Laser parameters for the fabrication of dimple and groove patterns on the surface of Vitreloy 105 samples.

Wavelength (nm)	Spot diameter (μm)	Pulse duration (ns)	Frequency (kHz)	Laser fluence (J/cm^2)	Scanning speed (mm/s)	Track distance (μm)	Surface patterns
1064	32	220	20	10	-	80	Dimples
				30	-	80	
				50	-	80	
				30	-	60	
				30	-	70	
				30	-	90	
				30	100	100	Grooves
				30	200	100	
				30	300	100	
				30	200	80	
				30	200	90	
				30	200	110	

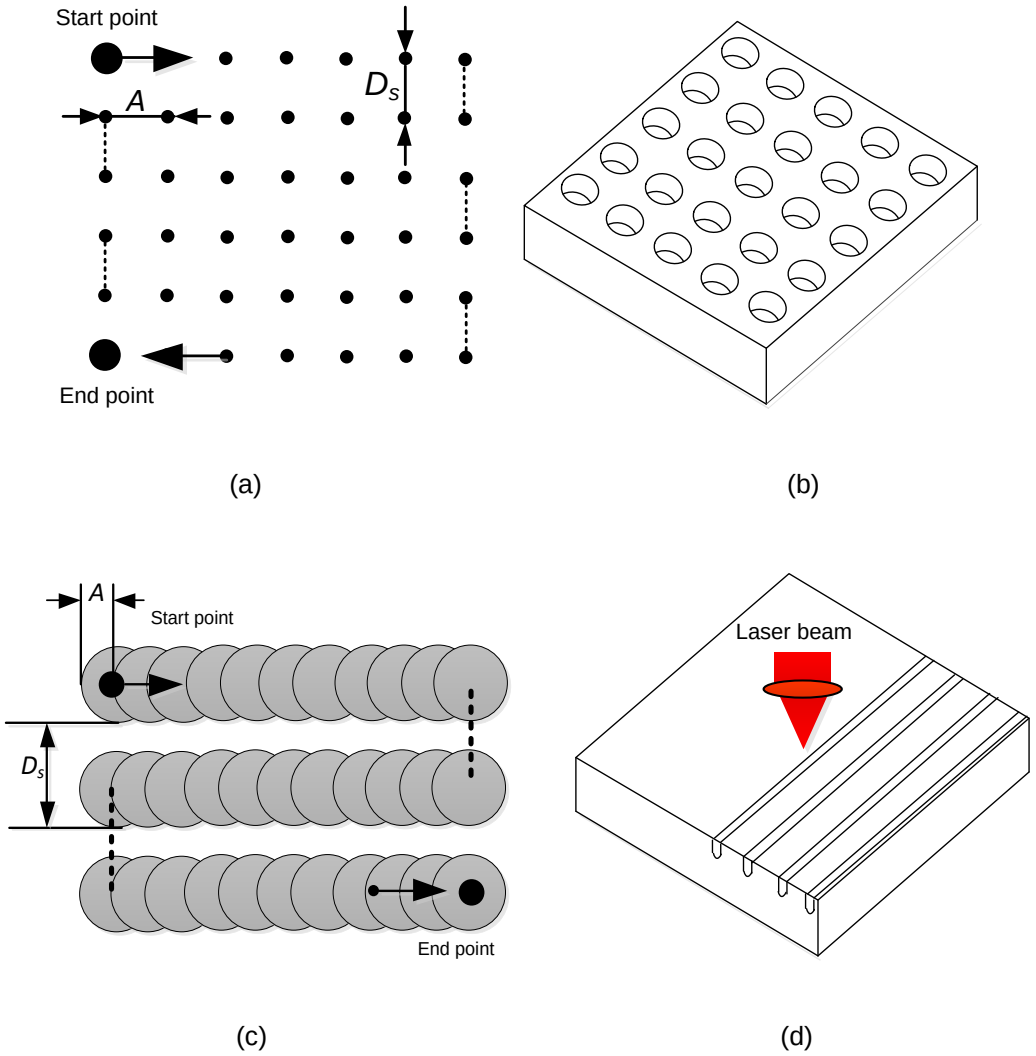

Figure 5.1: Schematic diagram of the laser surface texturing process for producing dimples and grooves on the Zr-based metallic glass surfaces. (a), (c) is the top view of the laser path for dimples and grooves, respectively. (b), (d) illustrates their corresponding sample surfaces after laser texturing.

5.3 Results and discussion

5.3.1 Surface topography analysis

This section reports on the results obtained when the scanning electron microscope (SEM) and the non-contact three-dimensional surface profiler (using

its confocal mode) were employed to characterize the surface topography variation of the Vitreloy 105 metallic glasses samples before and after laser texturing.

1. Effect of the type of laser-inscribed patterns on the surface topography

SEM micrographs and their corresponding 3D surface profiles of the laser textured surfaces are presented in Figure 5.2 and Figure 5.3, to display the typical topography generated on the surface of the Vitreloy 105 samples for the two types of microscale patterns considered, i.e. dimple and groove. The patterns presented in Figure 5.2 and Figure 5.3 were obtained with the same average fluence of 30 J/cm^2. To achieve the dimple pattern shown in Figure 5.2, the distance between two adjacent craters was set to be 80 µm as this resulted in the formation of single craters. The average diameter and depth of the single craters were 32.23 µm and 2.44 µm, respectively. It can be clearly noted that the Vitreloy 105 surfaces experienced heating, melting, vaporisation as well as material ejection and redeposition as can be seen with the occurrence of resolidified droplets on the sample surface. Compared to the roughness for the as-cast samples which was S_a= 0.065 µm, the roughness of the dimple sample surface was measured to be S_a= 0.17 µm. The pulse overlap value used to generate a groove shown in Figure 5.3 was 84%. This corresponded to a scanning speed of 100 mm/s. The track distance was set at 100 µm for this particular example. The average width and depth of the laser-ablated grooves were measured to be about 25.1 µm and 27.1 µm, respectively. Compared to the diameter of craters on the dimple patterned surface, the width of the grooves was a little bit smaller but the depth was increased significantly. This is due to the accumulation of single material removal events over a given area as a result of the overlap between two successive laser pulses. When comparing two grooves, a higher overlap means that the number of repeated cycles of melt ejection for a given length of the machined track is increased. In addition, compared to the dimple pattern, Figure 5.3 shows a higher occurrence of fully ejected and resolidified droplets around the grooves. The roughness of the

groove surface was characterised to be S_a= 8.51 µm, which is much higher than that of the dimple textured (0.17 µm) and of the as-cast samples (0.065 µm), as expected. Therefore, surfaces with the groove patterns display more significant changes in terms of surface topography among these two textured structures under the same laser fluence.

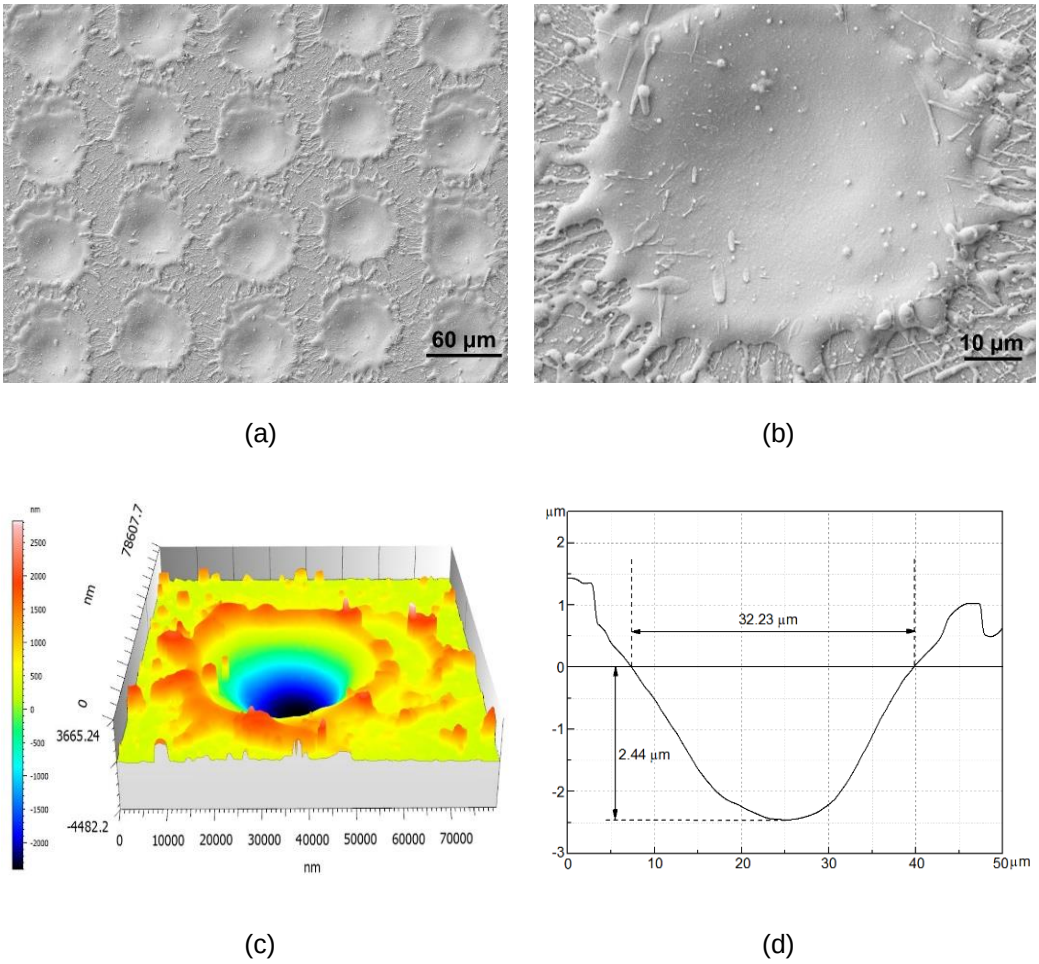

Figure 5.2: Dimple patterns. (a) General view; (b) Enlarged view of (a); (c) 3D profile of a typical dimple; (d) cross-section profile of the dimple.

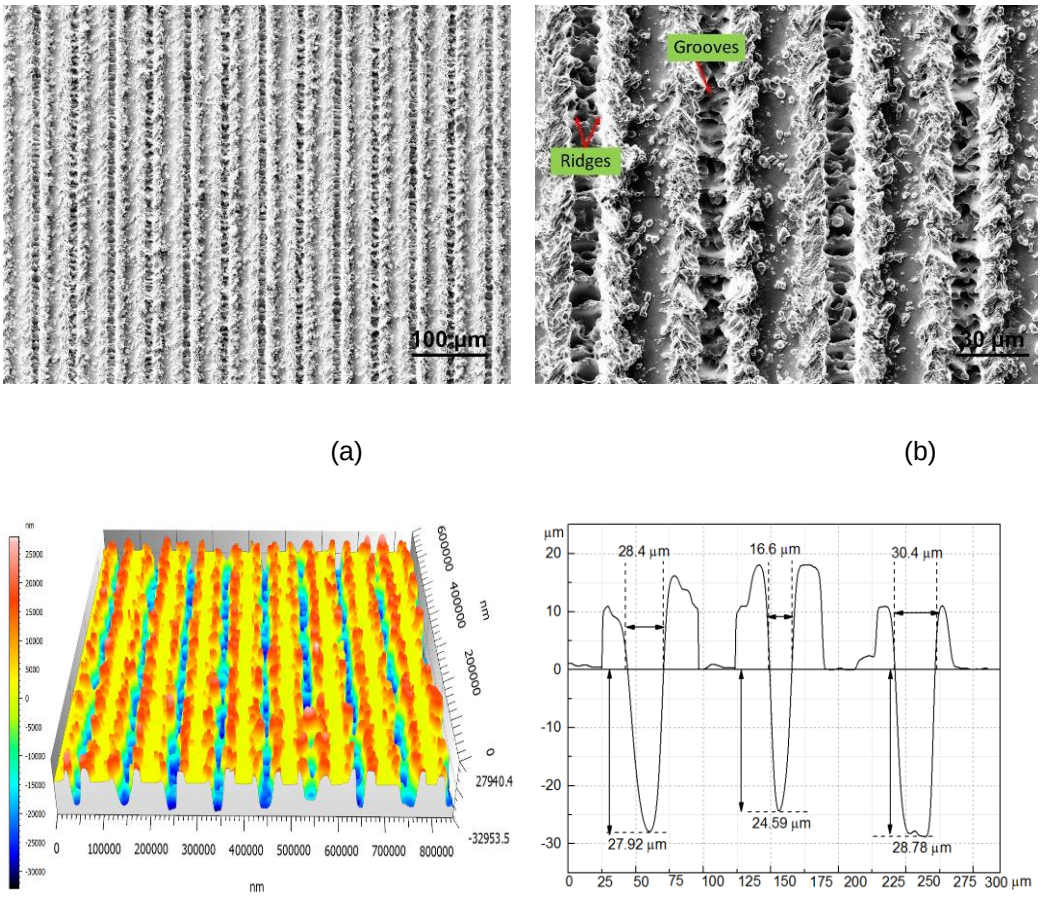

Figure 5.3: Groove patterns. (a) General view; (b) Enlarged view of (a); (c) 3D profile of the groove structure; (d) Cross-section profile of groove tracks.

2. Effect of the parameter "distance" on the surface topography

Yang et al. (2016) reported that the decrease in distance between grooves can lead to more distinct changes of surface topography, hence affecting the wettability. In the study reported in this chapter, it has to be clarified that the values of the track distance (D_s) and lateral displacement (A) in the case of the dimple pattern have been set to be equal and is henceforth referred to as "distance". The distance values were set to be 60, 70, 80, 90 µm for the dimple patterns and 80, 90, 100, 110 µm for the groove patterns. The surface roughness (S_a) of all the samples after laser surface texturing was measured and shown in Table 5.2. It can be seen from this table that the surface roughness for the groove pattern decreases with the

increase of distance and that this trend also generally applied for the dimpled surfaces.

The SEM images of the specimens treated under the same laser fluence of 30 J/cm^2 and the same scanning speed of 200 mm/s (for the groove patterns) but with different values of the parameter “distance” are shown in Figure 5.4 and Figure 5.5. For a small distance on the dimple-patterned surface, the craters are located next to each other and there is a very limited area of flat (i.e. unprocessed) surface between two neighbouring craters. With the increase of the distance, such virgin area became more visible on the sample surface. The increase in the proportion of the flat area on the sample surface results in the natural decrease in the value of S_a. Therefore, such variation in the proportion of the area not irradiated by the laser is the main reason that leads to the surface roughness variation for different values of the parameter “distance”. Given the fixed scanning speed associated with the results shown in Table 5.2, this explanation is also applicable to the surface roughness evolution of the groove patterned samples. In particular, an increase in the parameter “distance” also led to a reduction in surface roughness.

Table 5.2: The surface roughness of patterned samples with different values for the parameter “distance”.

Distance (μm)	S_a (μm)	
	Dimple pattern	Groove pattern
60	0.62 ± 0.06	-
70	0.23 ± 0.05	-
80	0.17 ± 0.03	3.79 ± 0.22
90	0.21±0.06	3.24 ± 0.08
100	-	3.00 ± 0.13
110	-	2.89 ± 0.17
as-cast	0.065 ± 0.01	

Note: the scanning speed used for all groove pattern results presented in this table was 200 mm/s. The errors reported correspond to one standard deviation.

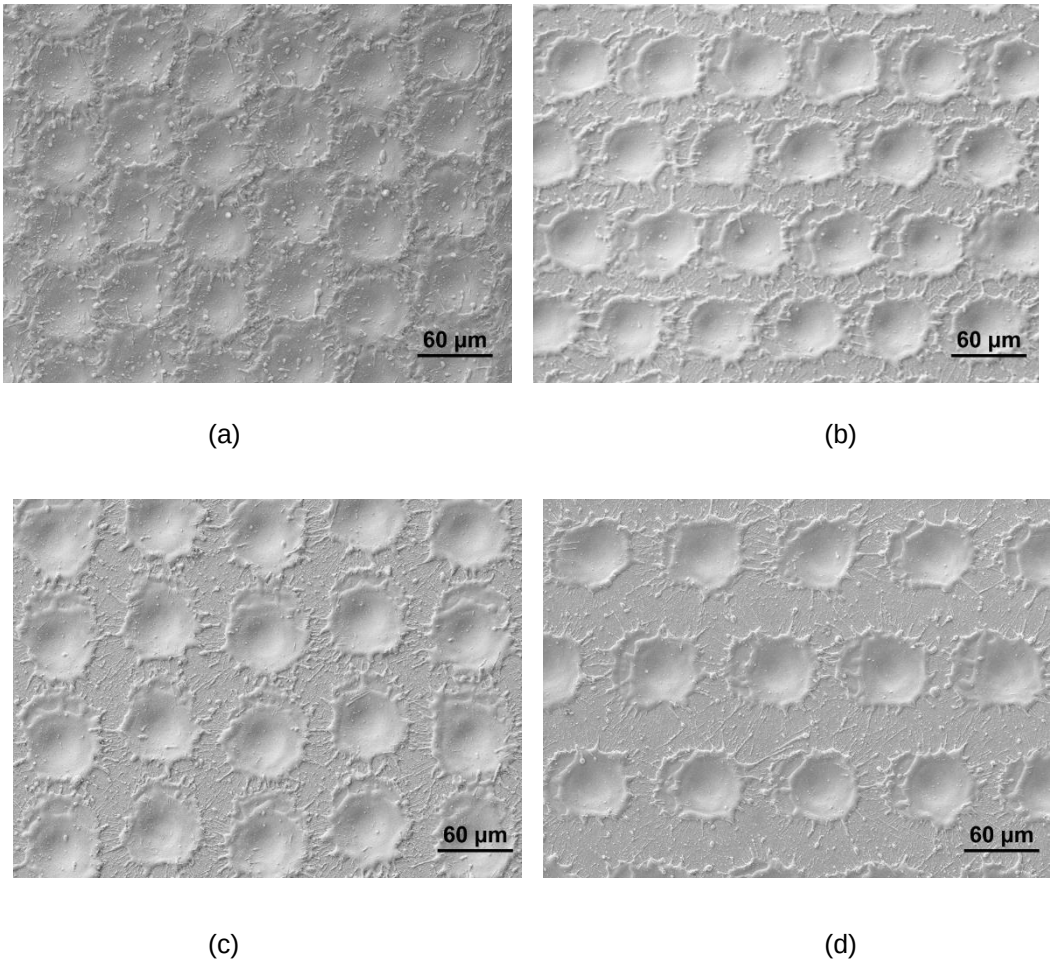

(a) (b)

(c) (d)

Figure 5.4: SEM micrographs of the groove-textured surface with the parameter “distance” set at (a) 60 μm, (b) 70 μm, (c) 80 μm, (d) 90 μm.

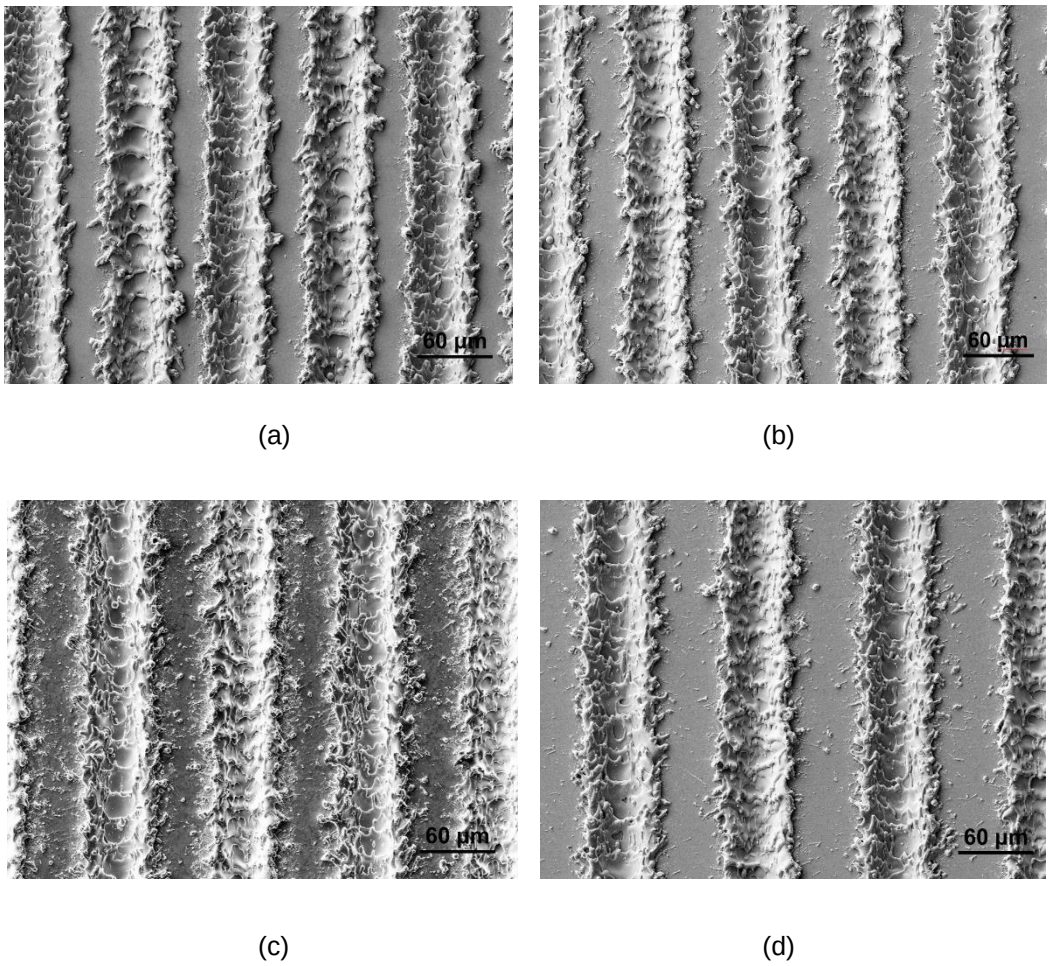

(a) (b)

(c) (d)

Figure 5.5: SEM micrographs of the groove-textured surface with the parameter "distance" set at (a) 80 µm, (b) 90 µm, (c) 100 µm, (d) 110 µm.

3. Effect of laser scanning speed on the surface topography of groove patterns

Figure 5.6 shows the SEM micrographs of the groove pattern generated using fixed values for the laser fluence, pulse duration and track distance, i.e. 30 J/cm^2, 220 ns, and 100 µm, but using various laser scanning speed, namely 100, 200 and 300 mm/s, which affects the pulse overlap. From this figure, it can be seen that the variation of the scanning speed changes the surface topography of the groove patterns significantly, which is a result of the different number of pulses delivered per unit length of the groove. More specifically, a higher number of laser pulses per unit length leads to more events of the molten material ejection, as is evident

from the qualitative observation of the density of redeposited material around the grooves in Figure 5.6. It was reported in the previous chapter that with an increase of the scanning speed from 100 mm/s to 300 mm/s, the temperature of the first irradiated site induced by the second laser pulse was decreased from 2300 K to 1950 K. As a result, the amount of molten material ejected from the formation of a second melt pool at that particular site is reduced. In addition, with a lower scanning speed, the bottom of the grooves presents a more distinct hierarchical structure, which can increase the effective surface area and hence improving wettability (Huang et al., 2016). Further, as shown in the inset of Fig. 5.6, the average width and depth of the grooves were measured to be 25.1 μm, 28.6 μm and 26.5 μm while the depth was 27.1 μm, 10.2 μm and 5.6 μm with the scanning speed increasing from 100 to 300 mm/s. Moreover, the roughness (S_a) was also greatly decreased from 8.51 μm to 1.91 μm with an increase of scanning speed. The detailed measured dimensions of the grooves and their corresponding roughness values are summarised in Table 5.3. Overall Figure 5.6 and Table 5.3 indicate that laser scanning speed has an important influence on the surface topography and surface roughness of the generated groove pattern. Therefore, selecting a suitable value of scanning speed should be critical in fabricating such patterns with a view of achieving optimal wetting property on the Vitreloy 105 amorphous alloy.

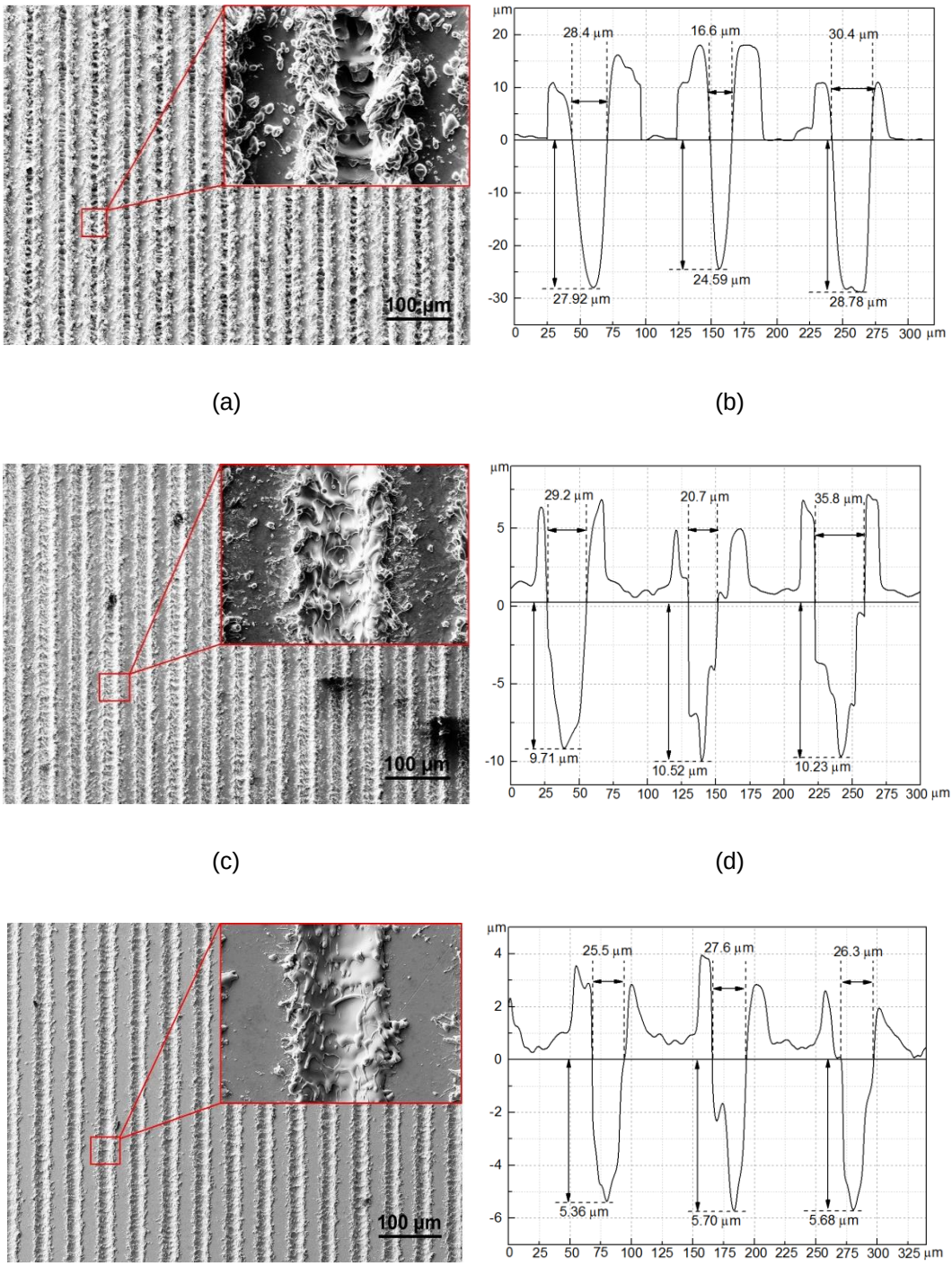

Figure 5.6: SEM micrographs of surface groove structures generated with various laser scanning speed: (a, b) 100 mm/s, (c, d) 200 mm/s and (e, f) 300 mm/s. The figures (b), (d) and (f) are the corresponding 3D topography and sectional profile of figures (a), (c) and (e).

Table 5.3: Dimensional and roughness data of surface structures created by various laser scanning speeds for the groove pattern.

Laser scanning speed (mm/s)	Groove width (μm)	Groove depth (μm)	Roughness S_a (μm)
100	25.1 ± 3.73	27.1 ± 1.11	8.51 ± 0.51
200	28.6 ± 3.79	10.2 ± 0.21	3.00 ± 0.13
300	26.5 ± 0.53	5.6 ± 0.10	1.91 ± 0.29

Note: the errors reported correspond to one standard deviation.

4. Effect of laser fluence on the surface topography of dimple patterns

As mentioned in the previous section, laser fluence should be an important factor in the resulting surface topography and roughness of samples with the dimple structures. SEM images, 2D cross-section profiles and measured surface data of such laser textured structures are shown in Figure 5.7 and Table 5.4, respectively. It can be seen from Figure 5.7 that when the laser fluence was 10 J/cm^2, the density of material redeposited on the edges of the craters was low and the craters were much shallower in comparison to higher laser fluence values. Thus, such laser fluence value leads to only slight changes in surface topography compared to the as-cast material. This is confirmed quantitatively by the surface roughness data reported in Table 5.4 and Figure 5.7(b). With the increase in the laser fluence, the diameter and depth of the craters became larger. However, the rate of increase in diameter with laser fluence is not linear and reached a plateau around 30 J/cm^2. This was discussed in the previous chapter and attributed to the ablation process mechanism transitioning from melting-dominated to vaporisation-dominated. When the laser fluence reached 50 J/cm^2, Figure 5.7(e) shows that a large volume of molten material splashed and re-solidified around the craters. This resulted in a much rougher surface compared to the other two fluence values considered. As expected, laser fluence has an important impact on the surface topography and roughness of the dimple textured surfaces. Thus, for fabricating dimple patterns

with desired wetting property, the laser fluence should be carefully considered as well.

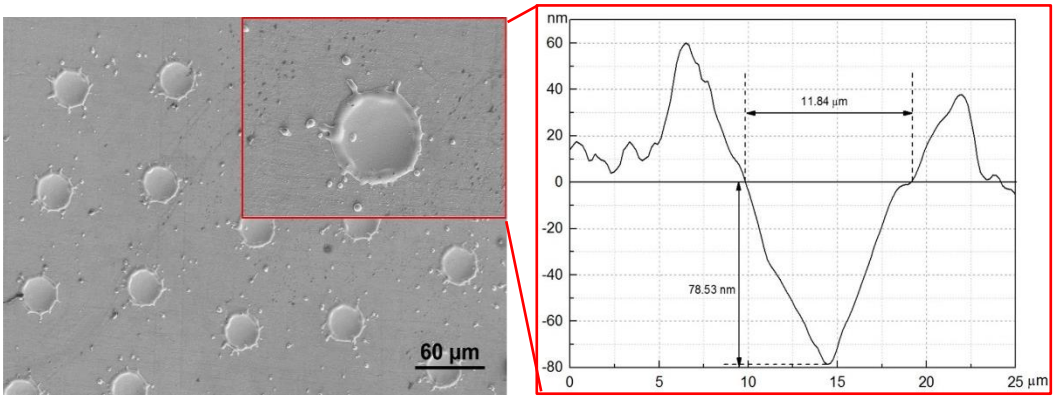

(a) (b)

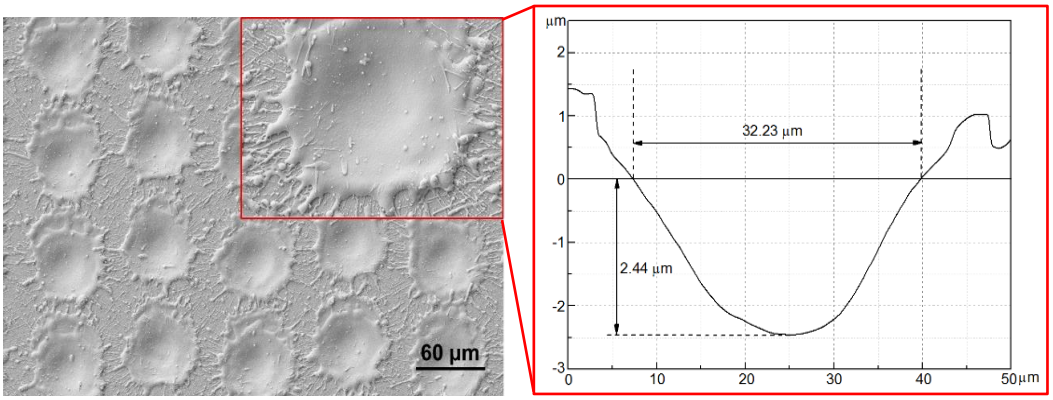

(c) (d)

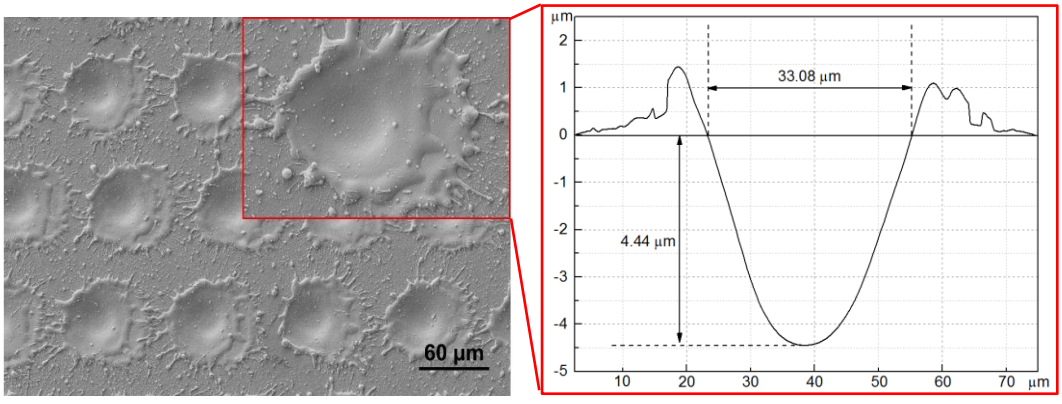

(e) (f)

Figure 5.7: SEM images of dimple structures with various laser fluence: (a) 10 J/cm^2, (c) 30 J/cm^2, (e) 50 J/cm^2 and their corresponding surface roughness (b)(d)(f).

Table 5.4: Dimensional and roughness data of dimple pattern structures created by various laser fluence values.

Laser fluence (J/cm^2)	Crater diameter (μm)	Crater depth (μm)	Roughness S_a (μm)
10	11.84 ± 0.61	0.08 ± 0.01	0.07 ± 0.02
30	32.23 ± 2.16	2.44 ± 0.41	0.17 ± 0.03
50	33.08 ± 1.99	4.44 ± 0.61	0.41 ± 0.06
As-cast	-	-	0.065 ± 0.01

Note: the errors reported correspond to one standard deviation.

5.3.2 Analysis of surface wettability

Cell attachment was reported to be particularly related to wettability and surface free energy, which are characteristics linked to surface roughness and chemical composition (Boyan et al., 1996; Chrzanowski et al., 2008; Ochsenbein et al., 2008). For instance, Ochsenbein et al. (2008) showed that cell adhesion could be enhanced via higher hydrophilicity and surface free energy. As discussed earlier, the literature also reports that laser surface texturing could be employed to modify the hydrophilicity and surface free energy of orthopaedic crystalline titanium alloys by tuning the topography of textured patterns on sample surfaces (Pfleging et al., 2015). In this section, the sessile drop method was used to assess surface wettability characteristics (i.e. contact angle, surface free energy and work of adhesion) of the Vitreloy 105 samples before and after laser surface texturing.

1. Contact angle

The measured contact angle values before and after laser surface texturing are presented in Figure 5.8. As a reference, the SCA of the polished sample wetted with the two liquids utilised (i.e. DD water and ethylene glycol) are also given (i.e. 35.17° and 19.94°, respectively). These are smaller than the Berg limit ($\theta < 65°$) (Vogler, 1998), which means that the polished as-cast sample is originally

hydrophilic. Following irradiation with the nanosecond laser, all surfaces with dimple and groove patterns remained hydrophilic, as evidenced by the measured SCA values shown in Figure 5.8, Table 5.5 and Table 5.6. The measurements also reveal that the SCA of the samples with the dimple patterns tended to be larger than that of the as-cast sample overall, while the SCA of the samples with the groove patterns were generally smaller than that of the as-cast sample for the processing conditions considered in this study. This implies that the hydrophilicity of the Vitreloy 105 surface was generally weakened when laser texturing the dimple structures but generally strengthened when laser texturing the groove patterns. This observed enhanced hydrophilicity of the groove patterned samples, compared to the as-cast, pristine, surfaces, is consistent with their significantly higher surface roughness. This result is also in-line with other reports in the literature in which laser surface texturing of metallic specimens was also studied (Bizi-Bandoki et al., 2013; Pfleging et al., 2015). However, compared to the as-cast sample, a weakened hydrophilicity is observed on the dimple patterned surfaces despite the increased surface roughness. Thus, the influence of the type of patterns on the wettability is observed in this study, as expected from literature findings reported in Chapter 2 (Bizi-Bandoki et al., 2013; Pfleging et al., 2015), it is not possible to consider the variation of the surface roughness alone to draw definitive conclusions about the evolution of the hydrophilicity of a surface.

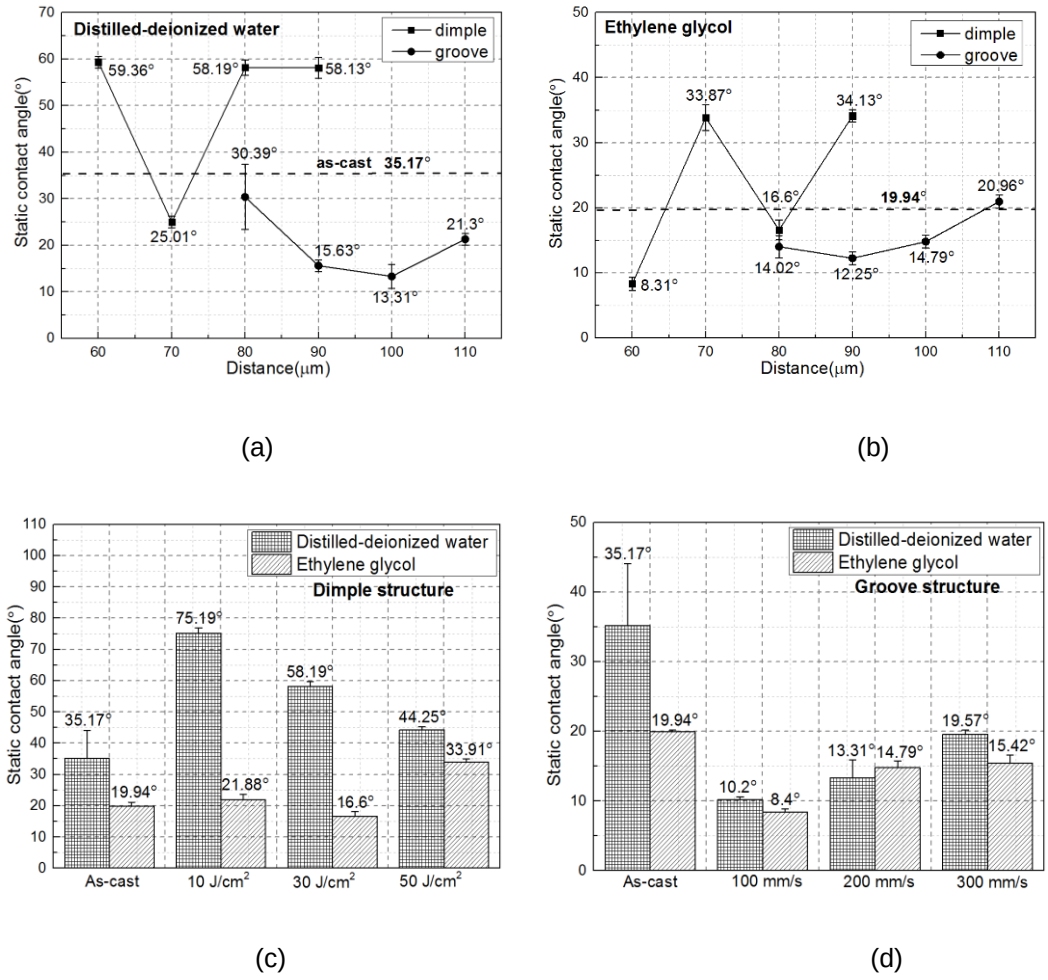

Figure 5.8: Static contact angle measurements of Vitreloy 105 metallic glass specimens before and after laser surface texturing (a) DD water on specimens treated with different values for the parameter “distance” (b) Ethylene glycol on specimens treated with different values for the parameter “distance” (c) DD water and ethylene glycol on the dimple patterns treated with different fluence values (d) DD water and ethylene glycol on the groove patterns treated with different scanning speeds.

Table 5.5: Static contact angle for the Vitreloy 105 metallic glass with dimple patterns before and after laser surface texturing.

	Distilled-deionized water				Ethylene glycol			
Scanning speed	60	70	80	90	60	70	80	90
10 J/cm^2	-	-	75.19°	-	-	-	21.88°	-
30 J/cm^2	59.36°	25.01°	58.19°	58.13	8.31°	33.87°	16.6°	34.13
50 J/cm^2	-	-	44.25°	-	-	-	33.91°	-
As-cast	35.17°				19.94°			

Table 5.6: Static contact angle for the Vitreloy 105 metallic glass with groove patterns before and after laser surface texturing.

	Distilled-deionized water				Ethylene glycol			
Scanning speed	80	90	100	110	80	90	100	110
100 mm/s	-	-	10.2°	-	-	-	8.4°	-
200 mm/s	30.39°	15.63°	13.31°	21.3°	14.02°	12.25°	14.79°	20.96°
300 mm/s	-	-	19.57°	-	-	-	15.42°	-
As-cast	35.17°				19.94°			

Figure 5.8 (a) and (b) depict the static contact angle of DD water and ethylene glycol as a function of the parameter “distance”. Unlike the evolution in surface roughness variation as a function of this parameter, there is no specific trend for the change in SCA values for the two types of surface patterns wetted by both liquids with the increase of the distance. In addition, the effect of laser fluence on the SCA of the samples with the dimple patterns is shown in Figure 5.8(c). This particular plot reveals that the contact angle decreases with the increase of the laser fluence when the surface was wetted by DD water. This indicates that the increase in laser fluence could enhance the hydrophilicity of the dimple patterns. Nevertheless, all SCA values for such patterns were found to still be higher than that of the as-cast sample surface. Figure 5.8(d) presents the SCA measurements of the metallic glass specimens textured with groove patterns as a function of the laser scanning speed. In this case, it is observed that a lower scanning speed can

enhance the surface hydrophilicity of the Vitreloy 105 specimens when assessed using both types of liquid. Representative images for the water contact angle of Vitreloy 105 metallic glass surface with different surface patterns and processed by different laser parameters are also provided in Figure 5.9.

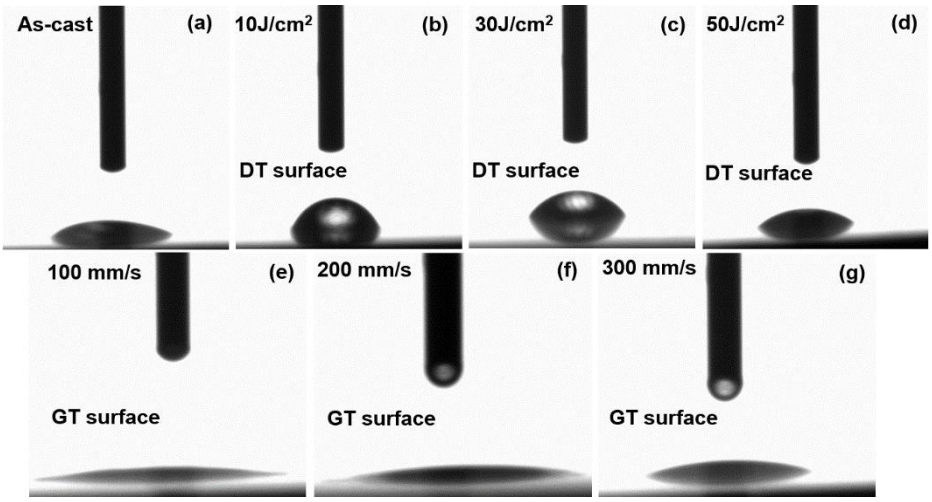

Figure 5.9: Representative images for the water contact angle of Vitreloy 105 metallic glass surface with different surface patterns and processed by different laser parameters (a) as-cast; (b) DT surface with 10 J/cm^2; (c) DT surface with 30 J/cm^2; (d) DT surface with 50 J/cm^2; (e) GT surface with 100 mm/s; (f) GT surface with 200 mm/s; (g) GT surface with 300 mm/s; Note: DT-dimple texture and GT-groove texture.

According to the Wenzel model (Wenzel, 1936), the wetting behaviour of a surface can be enhanced with increased roughness as the contact angle θ_w obeys the following equation:

$$\cos\theta_w = r\cos\theta \tag{5.2}$$

where r is the surface roughness parameter, θ is the contact angle for a flat surface and is determined by the initial surface properties of the target material.

It can be deduced from Equation 5.2 that a hydrophilic surface becomes more hydrophilic with the increase of roughness while an initially hydrophobic surface evolves as more hydrophobic with a higher roughness. The topography analysis

reported earlier in section 5.3.1 showed that the surface roughness of all the groove textured samples was larger than that of the dimpled textured and as-cast samples. Besides, since the as-cast polished Vitreloy 105 surface was originally hydrophilic, the Wenzel model can be used to explain how the textured surface becomes more hydrophilic when fabricating the groove patterns with a lower scanning speed. However, for the dimple textures, the surface roughness of all the samples was also higher than that of the as-cast. However, the SCA values measured became larger. In this case, the Wenzel model (Wenzel, 1936) or the Cassie-Baxter model (Cassie and Baxter, 1944) cannot explain this observation. As reported in Chapter 2, surface wettability not only depends on the surface topography but also on the surface chemistry properties. Thus, the influence of the surface chemical composition change induced by laser processing may be a likely reason to explain why the dimple structures resulted in a weakened hydrophilicity despite the increased roughness from that of the as-cast samples. Therefore, the underlying mechanism of wettability modification for the laser textured Zr-based amorphous alloy will be discussed from a surface chemistry perspective in a later section (i.e. section 5.3.3).

Finally, it can also be said that the contact angle measurements results presented here are consistent with those of Yang et al. (2017), Pfleging et al. (2015) and Kumari et al. (2015) who also investigated the effect of laser texturing on the surface wettability of metallic substrates. In particular, these authors observed that groove textured patterns could significantly enhance the hydrophilicity of the processed surface and also, that such groove patterned surfaces were more beneficial for cell viability and attachment when compared with dimple-patterned surfaces. From the results presented here, it is also clear that the generation of a groove textured surface is a suitable approach to enhance the hydrophilicity of the Vitreloy 105 metallic glasses.

2. Surface free energy

In this section, the surface free energy of the Vitreloy 105 samples is explored as a function of the textured pattern. It has to be mentioned that the influence of the parameter “distance” on the surface free energy and work of adhesion is not presented due to the fact that no specific dependence had been observed earlier between this parameter and the contact angle (Figure 5.8(a) and Figure 5.8(b)). Figure 5.10 and Table 5.7 show the variation of the total, dispersive and polar surface free energy of as-cast and laser textured surfaces. From this figure, it should be noted that the total surface free energy of the laser textured surfaces varies significantly from 46.07 to 125.74 mN/m as compared to that of the as-cast specimens (81.04 mN/m). A more detailed observation reveals that the total surface energy of the textures with dimples is always lower than that of the as-cast specimen, although it is noted that this is marginally true in the case of the smallest fluence value considered. For the surfaces with the groove patterns, the total surface energy is always clearly higher than that of the as-cast specimen. Furthermore, the polar component of the surface energy is consistently the much higher contributor for the groove patterns while it is the dispersive component of the surface energy which the more significant contributor for the dimple patterns. Unlike the monotonous relationship of the SCA with the laser fluence or scanning speed, there is no linear trend between surface free energy and these two parameters in the processing window considered here.

The surface free energy of materials is influenced by several surface characteristics including its chemical composition, charge and topography (Andrade et al., 1985). At the same time, high surface energy and enhanced wettability can promote the interaction between the surface of an implant and the physiological environment, cell spreading and cell attachment (Baier et al., 1984; Schrader, 1981; Schwarz et al., 2009). In fact, Hallab et al. (2001) also reported that the surface free energy plays a more important role in inducing cell attachment

and proliferation than surface roughness. The polar component of surface energy has a significant effect on wettability because polar molecules can interact with the dipole force and hydrogen bonds, which is beneficial for the enhancement of wettability (Hallab et al., 2001; Sarapirom et al., 2013). In combination with the contact angle measurements reported in the previous section, it can be concluded that the high polar surface energy of surfaces with groove patterns contributes to their enhanced hydrophilicity. Hallab et al. (2001) also indicated that the cellular adhesion strength has a strong positive relationship with the total surface energy and the polar component. On the contrary, a lower level of correlation was found between the dispersive component and the adhesion strength. In summary, it can be concluded from the presented results that groove patterns provide a higher surface free energy. In turns, this could be beneficial for enhancing cell attachment on laser textured Vitreloy 105 surfaces.

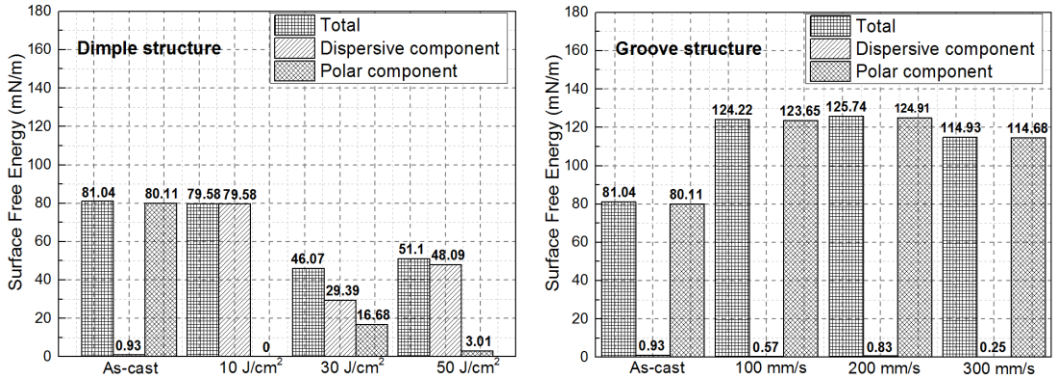

(a) (b)

Figure 5.10: The variation of the total, dispersive and polar surface free energy of as-cast and laser textured surface with groove and dimple patterns.

Table 5.7: Surface free energy and its components of as-cast and laser textured surface with groove and dimple patterns.

Surface free energy (mN/m)	Dimple pattern			Groove pattern			As-cast
	10 J/cm^2	30 J/cm^2	50 J/cm^2	100 mm/s	200 mm/s	300 mm/s	
Total	79.58	46.07	51.1	124.22	125.74	114.93	81.04
Dispersive component	79.58	29.39	48.09	0.57	0.83	0.25	0.93
Polar component	0	16.68	3.01	123.65	124.91	114.68	80.11

3. Work of adhesion

The evaluation of the work of adhesion (W_a) for as-cast and laser textured Vitreloy 105 specimens wetted by two liquids (distilled-deionized water and ethylene glycol) is shown in Figure 5.11 and Table 5.8. The work of adhesion for the as-cast specimen was 136.84 and 88.41 mN/m when wetted by DD water and ethylene glycol, respectively. It should be noted that the work of adhesion for the samples textured with groove patterns is always higher than that of the as-cast specimens for both liquids. In contrast, the work of adhesion for the surfaces textured with dimple patterns is lower than the as-cast ones, for the DD water while it is either equal or only slightly higher for the ethylene glycol. These results are generally consistent with the surface free energy and water contact angle measurements. However, no particular trend can be identified between W_a and the scanning speed for the groove patterns or between W_a and the laser fluence for the dimpled surfaces.

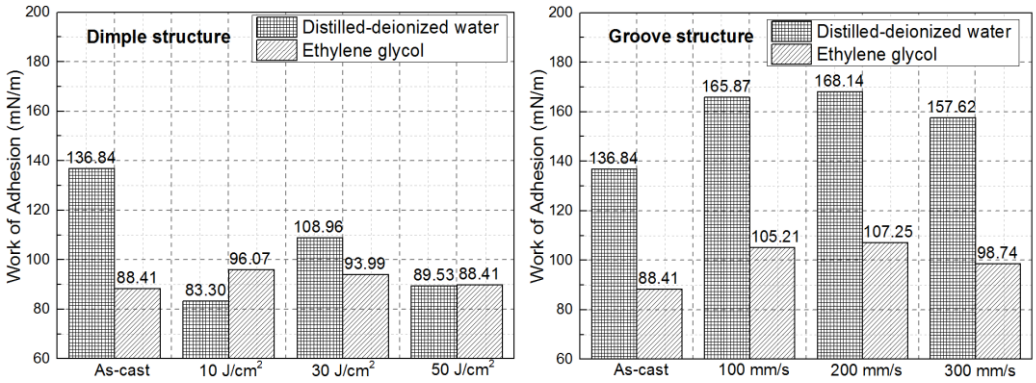

(a) (b)

Figure 5.11: Work of adhesion for as-cast and laser textured surface with dimple and groove patterns.

Table 5.8: Work of adhesion for distilled-deionized water and ethylene glycol on the as-cast and laser textured specimens.

Work of adhesion (mN/m)	Dimple pattern			Groove pattern			As-cast
	10 J/cm^2	30 J/cm^2	50 J/cm^2	100 mm/s	200 mm/s	300 mm/s	
DD water	83.30	108.96	89.53	165.87	168.14	157.62	136.84
ethylene glycol	96.07	93.99	89.81	105.21	107.25	98.74	88.41

5.3.3 Surface chemistry

Laser surface texturing can introduce changes in the surface chemical composition through the partial vaporisation of material, diffusion of specific alloying elements or reaction with the environment, principally oxidation (Fasasi et al., 2009). In order to explore the effect of laser surface texturing on the variation of the surface chemical composition of the metallic glass samples, and to further correlate the surface chemistry with the wettability results, the surfaces of the laser textured samples were analysed using energy dispersive X-ray detector (EDX) mapping and X-ray photoelectron spectroscopy (XPS). In this section, the dimple-textured

and groove-textured BMG samples considered for the surface chemistry analysis were treated with the same laser fluence of 30 J/cm^2 and also the same parameter “distance” of 90 µm for the dimple texture and groove texture. In addition, the scanning speed for the groove-textured sample was set at 200 mm/s. The EDX data obtained to assess the distribution of Zr, Cu, Ni, Al, O, and C for the as-cast, dimple, and groove textured samples are shown in Figure 5.12. Given that the content of Ti is the lowest among all the elements contained in the composition of Vitreloy 105 and its presence was difficult to detect as a result, data for Ti are not presented here. It can be seen from this figure that the Zr, Cu, Ni, Al, O, and C elements are uniformly distributed on the as-cast specimen. For the dimple textured sample, the elements Ni, Al, C, and O are uniformly distributed on the irradiated surfaces, while some small areas corresponding to the rims of the single craters may suggest a reduction of the Zr and Cu elements distribution. However, this may be an artefact resulting from the topography of the laser-induced protrusions. This observation is also applicable to the elemental distribution of the groove patterned samples as the location of the black areas shows a good match with the protrusions of the grooves. Given that the EDX mapping is mainly a qualitative analysis technique and could not provide specific conclusions about the evolution of the surface chemistry following laser processing, a more precise chemical element analysis, XPS, was employed to investigate the chemical changes of the laser surface textured Vitreloy 105 specimens in a more quantitative manner.

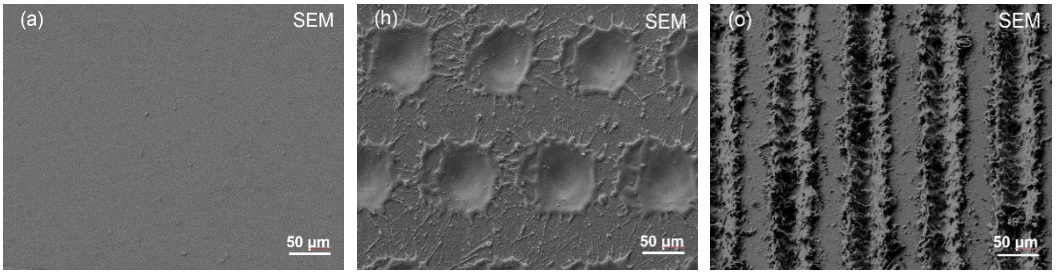

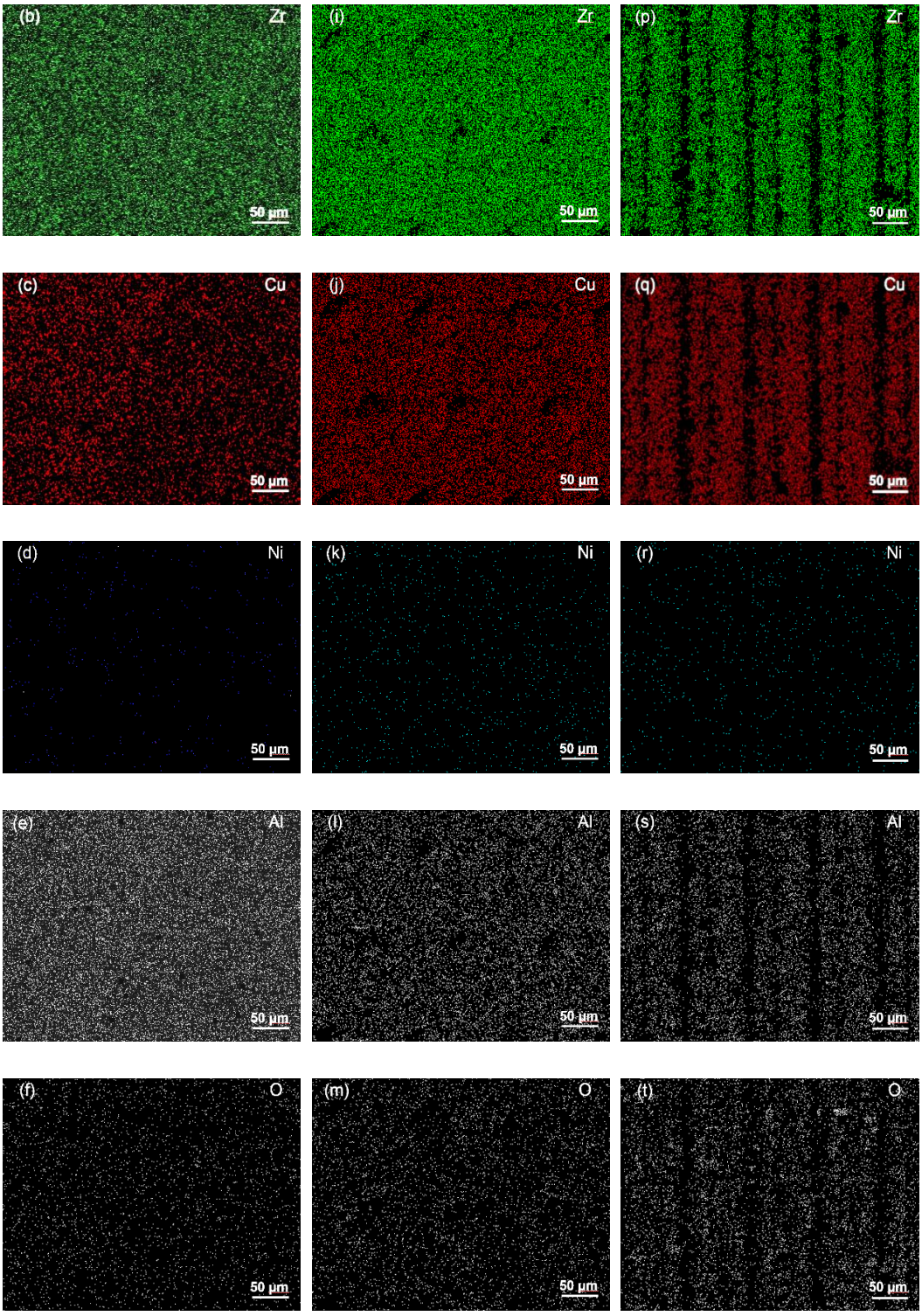
(b) Zr
(i) Zr
(p) Zr
(c) Cu
(j) Cu
(q) Cu
(d) Ni
(k) Ni
(r) Ni
(e) Al
(l) Al
(s) Al
(f) O
(m) O
(t) O
50 µm

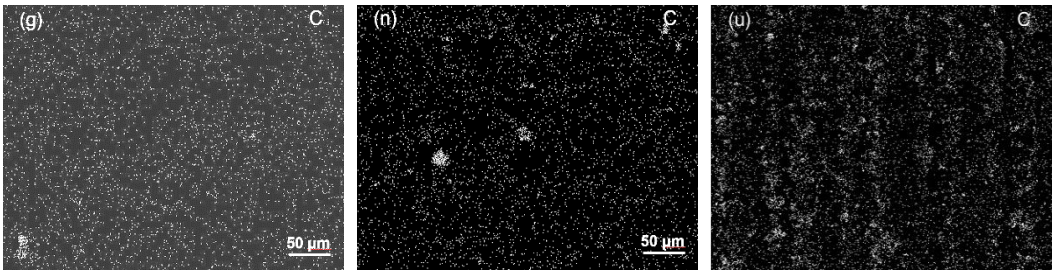

Figure 5.12: SEM/EDX element mappings of as-cast (a-g), dimple textured (h-n) and groove textured (o-u) laser irradiated surfaces. (a), (h) and (o) are SEM images depicting the corresponding analysed regions; (b-u) are the EDX maps showing the qualitative elemental distributions of Zr, Cu, Ni, Al, O, and C.

The XPS full spectra and the detailed atomic elemental composition of all the samples (as-cast, dimple-textured and groove-textured specimens) are shown in Figure 5.13. For the non-processed surfaces, the main elements detected were carbon (58.89 %) and oxygen (28.58 %), which is ascribed to the contamination and oxidation of the surface by water molecules and other contaminants from the atmosphere. In addition to the C 1*s* and O 1*s* peaks, the as-cast sample shows small peaks on the Al 2*p* and Zr 3*d* region. The non-processed surface also contained negligible amounts of Ti, Cu, and Ni elements.

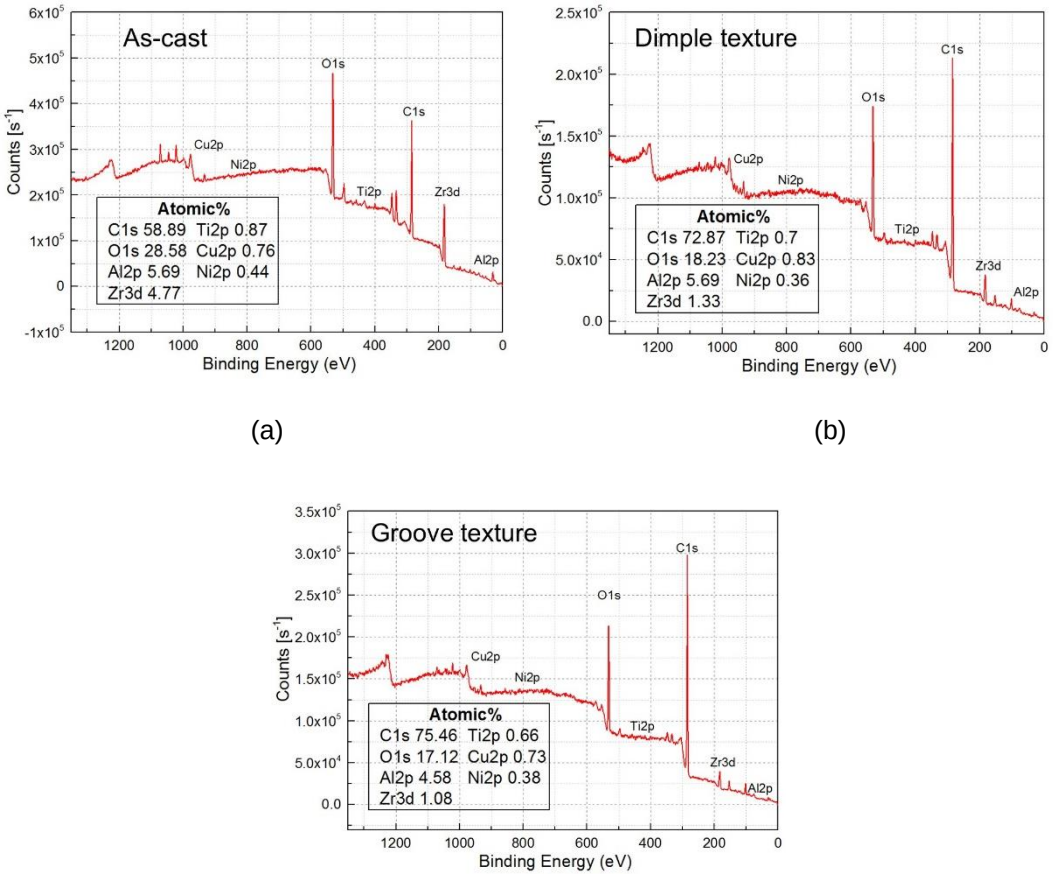

Figure 5.13: XPS full spectra of Vitreloy 105 metallic glass before and after laser surface texturing: (a) as-cast; (b) dimple-textured specimen; (c) groove-textured specimen.

The detailed atomic elemental composition of the Vitreloy 105 samples without and with textured patterns is shown in the inset of the corresponding XPS spectra in Figure 5.13. These data indicate a decrease in the percentage of zirconium concentration on the Vitreloy 105 surfaces after laser texturing compared to the as-cast one, which may be attributed to material vaporisation during laser irradiation. In comparison, the contents of Al remained relatively stable. Furthermore, while the as-cast specimen exhibited a carbon content of 58.89 %, this was increased to 72.87 % and 75.46 % after laser surface texturing for the dimple and groove-textured surfaces, respectively, which implies that more

hydrocarbons were introduced on the sample surface as a result of laser processing. In contrast, the oxygen content decreased from 28.58% for as-cast to 18.23 % and 17.12 % for the dimple and groove-textured surfaces, respectively, suggesting the removal of metal oxide from the surface. Additionally, due to oxidation and contamination, all samples exhibited a rather low concentration of Ti, Cu, and Ni on their surfaces. It was reported by Bizi-Bandoki et al. (2013) that new functional chemical groups, such as non-polar carbon groups (–CH3 and graphitic carbon), can be introduced by laser surface texturing on the sample surface. These two carbon groups could make the sample surface more hydrophobic. This indicates that the laser-induced change in the carbon content and type may be an important contributor to the evolution of the wettability following laser processing. Kietzig et al. (2009) also proposed a chemical evolution of the non-polar carbon for the explanation of weakened hydrophilicity following the femtosecond laser irradiation of different metallic alloys. For this reason, a higher resolution XPS spectra of carbon was also performed on the laser textured Vitreloy 105 surfaces.

These high-resolution XPS spectra for the C1s regions are shown in Figure 5.14. It can be seen from Figure 5.14 (a) that the as-cast sample shows three different carbon bonding environments: carbon-carbon (C-C) bonds or hydrocarbons species (C-H) at 284.8 eV, carbonyl bonds (C=O) at 288.6 eV and carboxyl species (O=C-O) at 292.8 eV. After laser texturing, the C-C/C-H peak was reduced, particularly in the case of the dimple pattern. Huerta-Murillo et al. (2019) attributed this to the removal of surface contaminants during the laser ablation process. Additionally, the intensity of the C=O component was also reduced, again more significantly for the dimple pattern, while the intensity of the O=C-O component was reduced to a near-negligible level for both types of patterns. It is reported in the literature that the carbonyl bonds (C=O) and O=C-O species are all polar molecules, which can enhance the hydrophilicity of a surface due to the polarity of

the water molecules, whereas C-C/C-H bonds are non-polar and can lead to a hydrophobic effect on the surface (Huerta-Murillo et al., 2019).

Based on the reported data, it can reasonably be inferred that the wettability of the three types of surface considered in this study, i.e. as-cast, dimple-textured and groove-textured surface, results from the combined effects of laser irradiation on the achieved surface roughness enhancement and chemical modification. More specifically, for the as-cast samples, given that the surface roughness was only 0.065 µm, its contribution to the initial hydrophilicity may be neglected. In this case, the hydrophilic property of the as-cast sample should mainly result from the presence of polar carbonyl bonds (C=O) and carboxyl species (O=C-O). For the dimple-textured sample, the surface roughness was measured to be 0.21 µm. Considering that this is higher than that of the as-cast specimen, based on the Wenzel model, it could be expected that the hydrophilicity may be enhanced. However, given that the opposite was observed, i.e. a weakened hydrophilicity for the dimple patterns, it can be said that the influence of the surface roughness modification should play a relatively less important role as a contributor to the hydrophilicity compared to the influence of surface chemistry variations. In fact, after laser dimple texturing, the intensity of the hydrophilic carbonyl bonds (C=O) and carboxyl species (O=C-O) were significantly reduced as observed in Figure 5.14. The intensity of the hydrophobic C-C/C-H bonds was also reduced. For this reason, it is proposed that the likelihood explanation for the weakened hydrophilicity of the dimple-textured samples is the significantly reduced content of the hydrophilic (C=O) and (O=C-O) bonds. Finally, in the case of the groove textured samples, the surface roughness was measured to be 3.24 µm. This is 50 times higher than that of the as-cast samples. Thus, although the hydrophilic carbonyl bonds (C=O) and carboxyl species (O=C-O) were reduced after groove texturing, in this case, it is the much higher surface roughness that should be the dominant factor in the hydrophilicity enhancement of the groove-textured samples.

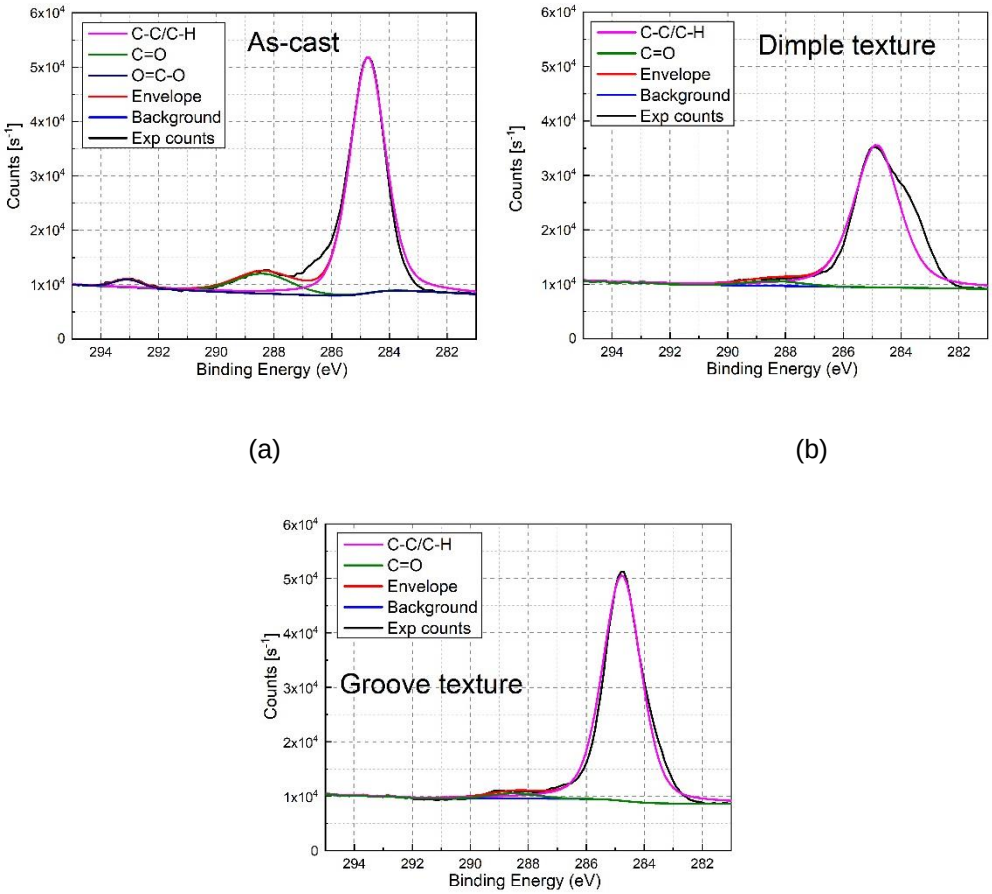

Figure 5.14: High-resolution spectra from the C1s regions on the Vitreloy 105 metallic glass with and without laser surface texturing: (a) as-cast; (b) dimple-textured surface; (c) groove-textured surface.

5.4 Conclusions

Nanosecond-pulsed laser surface texturing was employed in this chapter to fabricate two types of surface patterns, i.e. dimples and grooves, on Vitreloy 105. These surface patterns were fabricated with the aim to investigate whether they could improve the surface wettability of the as-cast Vitreloy 105 material and hence, enhance the potential of this particular BMG alloy to be considered for biomedical applications. The surface topography and roughness of samples laser irradiated

with different process parameters when machining the considered patterns were studied and compared. The static contact angle was measured, and the surface free energy was assessed for all samples. Comparisons of surface chemical composition before and after laser texturing were also made via EDX mapping and XPS analysis in an attempt to explain how such laser-induced variations could contribute to the wettability modification mechanism.

The obtained results confirm the existing literature that surface wettability can be modified intentionally by laser texturing depending of the generated surface patterns and selected process parameters. In line with former reports where laser texturing was applied to other type of metallic materials, it was found that the groove patterns induced higher roughness on the sample surface compared to the dimple patterns. In the processing window considered in this chapter, the effect of distance between two consecutive grooves or craters on the surface roughness of groove patterned or dimple patterned surface could be neglected. However, the scanning speed had an important influence on the surface roughness of the groove textured sample, while the laser fluence also affected the dimple textured surface roughness significantly. An important conclusion from the result is that the surface hydrophilicity of the as-cast Vitreloy 105 surface could be enhanced by laser texturing of groove patterns. Based on the outcome of the surface topography and chemistry analyses, this increased hydrophilicity could be attributed to the dominant role that a much higher roughness plays for such patterns. In contrast, the hydrophilicity of the as-cast surface was generally deteriorated with the laser texturing of dimple patterns. This result was attributed to the more dominant role that surface chemistry modification plays in this case and in particular, to the reduction of the hydrophilic carbonyl bonds (C=O) and carboxyl species (O=C-O). An important outcome of the work presented is that it indicates the possible potential of Vitreloy 105 to be employed in applications for orthopaedic implants when used in combination with laser surface texturing to generate groove patterns

on the implant surface. Complementary investigations on cell viability and attachment by in vitro cell culture on such patterns are presented in the following chapter.

Chapter 6 Laser texturing of the $Zr_{52.8}Cu_{17.6}Ni_{14.8}Al_{9.9}Ti_{4.9}$ bulk metallic glass for *in-vitro* bio-compatibility modification

6.1 Introduction

This chapter aims to investigate the feasibility of using nanosecond laser surface texturing as a method to modify the *in-vitro* bio-compatibility of Vitreloy 105. The available fibre laser system was employed to fabricate dimpled and grooved textures on the surface of the Zr-based BMG pulse duration of 220 ns. The resulting surface topography, chemical composition and wettability were evaluated for these different patterns via non-contact three-dimensional confocal microscopy, scanning electron microscopy, X-ray photoelectron spectrometry and contact angle measurements. The cellular response of osteoblast-like MG63 cells on as-cast and laser textured surfaces was investigated via cell viability, cell attachment and cell morphology assays. The underlying mechanism associated with laser surface texturing which affected the *in-vitro* bio-compatibility of Vitreloy 105 was discussed based on the changes to surface chemistry, wettability and surface roughness.

6.2 Experimental procedures

6.2.1 Sample preparation

The sample preparation method implemented for the bio-compatibility tests was slightly different from that employed in other chapters. Thus, specific details are described here. In particular, the cylindrical rods (3 mm in diameter and 3 mm in length) for cellular behaviour studies were manually grinded transverse to the long axis using coarse abrasive paper (180 grit) and then polished with 1200 and 2000 grit SiC papers followed by a final step using a 1 μm diamond gel suspension until a mirror-like appearance. All the samples were also mounted in conducted resin to carry out the polishing process. Subsequently, all the samples were also cleaned with the ultrasonic bath using the acetone and distilled water for 15 min each. Before each biochemical test, the samples were pre-immersed in the PBS solution for 2 hours and sterilised in an autoclave for approximately 15 minutes at 121 ˚C and 1.4 bar.

6.2.2 Nanosecond laser processing: specific experimental plan

In line with the work reported in the previous chapter, two types of surface textures, dimples and grooves, were machined on the surface of the metallic glass specimens using the nanosecond fibre laser using the pulse duration of 220 ns. The pulse repetition frequency was set to be 20 kHz. The laser source was stationary. The machined samples were fixed on the high-resolution 3-axis motion platform of the laser system to achieve the patterning. All surface patterns were machined under the same laser fluence of 30 J/cm^2 and also with the same “distance” of 90 μm, as defined in the previous chapter. The scanning speed for the groove textured samples was fixed at 200 mm/s, which results in a pulse

overlap of 68.8 %. The laser parameters used for laser texturing are summarised in Table 6.1.

Table 6.1: Laser parameters for the fabrication of dimple and groove patterns on the surface of Zr-based BMG samples.

Wavelength (nm)	Spot diameter (μm)	Pulse duration (ns)	Frequency (kHz)	Laser fluence (J/cm^2)	Track distance (μm)	Scanning speed (mm/s)	Surface patterns
1064	32	220	20	30	90	-	Dimples
						200	Grooves

6.2.3 Cellular behaviour study

Osteoblast-like MG63 cells were employed to evaluate the bio-compatibility of the $Zr_{52.8}Cu_{17.6}Ni_{14.8}Al_{9.9}Ti_{4.9}$ BMG surfaces processed with different surface conditions. The cell viability test, cell attachment and morphology observation were conducted according to specific instruments and test formats. All the details about the cell culture, cell viability test, cell attachment and morphology observation were described in Section 3.6.

6.3 Results

It has to declare that the study in this chapter is a further investigation about the bio-compatibility of the laser-textured Vitreloy 105 samples based on the wettability investigations shown in Chapter 5. Only one set of laser parameter was chosen for each type of textured sample (as shown in Table 6.1), so the surface topography and wettability results as well as surface chemistry results presented in this chapter were the same as those in chapter 5. These results presented here were for the purpose of briefly reminding.

6.3.1 Surface characterisation

Figure 6.1 shows the surface topography of the BMG samples with different surface texturing (i.e. as-cast: AC, dimple-textured: DT and groove-textured: GT) observed with the 3D optical microscope and field-emission scanning electron microscope. The DT surface was generated by creating an array of single craters, with each crater corresponding to a single pulse irradiation event. On this surface, rims and vapour particles were distributed around the craters as a result of the laser-material interaction phenomena, as discussed in Chapter 4. Grooves and ridges could also be observed clearly on the GT samples, while almost no surface features were visible on the as-cast (i.e. AC) samples.

The measured dimensions (i.e. depth, diameter/width) and surface roughness values of these three types of surfaces are listed in Table 6.2 using the arithmetical average height of the specific surface area, S_a. For the AC samples, S_a was assessed to be 0.065 µm, while S_a for the DT and GT samples increased to 0.21 µm and 3.24 µm, respectively. The average depths of a single crater for the DT specimen and of a groove for the GT surface were 2.44 µm and 10.2 µm, respectively. In addition, their corresponding width(s)/diameter(s) were 32.23 µm and 28.6 µm, respectively. It was reported in the literature (Huang et al., 2011) that the increased surface roughness is beneficial for the cell attachment and cell orientation on the titanium alloys. The effects of the two types of surface textures considered here on the cell behaviour for the Zr-based metallic glass from the perspective of surface roughness variation will be discussed in section 6.4.2.

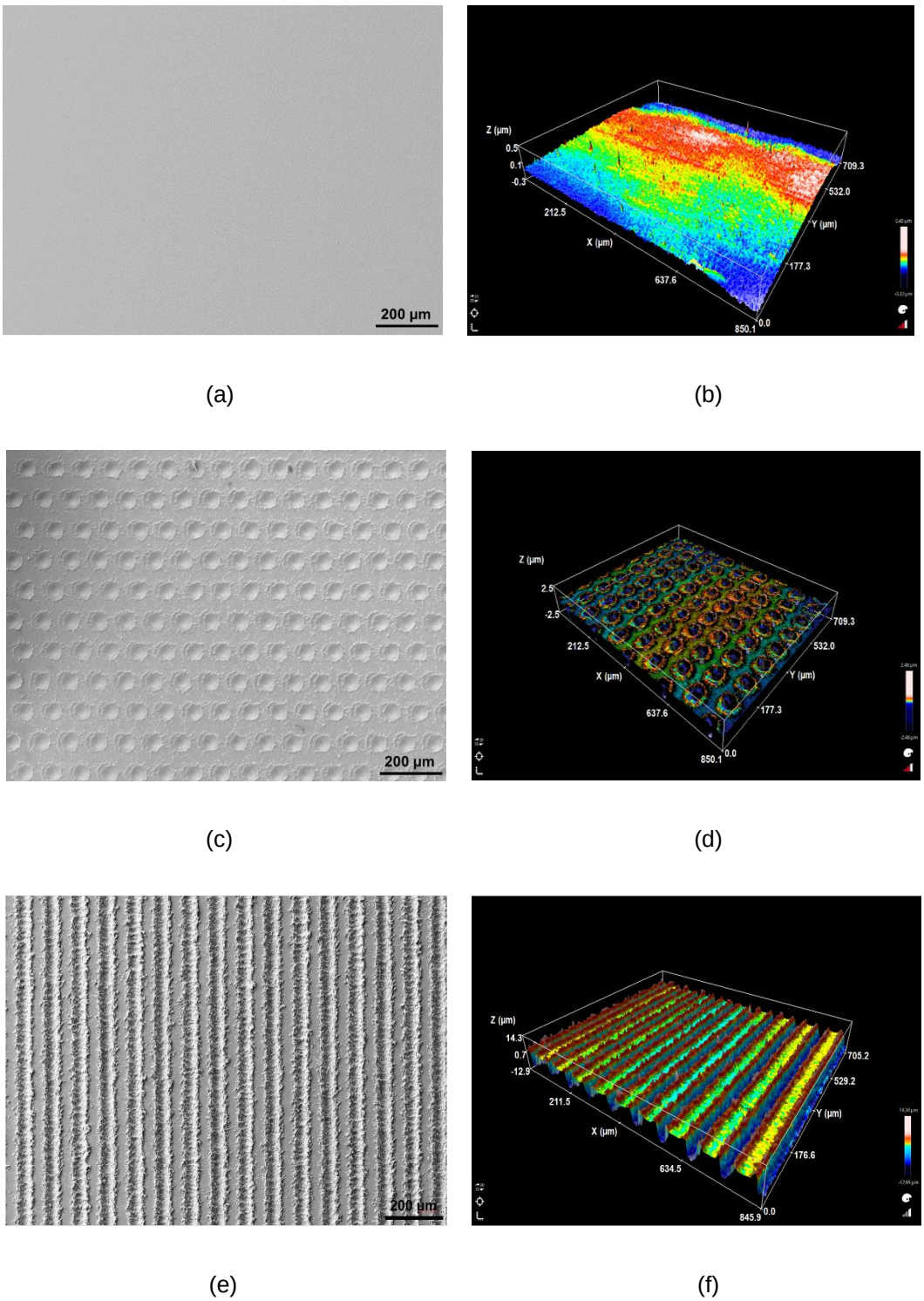

(a) (b)

(c) (d)

(e) (f)

Figure 6.1: SEM images for $Zr_{52.8}Cu_{17.6}Ni_{14.8}Al_{9.9}Ti_{4.9}$ BMG samples (a, c, e) and their corresponding surface topography (b, d, e). (a) (b) for as-cast, (c)(d) for dimple textured and (e) (f) for groove textured sample.

Table 6.2: Surface roughness for different samples.

Samples	Roughness S_a (µm)	Depth (µm)	Diameter/Width (µm)
Dimple textured (DT)	0.21	2.44	32.23
Groove textured (GT)	3.54	10.2	28.6
As-cast (AC)	0.065	-	-

Figure 6.2 shows the high-resolution XPS spectra of the metallic glass surfaces, in the case of the AC, DT, and GT surfaces for Zr 3*d*, Al 2*p*, Ti 2*p* and O 1*s* elements. Zirconium oxides (ZrO_2 and ZrO_x) and metallic Zr (i.e. pure Zr) were detected on the AC surface. In contrast, no trace of metallic Zr was observed on the surface of the samples after laser treatment, indicating that the zirconium on the surface was oxidized during the laser texturing process. In the case of Ti 2*p*, all the samples show a similar behaviour where the spectra reveal peaks at 458.5 eV and 464.2 eV corresponding to titanium oxide (TiO_2) doublets, Ti $2p_{1/2}$ and Ti $2p_{3/2}$, respectively. Moreover, for the Al 2*p* region, the XPS spectrum for the samples with and without laser texturing all show peaks at 72.6 eV, 74.6 eV and 76.8 eV corresponding to the metallic Al, Al_2O_3 and AlO(OH), respectively. After laser texturing the groove pattern, the data suggests a reduced content of the aluminium element, particularly Al_2O_3. The formation of titanium oxides, zirconium oxides and aluminium oxides can also be verified by examining the O 1*s* spectra shown in Figure 6.2 (j) to (l).

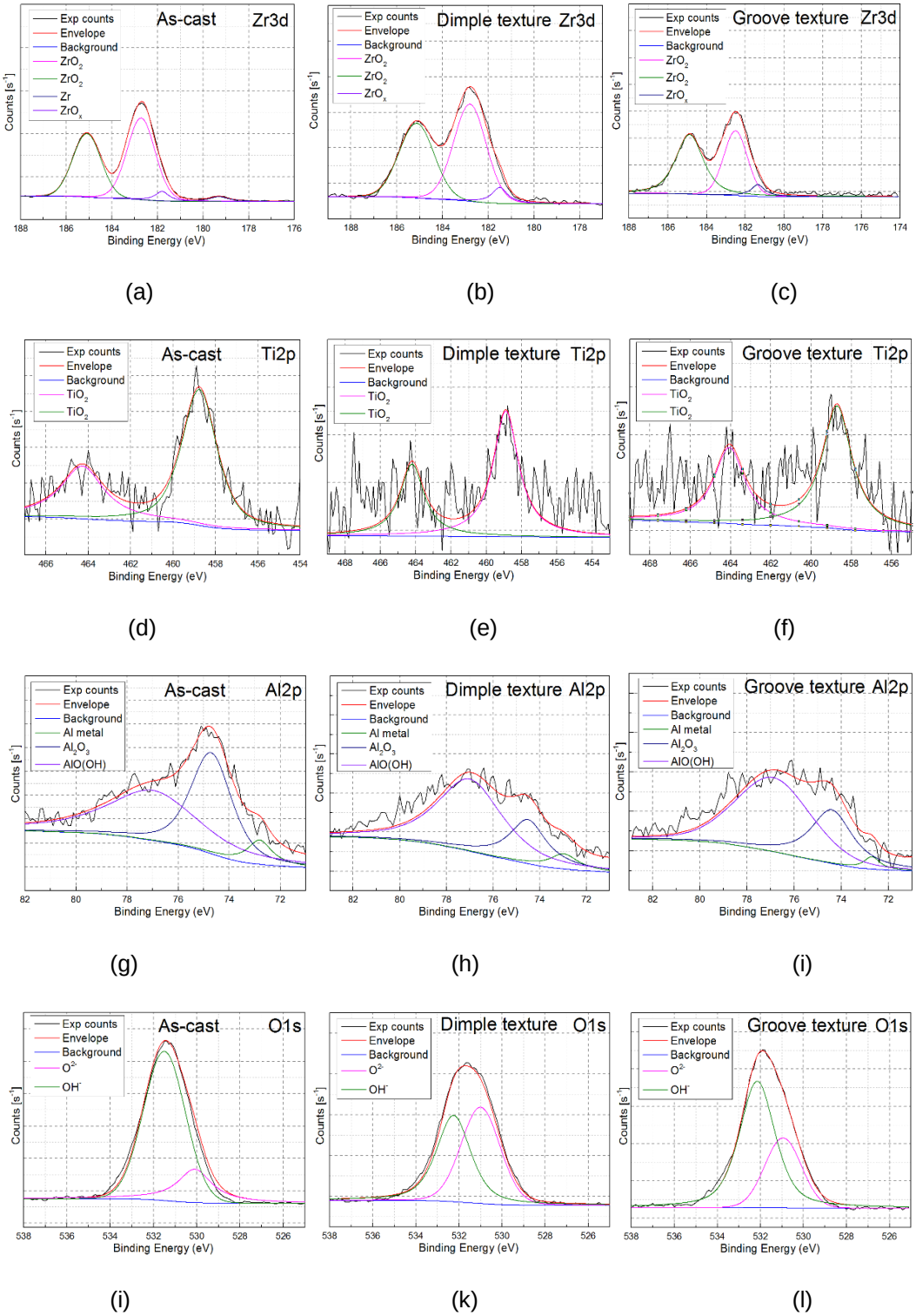

Figure 6.2: High-resolution XPS spectra for the as-cast, dimple textured and groove textured samples: narrow scans of (a) to (c) for Zr 3*d*, (d) to (f) Ti 2*p*, (g) to (i) Al 2*p* and (j) to (l) O 1*s*.

6.3.2 Wettability and SFE

Surface wettability in terms of static contact angle (SCA) was characterized by the sessile drop technique. The SCA value of the AC, GT and DT are presented in Figure 6.3 and Table 6.3. As discussed in Chapter 5, the groove texture could enhance the hydrophilicity of the Vitreloy 105 metallic glass surface, while the dimple texture can weaken it. In the open literature (Costa and Hutchings, 2007; Junker et al., 2009), it has been reported that a hydrophilic surface is beneficial for cell attachment and proliferation.

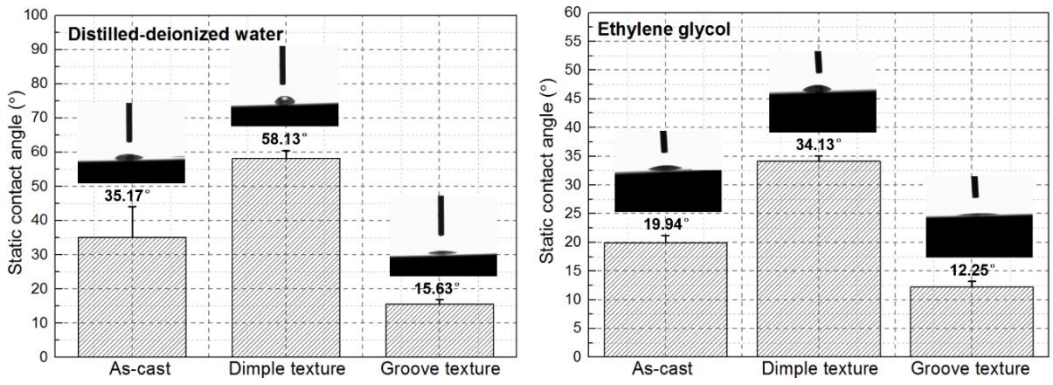

(a) (b)

Figure 6.3: Static contact angle of the Zr-based metallic glass samples in the case of as-cast, dimple texture and groove texture wetted by distilled-deionized water (a) and ethylene glycol (b). Optical images of the droplets on the different sample surface are shown in the insets.

Table 6.3: Static contact angle and surface free energy of as-cast and laser textured surface with groove and dimple texture.

Samples	Contact angle (°)		Surface free energy (mN/m)		
	DD water	Ethylene glycol	Dispersive (γ^d)	Polar (γ^p)	Total (γ^T)
As-cast	35.17	19.94	0.93	80.11	81.04
Dimple texture	58.13	34.13	12.78	29.83	42.65
Groove texture	15.63°	12.25°	0.38	118.92	119.3

The surface free energy (SFE) was calculated from the Owens–Wendt model based on the SCA values measured using two liquids (i.e. distilled-deionized water and ethylene glycol). The SFE values for each specimen along with the polar and dispersive components are shown in Figure 6.4 and Table 6.3. From the Figure 6.4, it should be noted that the surface free energy of the Zr-based metallic glass surfaces shows a significant difference. Indeed, it varies from 42.65 mN/m for DT sample to 119.3 mN/m for the GT specimen in comparison with 81.04 mN/m for the AC sample. Furthermore, the polar component of the SFE is significantly higher in the cast of GT surface (118.92 mN/m) compared to the AC (80.11 mN/m) and DT (29.83 mN/m) surfaces. In contrast, the dispersive component of the SFE for the DT sample (12.78 mN/m) is much higher than the AC (0.93 mN/m) and the GT (0.38 mN/m) samples. The SFE of a material is reported to be determined by several characteristics, including surface chemical composition, surface topography and surface charge. The relationship between the SFE and cellular behaviour of the Zr-based BMGs for different types of surface patterns will be discussed in the next sections.

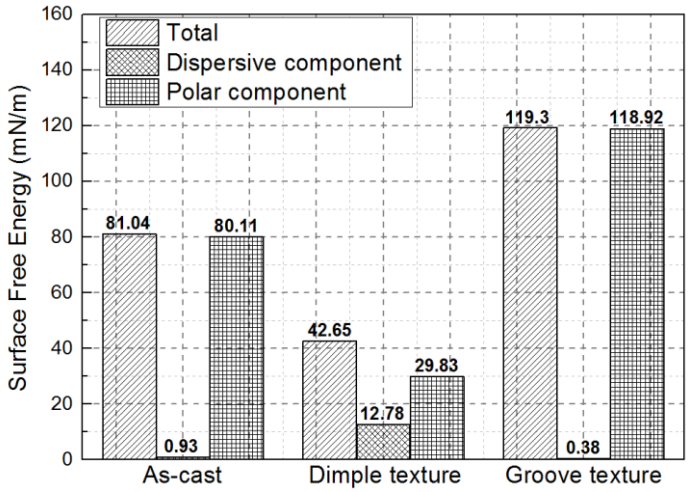

Figure 6.4: Surface free energy and its dispersive and polar components for the $Zr_{52.8}Cu_{17.6}Ni_{14.8}Al_{9.9}Ti_{4.9}$ BMG in the case of as-cast, dimple texture and groove texture.

6.3.3 Cell viability

Figure 6.5 shows the cell viability characterized by the optical density (OD) of MG63 osteoblast-like cells on the AC, DT and GT samples as measured by the CCK-8 assay. From this figure, for the MG63 cells after a 24 h incubation, it can be seen that the measured OD values for all these three samples were above the background OD values of the negative control with no cells. Moreover, the optical density values of the as-cast and laser textured samples were comparable to or larger than the positive control samples (cells on tissue culture plastic). This means that the cells were able to survive on all the Zr-based BMG surfaces and thus, that the Vitreloy 105 BMG has no cytotoxic effect. A detailed comparison of cell viability between the as-cast and the laser textured samples shows that the OD values of the GT surface was the highest (0.66 ± 0.04), and that of the AC sample surface (0.53 ± 0.03) was slightly higher than that of the DT sample surface (0.52 ± 0.03). It was reported by Huang et al. (2012a) that a higher optical density (OD) value represents a higher cell viability. Therefore, it can be concluded that the groove-textured surface is beneficial for greater cell viability. The cell viability results are

in line with the wettability results reported earlier and also with findings made by Mukherjee et al. (2013) in the case of MG63 cells on the micro-groove patterned Ti-6Al-4V alloys surface.

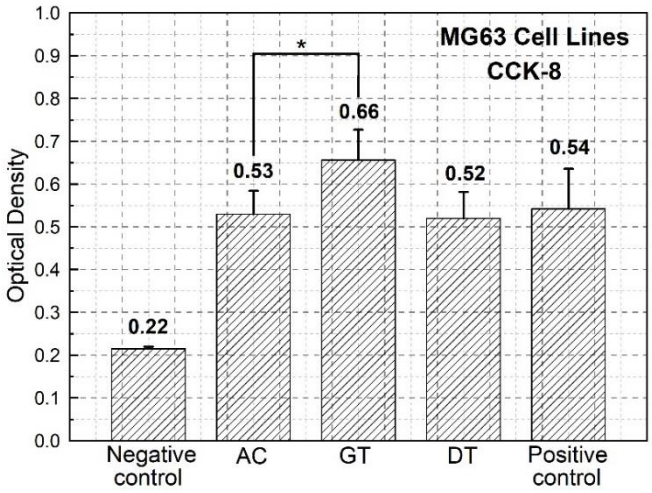

Figure 6.5: Cell viability measured with CCK-8 assay of cells cultured on $Zr_{52.8}Cu_{17.6}Ni_{14.8}Al_{9.9}Ti_{4.9}$ BMG in the case of as-cast, dimple texture and groove texture. The t-test was conducted on the certain pairs of presented data; the inclusion of the symbol * in this figure indicates that the means of these sets of data were found to be significantly different from each other ($p<0.05$).

6.3.4 Cell attachment and morphology

Figure 6.6 shows the representative fluorescent microscopic graphs of the cell morphologies for the MG63 cells cultured for 24 h on the surface of AC, DT and GT Zr-based BMG samples. From these figures, the dimple patterns and groove patterns can be seen clearly. Figure 6.6 (a) and (b) show the appearance of cells attached to the AC Zr-based BMG surface, stained by DAPI and phalloidin, respectively. It can be seen that a number of labelled cells were attached to and spread out on the AC surface. In contrast, almost no cells can be found on the dimple textured sample surface. In comparison with the AC samples, more cells

can be found on the GT sample surface, which agrees with the cell viability results discussed in section 6.3.3. These observations mean that the laser-induced groove texture can promote the cell attachment while the dimple texture can inhibit it. In addition, it should be noted that the SFE results presented earlier show a good correlation with the cell attachment results. Cell morphologies of the MG63 cells cultured on the AC and GT BMGs stained by both DAPI and phalloidin were shown in Figure 6.7. From this figure, it should be noted that the cells were randomly adhered on the as-cast Vitreloy 105 surface. However, many cells on the groove textured surface are aligned along the troughs or around the protrusions, indicating preferential adherence, which is likely to impact on cell morphology and behaviour.

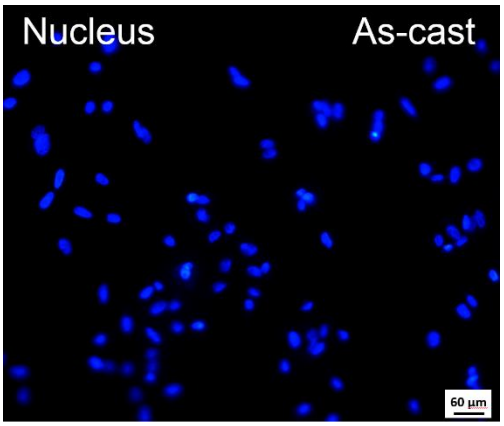

(a)

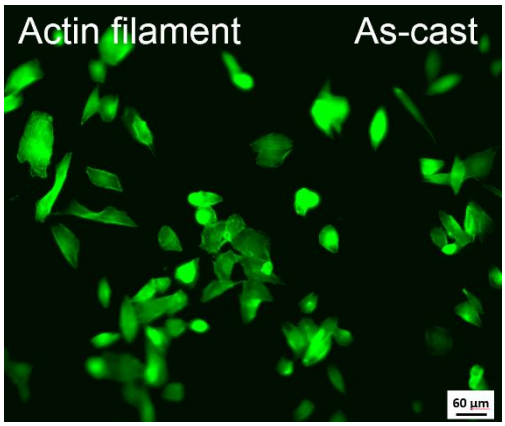

(b)

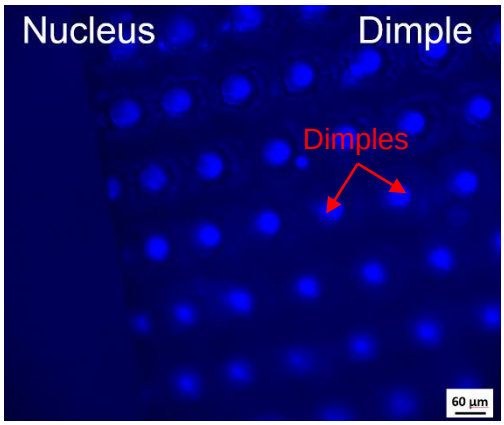

(c)

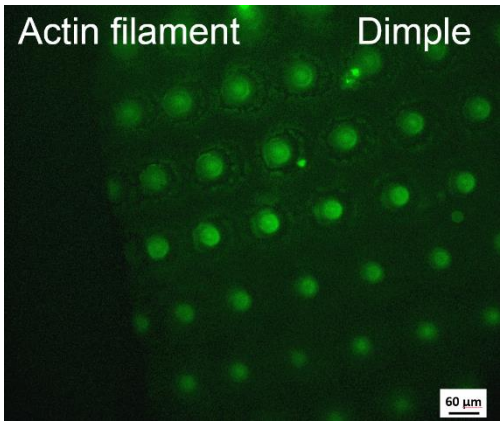

(d)

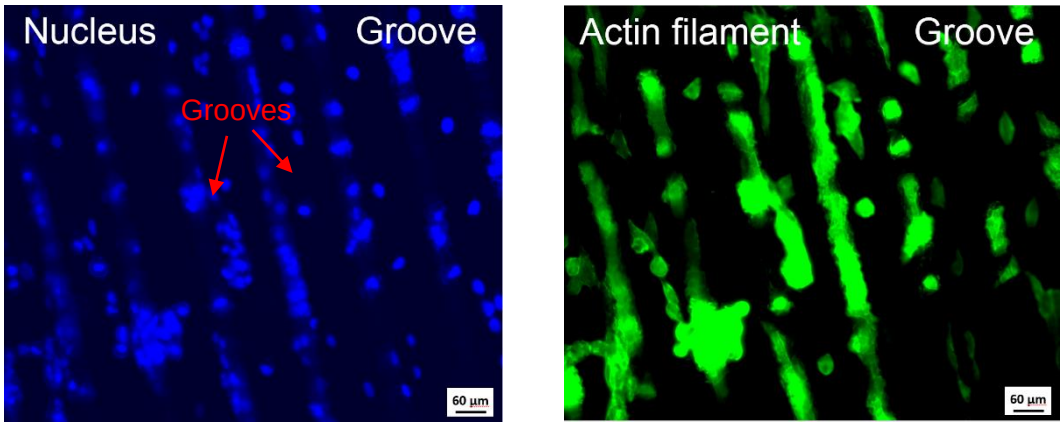

(e) (f)

Figure 6.6: Morphologies of MG63 cells cultured on the $Zr_{52.8}Cu_{17.6}Ni_{14.8}Al_{9.9}Ti_{4.9}$ BMG in the case of as-cast (a) (b), dimple-texture (c) (d) and groove-texture (e) (f); (a) (c) (e) cell nucleus stained with DAPI; (b) (d) (f) actin filament stained with phalloidin.

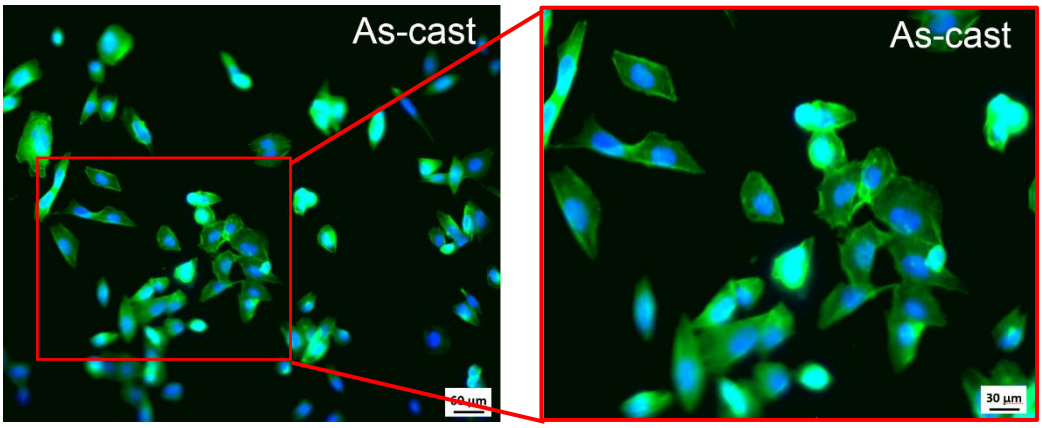

(a) (b)

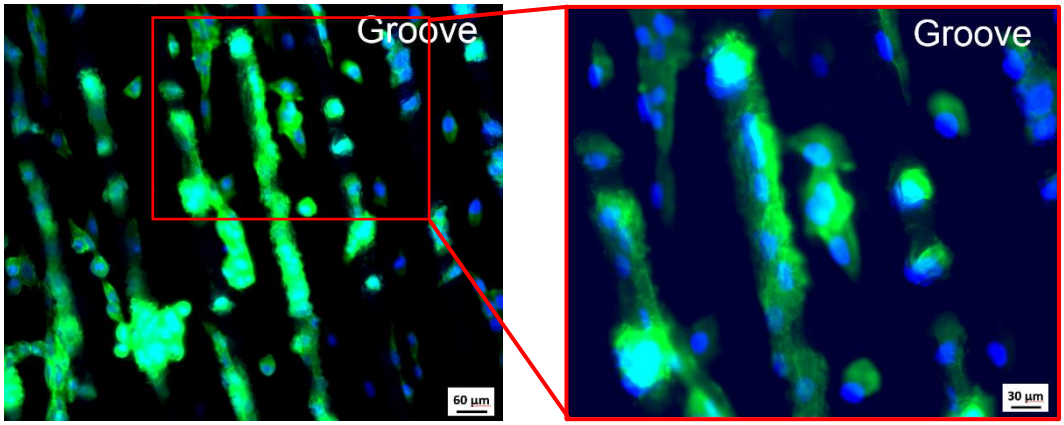

(c) (d)

Figure 6.7: Cell morphologies of the MG63 cells cultured on the $Zr_{52.8}Cu_{17.6}Ni_{14.8}Al_{9.9}Ti_{4.9}$ BMG stained with both DAPI and phalloidin; (a) (b) as-cast; (c)(d) groove-texture; (b) and (d) are the enlarged view of (a) and (c), respectively.

6.4. Discussion

The requirements for a biomaterial to be used for the load-bearing implants, i.e. hip prosthesis, and total joint prostheses, are high hardness, good specific strength and relatively lower Young's modulus, together with a good corrosion resistance. However, the widely used biomedical crystalline alloys, like titanium alloys, stainless steels and CoCrMo alloy, do not possess a good combination of these

properties. For example, the CoCrMo alloy exhibits high hardness and good wear resistance, but the young modulus (210 GPa) is too high, which can lead to stress shielding effects; while the titanium alloy, like Ti-6Al-4V, has the modulus close to the natural bone, but the wear resistance is really poor, which may cause the degradation-induced inflammation. The metallic glass could exhibit a good combination of these properties, which is able to promote their biomedical applications as potential orthopaedic implants, especially the loading bearing devices (Demetriou et al., 2010; Li et al., 2016; Schroers et al., 2009). Some basic mechanical and physical properties of the $Zr_{52.8}Cu_{17.6}Ni_{14.8}Al_{9.9}Ti_{4.9}$ BMG, cortical bone and other traditional biomaterials are listed in Table 6.4. The yield strength of the $Zr_{52.8}Cu_{17.6}Ni_{14.8}Al_{9.9}Ti_{4.9}$ BMG is 2225 MPa, which is double of the strength for Ti-6Al-4V. The higher strength can make smaller and thinner implants possible, and thus leading to less rejection effects of the host tissue to the implants. In addition, the micro-hardness of $Zr_{52.8}Cu_{17.6}Ni_{14.8}Al_{9.9}Ti_{4.9}$ BMG was measured to be 579 Hv, which is 50% higher than Ti-6Al-4V and 316 stainless steel. The higher hardness means good wear resistance (Li et al., 2016), which implies that the $Zr_{52.8}Cu_{17.6}Ni_{14.8}Al_{9.9}Ti_{4.9}$ BMG was more wear resistant than the titanium alloy and stainless steel. As a result, the wear debris-induced inflammation and osteolysis effect (also known as particle disease) can be avoided in a certain degree. Furthermore, the Young's modulus of the $Zr_{52.8}Cu_{17.6}Ni_{14.8}Al_{9.9}Ti_{4.9}$ BMG is 88.6 MPa, which is lower than the other biomedical metals and much closer to that of the cortical bone (10-40 MPa). Based on the Wolff's law, the close Young's modulus between the Zr-based BMG and the cortical bone can make the stress distribute more uniformly than the other biomaterials, thus minimizing stress concentration, avoiding the occurrence of stress shielding-induced failure. The high hardness, good specific strength and relatively low young's modulus have made this Zr-based BMGs to be an ideal candidate material for the load-bearing orthopaedic implants (Demetriou et al., 2010; Li et al., 2016; Schroers et al., 2009).

Fatigue properties also play an important role during the service life of a load-bearing implants. The fatigue limit of the $Zr_{52.8}Cu_{17.6}Ni_{14.8}Al_{9.9}Ti_{4.9}$ BMG under 10^7 loading cycles is measured to be 907 MPa, which is much higher than that of the Ti-6Al-4V alloy (310-816 MPa, Long et al., 1998 and Niinomi et al., 1998) and at a similar level to that of the CoCrMo alloy (207-970 MPa, Niinomi et al., 1998). Excellent high-cycle fatigue strength can prolong the service life, and the high-cycle fatigue strength of the $Zr_{52.8}Cu_{17.6}Ni_{14.8}Al_{9.9}Ti_{4.9}$ BMG makes it to be promising for applications as heavy load bearing parts, such as joints or thighbone. Prior to being used in the body, the biocompatibility assessment has to be done. As an in-vitro assessment method, cellular response has been a powerful technique to evaluate the biocompatibility of a potential bio-material. It was reported on the medical grade Ti-6Al-4V titanium alloy that surface texture can enhance the bio-compatibility of the materials (Chen et al., 2007). Therefore, the nanosecond fibre laser was used to texture the surface of $Zr_{52.8}Cu_{17.6}Ni_{14.8}Al_{9.9}Ti_{4.9}$ BMG, and the biocompatibility was investigated in this study.

Table 6.4: Mechanical properties of $Zr_{52.8}Cu_{17.6}Ni_{14.8}Al_{9.9}Ti_{4.9}$ BMG, cortical bone and other biomaterials.

Materials	Young's modulus(GPa)	Fracture strength(MPa)	Hardness (Hv)	Fatigue limit(10^7 cycles, MPa)	Density (g cm^{-3})	Source
Zr-based BMG	88.6	2225	579	907	6.73	(Glade et al., 2000)
Cortical bone	10-40	130-150	63-75	20-60	0.7-1.85	(Long et al., 1998 and Niinomi et al., 1998)
Ti-6Al-4V	110	760-1050	320	310-816	4.4	(Long et al., 1998 and Niinomi et al., 1998)
316 SS	200	190-690	365	200-800	7.9	(Long et al., 1998 and Niinomi et al., 1998)
CoCrMo alloy	200-230	600-1795	345-390	207-970	8.3	Niinomi et al., 1998

6.4.1 Effects of surface chemical composition

Enhanced cellular attachment and cell viability were clearly observed on the GT surface, as evidenced in Fig. 6.5 and Fig. 6.6. It was reported by Ohtsu et al. (2015) that enhanced cell adhesion was attributed to improved surface hydrophilicity. The effect of the carbon group evolution during the laser process has already been discussed in chapter 5, and the hydrophilicity variation of these three different surfaces resulted from the combined effects of surface roughness and carbon groups. In addition to the wettability, the chemical composition can play a negative

role in the resulting bio-compatibility, especially the potential toxicity of copper, nickel and aluminium elements (Huang et al., 2012a; Rae, 1986; Wang et al., 1997). The surfaces of the $Zr_{52.8}Cu_{17.6}Ni_{14.8}Al_{9.9}Ti_{4.9}$ BMG considered here however were found to mainly consist of TiO_2, ZrO_2 and Al_2O_3, as evidenced by the XPS results. These oxides can act as a barrier, avoiding the release of toxic elements from the original metallic glass surface. As a result, such elements may not directly interact with cells, allowing their survival on Vitreloy 105 surfaces, whether as-cast or laser-irradiated.

6.4.2 Effect of surface roughness

As discussed earlier in Chapter 5, the increase in surface roughness has a positive effect on the hydrophilicity of the laser processed $Zr_{52.8}Cu_{17.6}Ni_{14.8}Al_{9.9}Ti_{4.9}$ BMG. According to Huang et al. (2011), who also conducted cellular response experiments on a Zr-based BMG, in addition to the chemical composition, the roughness of a surface can also affect cell behaviour. For example, in the case of laser textured Ti-6Al-4V surfaces, it was reported that the rougher the surface, the more features (e.g. redeposited vapour particles and sharp ridges) are available as focal points for the cells to adhere to (Chen et al., 2009). In the study reported in this chapter, a higher level of cell attachment (c.f. Fig. 6.6) was observed for the GT surface, while there were almost no cells attached on the DT sample. Moreover, on the GT surface, the MG63 cells were mainly distributed along the troughs or around the protrusions, where the surface roughness is higher than that of the flat, unprocessed area. This observation is in-line with the reports from Huang et al. (2011). This relationship between increased roughness and improved cell attachment is applicable to the GT sample, but it does not hold for the DT specimen. Indeed, the roughness of the DT surface is higher than that of the as-cast sample, but cell attachment was not found to be improved with the dimple pattern. At the

same time, it was found that the hydrophilicity of the AC surface was enhanced by the laser-induced groove patterns but weakened by the laser-induced dimple patterns. Thus, it can be said that the cell attachment results show a good consistency with the wettability observations of these three samples. Therefore, it can be concluded that while surface roughness can affect cell attachment, it is not the only factor determining this aspect of cell behaviour.

Several research investigations have shown that cells align along grooves (Anselme et al., 2002; Chen et al., 2009; Chesmel et al., 1995), depending on their dimensions, especially as a function of the depth of the micro-grooves. In particular, it was reported that cells can elongate along or parallel to 5 μm deep grooves, but randomly orientate when grooves were only 0.5 μm in depth (Anselme et al., 2002). In this study, the surface roughness of the groove-textured sample was measured to be 3.54 μm and the average depth of the grooves was measured to be about 10 μm. Thus, it is believed that the depth of the grooves generated here was large enough for many cells to align preferentially along them. In contrast, the observed randomly aligned cells on the as-cast sample surface can be attributed to its relatively smooth surface.

6.4.3 Relationship between cell attachment and wettability

Wettability and surface free energy also contribute to cell attachment (Boyan et al., 1996; Chrzanowski et al., 2008; Ochsenbein et al., 2008; Ponsonnet et al., 2003). In particular, a high surface free energy and increased hydrophilicity can enhance the interaction between an implant surface and its biological environment, cell adhesion and cell spreading (Baier et al., 1984; Schrader, 1981; Schwarz et al., 2009). In the present study, the measured water contact angles for all the samples were smaller than the Berg limit (θ=65°). This indicates that all considered surfaces were hydrophilic (Vogler, 1998). As reported in Figure 6.3 earlier, the contact angle

of the DT surface was the largest, while that of the groove textured surface was the smallest. This means that the dimple pattern resulted in the lowest hydrophilicity while the groove pattern displayed the highest hydrophilicity. By means of wetting with two liquids (distilled-deionized water and ethylene glycol), the surface free energy of the analysed three sample surfaces was also calculated, along with their dispersive and polar components. According to Sarapirom et al. (2013), the polar component of surface energy has a significant effect on wettability as polar molecules can interact with the dipole force and hydrogen bonds, which is beneficial for enhancing wettability. The surface free energy results and the observation of hydrophilic properties for each surface are in line with the cell attachment results. More specifically, the SFE and its polar component for the dimple-textured sample was found to be lower than the other two groups. In contrast, the SFE and its polar component of the groove textured sample surface was the largest.

In addition, cell attachment may relate to protein pre-adsorption as well. It is widely reported that protein adsorption occurs before cells reach the material surface, exposing cell binding domains that may encourage or inhibit cell adhesion (Boyan et al., 1996; Ratner et al., 2004). Therefore, the initial surface texture may have implications on protein adsorption and thus affect cell adhesion. More specifically, fetal bovine serum (FBS), which is the constituent of the cell culture media used in this study, contains proteins such as bovine serum albumin (BSA) and fibronectin which play roles in cell attachment. BSA can partially inhibit osteoblast attachment whilst fibronectin can mediate attachment. It was reported that BSA preferentially adsorbs onto smooth surfaces, whilst fibronectin adsorbs more preferably on rough surfaces (Boyan et al., 1996; Yang et al., 2003). As a result, preferential binding of BSA on smooth as-cast surfaces are likely to inhibit cell attachment, which would offer an alternative explanation for the observations made in this study. On the contrary, the rough GT sample surface displayed good cell attachment, which may

be attributed to greater levels of fibronectin adsorption. Further work investigating the attachment of these serum proteins to these surfaces however is required to test this hypothesis. In addition, protein adsorption can also correlate with the surface hydrophilicity and surface free energy (Ochsenbein et al., 2008), highlighting the complex biological process of cell attachment to implant surfaces.

In general, in light of the cellular response of the osteoblast-like MG63 cells on the $Zr_{52.8}Cu_{17.6}Ni_{14.8}Al_{9.9}Ti_{4.9}$ BMG, it can be concluded that this Zr-based BMG has no toxic effect and that the best bio-compatibility is achieved on the groove-textured sample surface. This is due to its enhanced hydrophilicity, high SFE and surface roughness as well as the increase of metallic oxides. The corrosion resistance is also of utmost important for implants due to the aggressive environment encountered *in-vivo*. Corrosion resistance determines the likelihood and rate of released metal ions from implants which can affect bio-compatibility, mechanical properties and failure rates. Therefore, investigations in metal ion release via biocorrosion studies and enhanced corrosion resistance via surface treatment techniques remain a vital issue. Further investigations on the biocorrosion resistance and *in-vivo* animal testing are still required to gain a more comprehensive understanding of the bio-compatibility of laser-textured Vitreloy 105 BMG surfaces.

6.5. Conclusions

Two types of surface pattern, i.e. dimples and grooves, were fabricated on the surface of the Vitreloy 105 via nanosecond pulsed fibre laser irradiations. In particular, the bio-compatibility of this BMG, was investigated using cellular response studies of osteoblast-like cells (MG63) for different surface conditions, i.e. as-cast, dimple-textured and groove-textured. The surface roughness, chemical composition, and wettability as well as the surface free energy of all

samples were assessed and compared. The viability of the MG63 cells was evaluated using the CCK-8 assay on the different types of surface patterns. Comparisons of cell attachment and cell morphology were also made via fluorescent image analysis. Finally, the effects of surface chemistry, roughness and surface free energy on bio-compatibility were discussed in an attempt to explore the underlying laser-induced physical modifications for different patterns.

Vitreloy 105 metallic glass was found to be non-cytotoxic to MG63 osteoblast-like cells in this study. This is attributed to the presence of a surface oxide layer composed of TiO_2, Al_2O_3 and ZrO_2. This study also showed that cell viability and attachment could be modified on purpose via laser surface texturing and that bio-compatibility results agreed well with the wettability of the resulting surfaces. More specifically, cell viability and attachment could be enhanced by laser texturing grooves on the Vitreloy 105 surface, while cell attachment was reduced in the case of dimple texturing. In addition, it was found that cells preferentially orientated along the grooves whilst attachment direction was random for the as-cast samples. Finally, the cell adhesion observations correlated with the surface free energy measurements, which may be influenced by protein adsorption.

Chapter 7 Softening and hardening on the $Zr_{52.8}Cu_{17.6}Ni_{14.8}Al_{9.9}Ti_{4.9}$ bulk metallic glass induced by nanosecond laser surface melting

7.1 Introduction

The study reported in this penultimate chapter was conducted to investigate the influence of laser surface melting (LSM) on the mechanical properties, specifically hardness and shear banding behaviour of Vitreloy 105. More specifically, by conducting LSM operations on Vitreloy 105 in ambient atmosphere using the available nanosecond laser, a microhardness tester was used firstly to evaluate the surface hardness evolution of this BMG treated with different laser parameters. In addition, the surface residual stress distribution and microstructure changes of the BMGs before and after laser surface melting process were characterised by SEM, XRD and the FIB-DIC technique. Following this, a nanoindentation instrument was employed to explore the effect of LSM on the shear banding behaviour of as-cast and laser-irradiated Vitreloy 105 surfaces as an indirect method to reflect the plasticity evolution on different BMG samples. Finally, the driving mechanisms induced by LSM on the hardness and shear banding behaviour were proposed from the perspectives of LSM-induced residual stress distribution and microstructure evolution.

7.2 Specific experimental methods

7.2.1 Laser surface melting: specific experimental plan

The laser surface melting process was carried out by the fibre laser with a frequency of 80 kHz and a pulse duration of 65 ns at various beam scanning speed, laser fluence and scanning times. The laser beam travelled from a pre-defined starting edge of the treated area to a finished edge in the x direction for a distance L, thus completing one track. The first irradiated spot for the subsequent track was set at a distance increment, D_s, of several micrometres in the y direction. In this study, all the values of D_s were set to be 20 μm, so the overlap along the y direction was calculated to 37.5%. Unlike the laser micromachining process implemented in Chapter 4, for which the focus was to remove material, the laser surface melting operations conducted here are concerned with the modification of the mechanical properties of the BMGs via laser-induced rapid heating and cooling (see Figure 7.1). Therefore, a set of lower laser fluence values (less than 4.04 J/cm^2) with a shorter pulse duration (65 ns) were exploited. The detailed laser parameters used in the present study are shown in Table 7.1.

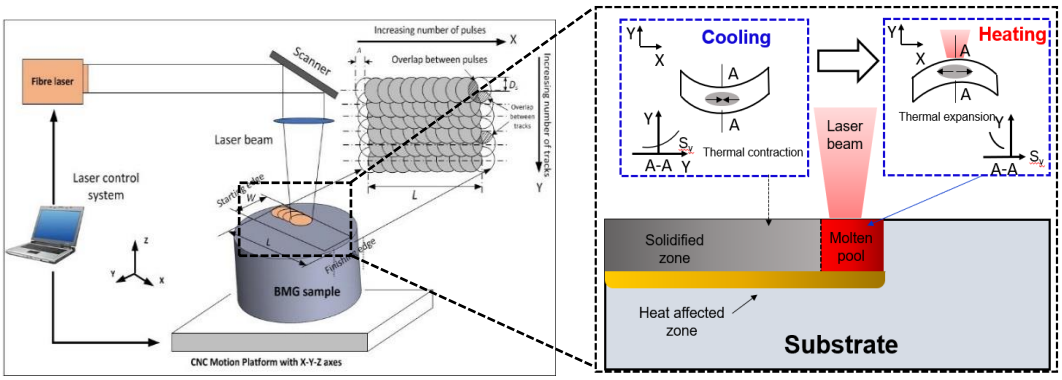

Figure 7.1: Schematic diagram of the laser surface melting process.

Table 7.1: Detailed laser parameters used for the laser irradiation experiments.

Wavelength (nm)	Spot diameter (μm)	Pulse duration (ns)	Frequency (kHz)	Track distance (μm)	Laser fluence (J/cm^2)	Scanning speed (mm/s)	Scanning times
1064	32	65	80	20	3.42	800	1
					3.73	800	1
					3.89	800	1
					4.04	800	1
					4.35	800	1
					4.04	600	1
					4.04	400	1
					4.04	200	1
					4.04	800	5
					4.04	800	10
					4.04	800	20

7.2.2 Material preparation for microstructure characterisation

In order to observe the microstructure of selected cross sections, specimens were etched for 10 s using a solution of 10 vol.% HF + 90 vol.% H_2O (Bian et al., 2001), then examined using the scanning electron microscope.

7.3 Results

7.3.1 Qualitative analysis of the surface topography

SEM micrographs of surfaces irradiated with different laser fluence values, namely 3.42 J/cm^2, 3.84 J/cm^2 and 4.35 J/cm^2, for a fixed scanning speed and after one irradiation cycle only, are shown in Figure 7.2. It can be clearly seen from this figure that, under the lowest laser fluence considered (3.42 J/cm^2), no obvious craters were formed on the surface. However, flake-type features are apparent between laser tracks. It is suggested that these features are remains of the original oxide layer on the surface of the as-cast sample. Indeed, the backscattered electron

(BSE) detector image shown in Figure 7.2(b) reveals that these features correspond to regions with a darker contrast. Interestingly, on the surface of samples treated with the slightly higher fluence of 3.89 J/cm^2, these flake-type features were not present anymore (see Figure 7.2(c)) while the resulting surface topography is still relatively unchanged. The corresponding BSE detector image shown in Figure 7.2(d), shows that the original oxide layer was indeed removed completely in this case. Under the highest laser fluence, (4.35 J/cm^2), overlapped disk-shaped features can be observed. These features, which are 18 µm in diameter and thus, smaller than the laser spot diameter, were formed by re-solidified melt. In addition, a higher magnification image (see Figure 7.2 (g)) shows that no vapour particles were re-deposited on the surface of this sample. This means that even at the highest fluence value selected in this study, laser melting was still the dominant processing regime; as opposed to laser ablation in the reports introduced in Chapter 2 from Tariq et al. (2009), Mudry et al. (2013) and Huang et al. (2019).

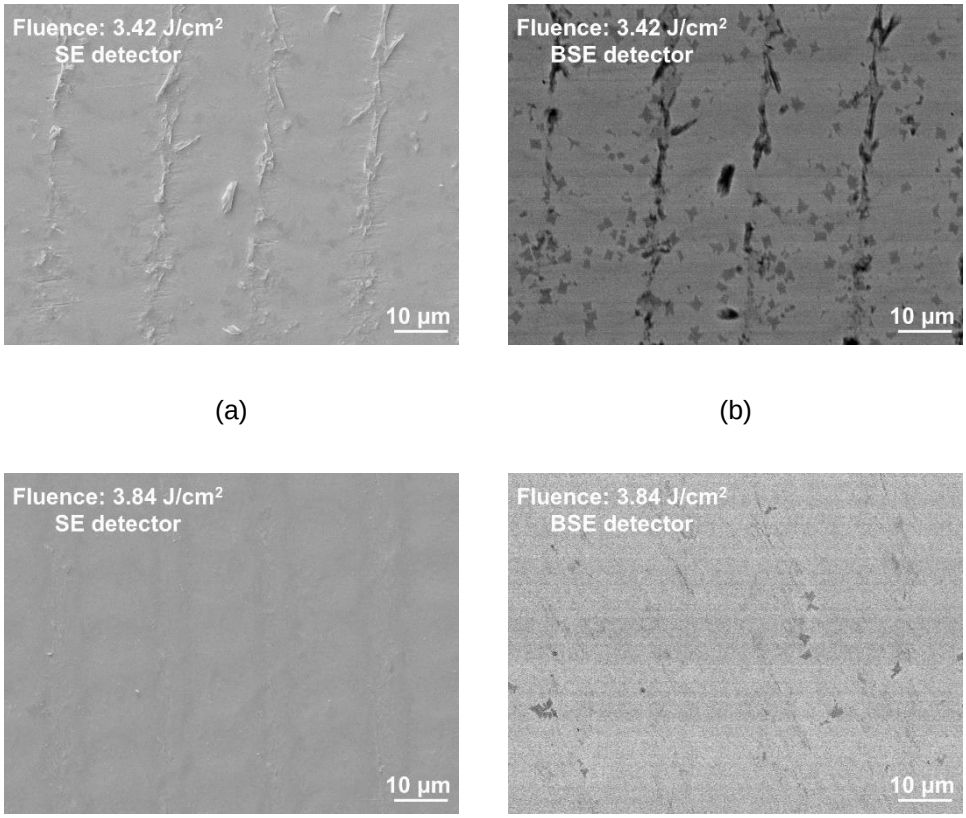

(c) (d)

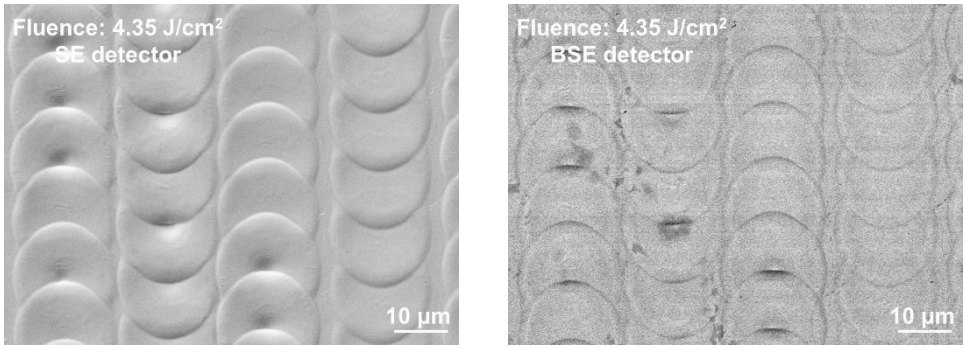

(e) (f)

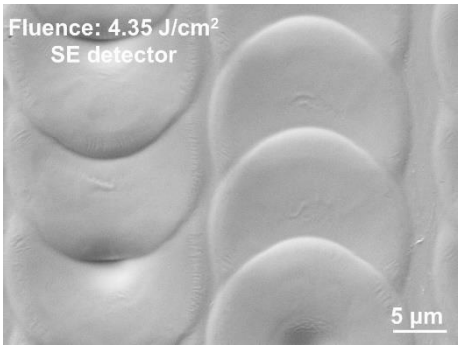

(g)

Figure 7.2: Secondary electron (SE) images of the surface of the Vitreloy 105 BMG following LSM with fluence values of (a) 3.42 J/cm^2 (c) 3.89 J/cm^2 and (e) 4.35 J/cm^2 under a fixed scanning speed of 800 mm/s and one irradiation cycle; (b), (d) and (f) are the corresponding back-scattered electron (BSE) images of (a), (c) and (e), respectively; (g) is a magnified SE image of (e).

7.3.2. Vickers micro-hardness tests

Hardness is an important property that can affect the wear resistance of metallic glasses. Greer et al. (2002) reviewed micro-hardness values of several amorphous alloys available in the literature and their corresponding wear resistance. They reported that, for a given class of alloy composition, the harder the material was,

the higher the wear resistance tended to be. Thus, the ability to harden BMGs via LSM could have interesting practical applications where a combination of strength, large elastic limit, corrosion and wear resistance are required, such as in orthopaedic implant materials, for instance.

Results of the Vickers micro-hardness tests conducted on the surface of the Vitreloy 105 samples under different LSM processing conditions are presented in Figure 7.3. The average hardness of the as-cast sample was measured to be 495.7HV_2. The standard deviation associated with this data (± 7.7HV_2) was relatively small, suggesting that the hardness distribution on the surface of the as-cast sample was quite homogeneous. In contrast, it is also observed from this figure that, after LSM, micro-hardness values tended to be less homogeneous for all laser processing conditions, as evidenced by larger standard deviations. In particular, for the sample treated with the highest fluence, 4.35 J/cm^2, the standard deviation was also the largest, i.e. ± 24.7 HV_2, and thus almost threefold that of the as-cast sample. Such a wider spread of hardness values may be attributed to the introduction of laser-induced surface patterns as well as microstructural changes (Huang et al., 2019).

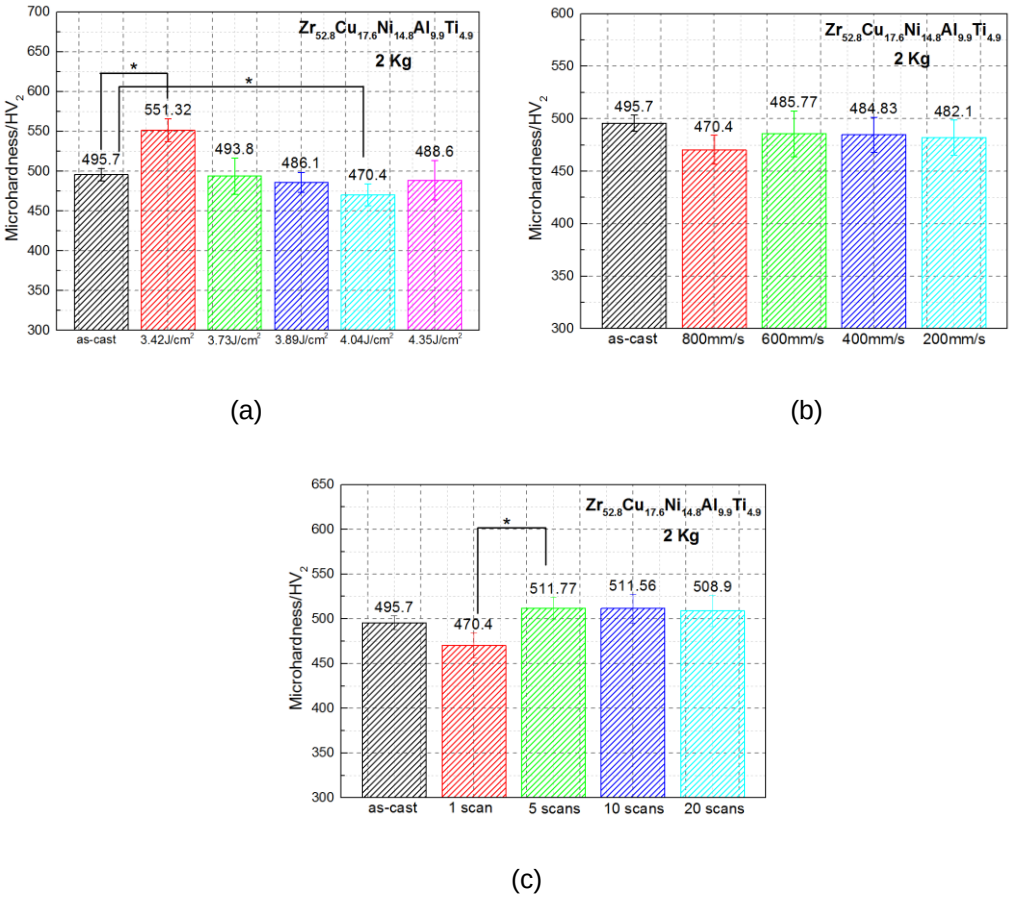

Figure 7.3: Surface hardness values of Vitreloy 105 treated with (a) different laser fluence values for a fixed scanning speed of 800 mm/s and one irradiation cycle; (b) different scanning speed values for a fixed fluence of 4.04 J/cm^2 and one irradiation cycle; (c) various number of irradiation cycles for a fixed fluence of 4.04 J/cm^2 and a scanning speed of 800 mm/s. The t-test was conducted on certain pairs of presented data; the inclusion of the symbol * in this figure indicates that the means of these sets of data were found to be significantly different from each other.

A comparison of the micro-hardness after LSM for different laser fluence values is provided with the bar chart in Figure 7.3(a). Of relevance to one of the motivations of this study, the results indicate that LSM operations could result in surface hardening depending on the employed laser fluence, in addition to the well-documented softening. This effect appears particularly pronounced for the pair of

values 3.42 J/cm^2 and 4.04 J/cm^2, which are associated with apparent hardening and softening, respectively. The completion of the t-test confirmed that the mean hardness of 551.32 HV_2 for the sample processed with the lower fluence of 3.42 J/cm^2 was statistically different, and thus higher (by 11.2%), than that of the as-cast sample. This test was also employed to confirm that the mean hardness of 470.4 HV_2 for the sample processed with the fluence of 4.04 J/cm^2 was lower (by 5.1%) than that of the as-cast sample. Given the relatively small difference between both fluence values, i.e. less than 1 J/cm^2, it is important to note that the hardness on the surface of Vitreloy 105 appears to be very sensitive to variations in delivered energy.

For a fixed fluence and a single irradiation cycle, the effect of different scanning speed on surface hardness is shown in Figure 7.3(b). In this case, it can be observed that the average micro-hardness did not vary significantly between scanning speed values. This indicates that this parameter does not have an important influence on the resulting hardness, at least for the range of values considered in this study. In addition, the effect of the number of irradiation cycles is shown in Figure 7.3(c) for fixed values of delivered fluence and scanning speed. From this particular bar graph, it can be noted that the micro-hardness reduced compared to that of the as-cast sample when only one irradiation cycle was applied. However, the hardness then increased with additional irradiation cycles and remained relatively stable after 5 cycles. In addition, the outcome of the student t-test showed that the mean micro-hardness values could indeed be considered significantly different between 1 cycle and 5 cycles of irradiation. This suggests that this parameter could also be influential on the micro-hardness resulting from LSM, in addition to the effect of the fluence noted earlier. However, given the fact that the micro-hardness remained almost unchanged after a certain number of cycles, it could also be said that there is an effective interval in which the number of irradiation cycles could have such an influence. In addition to the results reported

above, the effect of the laser fluence on 1) the residual stress distribution, 2) the microstructural evolution and 3) the shear banding behaviour of Vitreloy 105 is presented in the following sections. These subsequent experimental data are obtained for the samples irradiated with the specific fluence values of 3.42 J/cm^2 and 4.04 J/cm^2, in addition to the as-cast specimen. The rationale behind this selection is that this pair of fluence values resulted in the largest hardness increase and decrease, respectively, compared to the original hardness of the as-cast material.

7.3.3. Residual stress distribution

Residual stress is proven to have a significant effect on mechanical properties, such as the plasticity (Cao et al., 2015; Zhang et al., 2006), of bulk metallic glasses. It is known that residual stress can be induced during melting and solidification, phase transformation and mechanical treatment processes (Noyan and Cohen, (2013)). During pulsed LSM, the irradiated BMG surface experiences rapid heating and cooling cycles during which high thermal gradients can be generated along the in-depth direction. As a result, residual stress can be introduced on the target material. As mentioned earlier in this Thesis, the effect of LSM on the residual stress distribution was assessed by applying the ring-core FIB milling and DIC technique. The quantitative results obtained for the as-cast sample and for specimens processed with the selected fluence values of 3.42 J/cm^2 and 4.04 J/cm^2 are given in Figure 7.4. In particular, Figure 7.4(a) shows the average near-surface residual stress for all these three specimens of interest. From this figure, it can be seen that the near-surface residual stress for the sample treated with the lower fluence of 3.42 J/cm^2 presented a compressive state compared to the as-cast material. On the contrary, the introduction of tensile residual stress was detected for the sample treated with the higher fluence of 4.04 J/cm^2. These results

are in-line with the micro-hardness measurements presented earlier. In particular, the observed hardening of the surface for an applied fluence of 3.42 J/cm^2 is accompanied with the introduction of compressive residual stress, while the softening effect observed for the fluence of 4.04 J/cm^2 is associated with the presence of tensile residual stress.

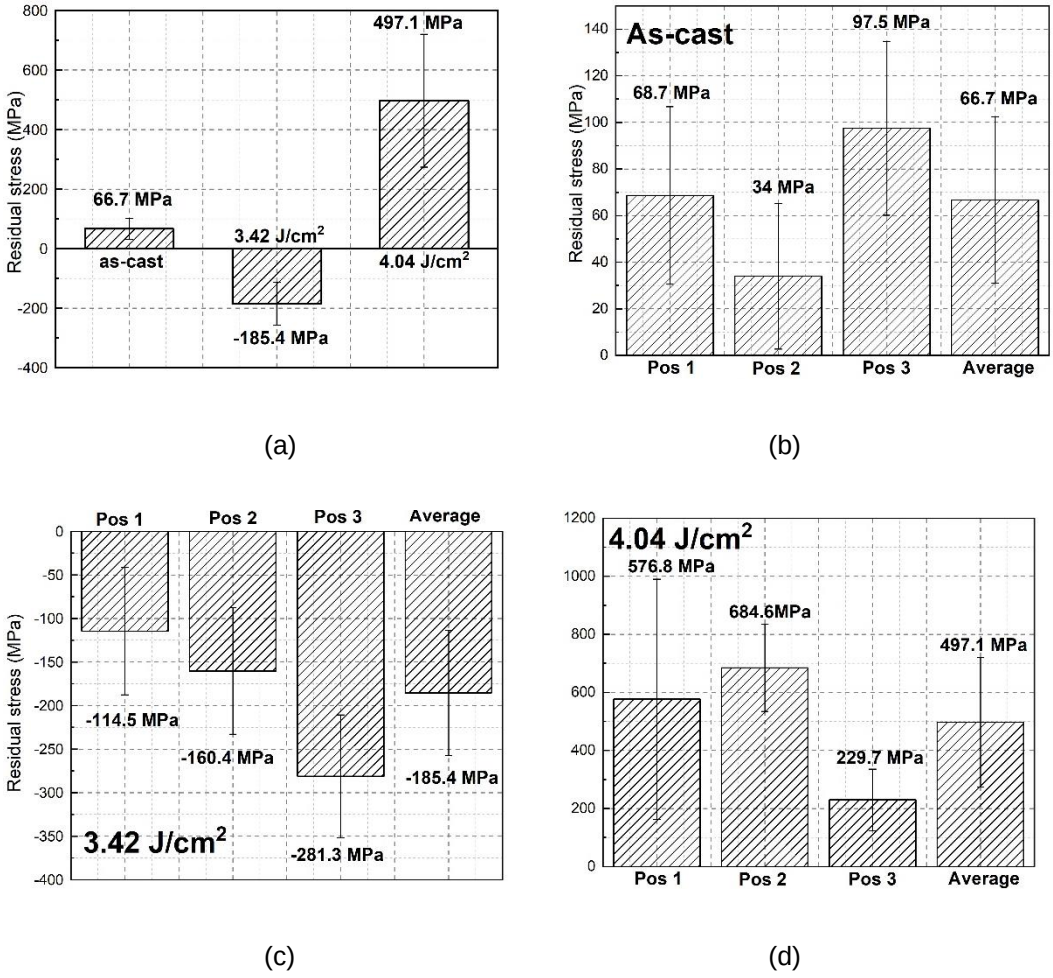

Figure 7.4: (a) Comparison of average near-surface residual stress between the selected Vitreloy 105 samples; individual and average residual stress values for (b) the as-cast sample; (c) the hardened sample LSM treated with a fluence of 3.42 J/cm^2; (d) the softened sample LSM treated with a fluence of 4.04 J/cm^2.

7.3.4. Microstructure analysis

Figure 7.5 shows the XRD patterns of the Vitreloy 105 BMG prior to and after LSM operations. As can be seen from this figure, the XRD pattern of the as-cast sample shows an overall amorphous halo with two crystalline peaks. After laser irradiation with the fluence of 3.42 J/cm^2, two crystalline peaks of Al_2NiZr_6 and an additional $CuZr_2$ peak were introduced. In contrast, with a higher laser fluence of 4.04 J/cm^2, no new crystalline phases formed and the intensity of the original $CuZr_2$ peaks was even reduced. Moreover, as seen in Figure 7.5(b), which shows an enlarged view of the XRD patterns, the location of the diffraction peak corresponding to the $CuZr_2$ phase at 25.18° shifted to a slightly lower angle. This smoothened profile and the small change in location of the crystalline peak may be correlated with a refined crystalline phase or the formation of an amorphous microstructure (Gu et al., 2012).

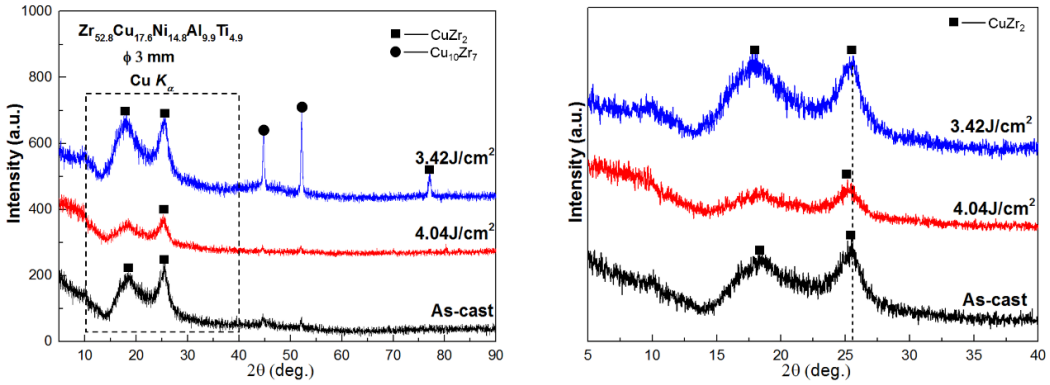

Figure 7.5: (a) XRD patterns of Vitreloy 105 BMG specimens prior to and post laser surface melting; (b) enlarged view of (a) in the range 5-40°.

The fact that the sample treated with a fluence of 3.42 J/cm^2 displayed a higher degree of crystallinity is in-line with related literature presented in Chapter 2, section 2.4, since this specimen also exhibits an increased hardness. However, it

is perhaps counter-intuitive to observe that when the fluence was further increased to 4.04 J/cm^2, then the surface became more amorphous. To confirm this particular observation, the morphology of the etched cross-section for the as-cast and the sample treated with this higher fluence of 4.04 J/cm^2 were further compared. The resulting SEM images are given in Figure 7.6. It can be seen that compared to the microstructure of the as-cast sample, the grains in the near-surface region appear refined following the LSM treatment, which is consistent with the XRD results. The fact that a higher fluence led to a refined crystalline phase and the formation of a more amorphous layer near the surface may be attributed to the higher cooling rate induced by the increased laser fluence and consequent rapid heating and cooling cycles during LSM operations.

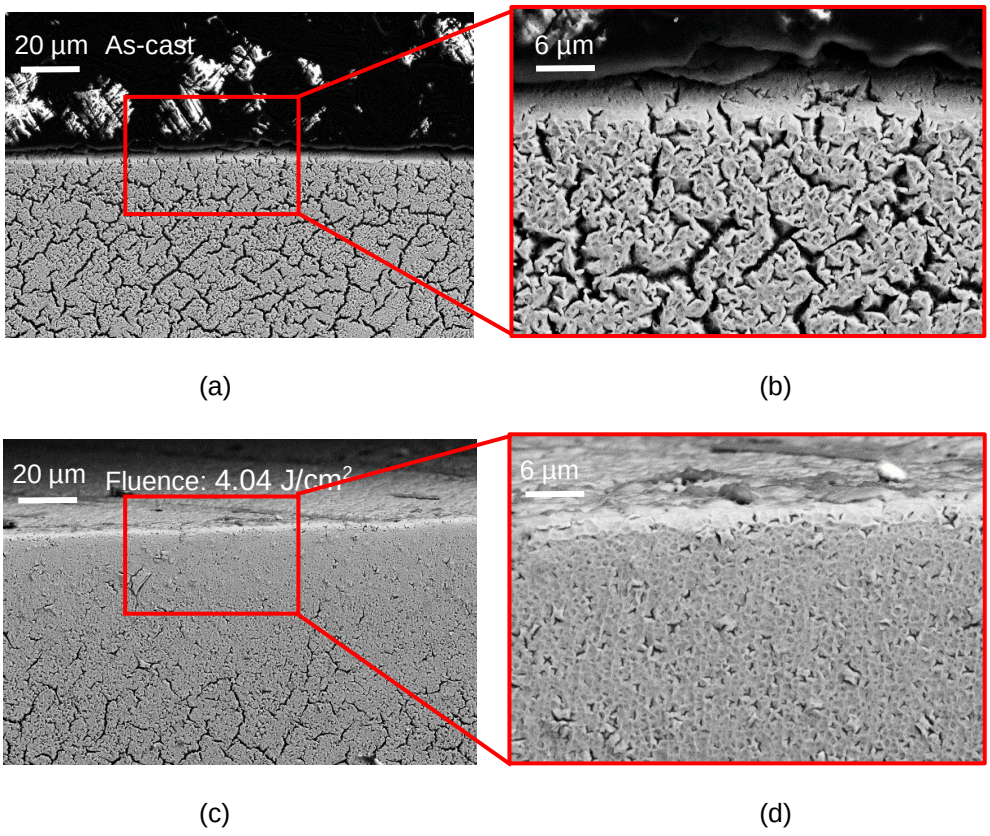

Figure 7.6: Cross-sectional SEM micrographs of the BMG specimens: (a) and (b) as-cast; (c) and (d) following LSM with a fluence of 4.04J/cm^2.

7.3.5. Nanoindentation tests

As reported in Chapter 3, section 3.5.3, discontinuous depth bursts in load-depth (*P-h*) curves obtained via nanoindentation tests are considered to be directly related to shear banding activity, i.e. nucleation, propagation and blockage and/or cessation, inside and on the surface of BMGs (Cao et al., 2015; Huang et al., 2019). Thus, insight into the plastic deformation behaviour of BMGs can also be gained through the analysis of such discontinuous depth bursts, also referred to as serrated flows. Such data can be obtained via the continuous recording of the mechanical response of the specimen during a nanoindentation cycle. Figure 7.7 shows the load-depth (*P-h*) curves of the as-cast and post-LSM samples. As could be expected, and in-line with the Vickers micro-hardness results, the maximum penetration depth was found to be the lowest (i.e. 924 nm) for the sample displaying a hardened surface post-LSM, while the highest penetration depth (i.e. 945 nm) was measured for the specimen with a softened surface. More interestingly, from the insets also included in this figure, which show magnified portions of the *P-h* curves, it is visible that serrated flows (discontinuous bursts) are quite prominent on both the as-cast sample and the specimen treated with 4.04 J/cm^2. In comparison, the *P-h* curve for the sample irradiated with 3.42 J/cm^2 is quite smooth.

In order to compare the serrated flow behaviour in a more systematic way, the depth-difference method was implemented on the recorded *P-h* data, as was also the case in previous studies (Huang et al., 2018, 2019; Huang et al., 2012b). As explained earlier (see Chapter 3, section 3.5.3), when implementing this method, one single serrated flow event on the *P-h* curve is characterised by one sharp peak in the resulting depth-difference curve. The number and height of such peaks thus represent the number and intensity of serrated flows on the corresponding *P-h* curves. Results from applying the depth-difference method are also included in

Figure 7.7. From a purely qualitative observation of these graphs, it appears that the number and magnitude of the sharp peaks for the hardened sample post-LSM are reduced compared to data extracted for the as-cast sample. Again, solely from a qualitative perspective, the number and magnitude of such peaks seem to be slightly higher for the softened sample post-LSM. In order to provide a more quantitative analysis, Table 7.2 gives the number of peaks, which were recorded to be larger than 2 nm, as well as the total distance covered when adding all such peaks together, for all three samples. From this table, it becomes obvious that the sample softened following LSM with 4.04 J/cm^2 displayed the largest number of large-sized serrated flow events, while the hardened sample post-LSM, i.e. with a fluence of 3.42 J/cm^2, led to the smallest number. These results will be further discussed in the next section. It is quite apparent however, that the LSM operations conducted here could not only promote but also reduce serrated flow events for the treated Vitreloy 105 surface. In turn, this suggests an associated influence on the plastic deformation behaviour of this material post-LSM depending on the irradiation conditions.

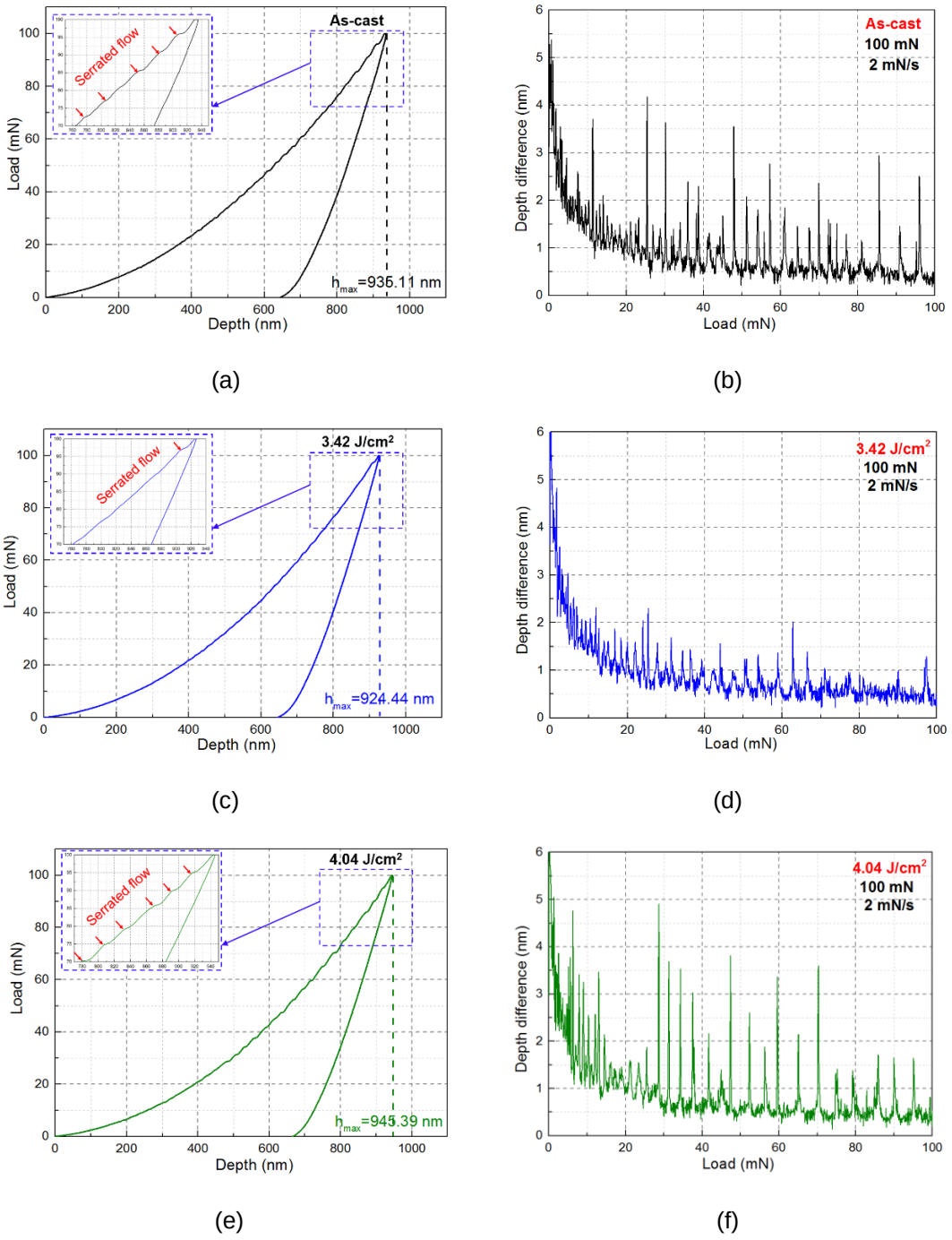

Figure 7.7: Load-depth curves and corresponding depth-difference curves: (a) and (b) for the as-cast sample; (c) and (d) for the LSMed sample treated with 3.42J/cm^2; (e) and (f) for the LSMed sample treated with 4.04J/cm^2.

Table 7.2: Quantitative results obtained from the depth-difference method to characterise serrated flow events being over 2 nm in the load range 10-100 mN.

	As-cast	3.42 J/cm^2	4.04 J/cm^2
Number of depth-difference peaks being over 2 nm	20	5	26
Total distance when adding all depth-difference peaks being over 2 nm (nm)	53.45	10.76	72.95

In order to provide further experimental elements of discussion regarding the effect of LSM treatment on the shear banding behaviour near the surface of BMG specimens, the topography of typical pile-ups formed on the side of the nano-indents was analysed using AFM (see Figure 7.8) and SEM images (see Figure 7.9). Interestingly, numerous macroscopic shear bands were observed to reach the surface near nano-indents for the hardened sample post-LSM, while the softened sample displayed a reduced number of such surface shear bands and the as-cast sample almost none. The height of these pile-ups also tended to be highest for the hardened sample (see Figure 7.8(d) as an example). The literature reports that an increased number of discrete bursts, or pop-ins, visible in the *P-h* curve corresponds not only to more pronounced shear banding activity but also this generally results in more shear bands reaching the surface near nano-indents (Golovin et al., 2001; Yoo et al., 2007). However, this is not the case in the present study. In fact, the number of shear band emerging on the surface is the highest for the sample displaying reduced shear banding activity. As will be discussed in the next section, this somewhat counter-intuitive observation indicates that residual stress might play an important role in the direction of propagation of shear bands, as was observed by Haag et al. (2014).

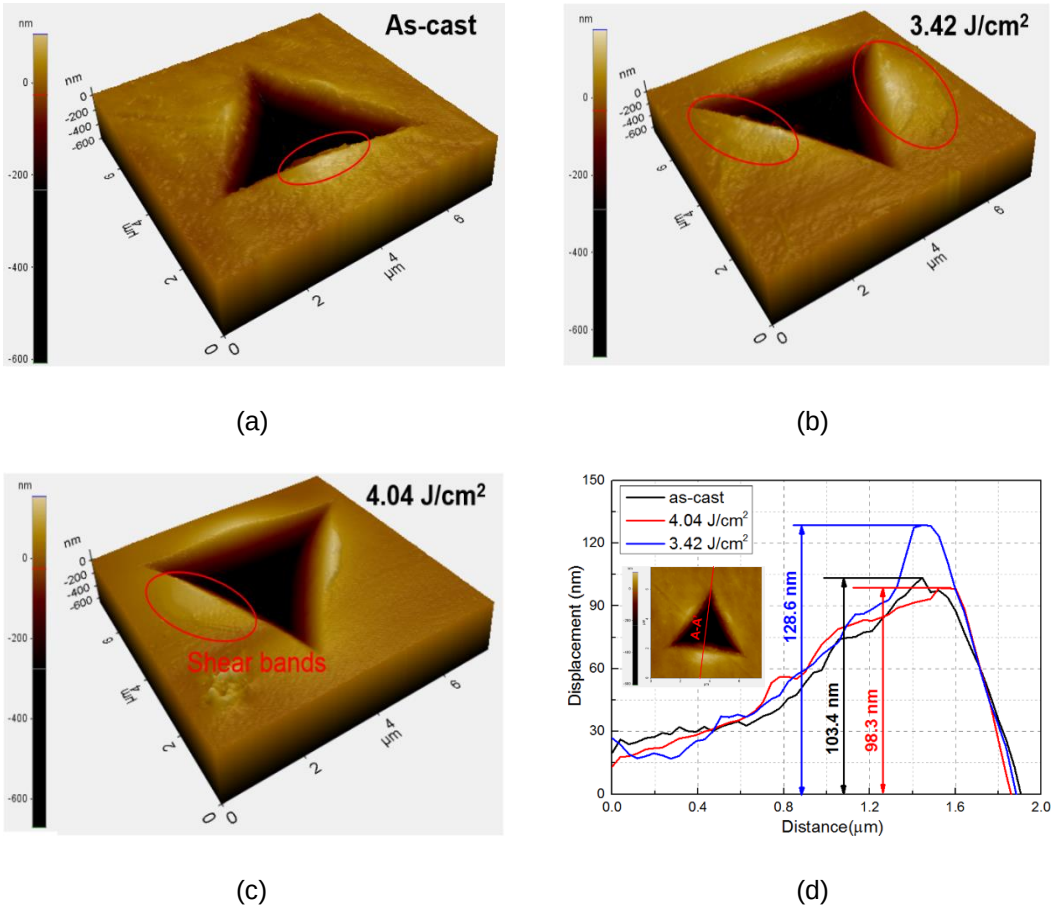

Figure 7.8: Representative 3D topography of nano-indents on the: (a) as-cast sample; (b) LSMed sample treated with 3.42 J/cm^2; (c) LSMed sample treated with 4.04 J/cm^2; (d) corresponding line profiles from the data shown in (a), (b) and (c).

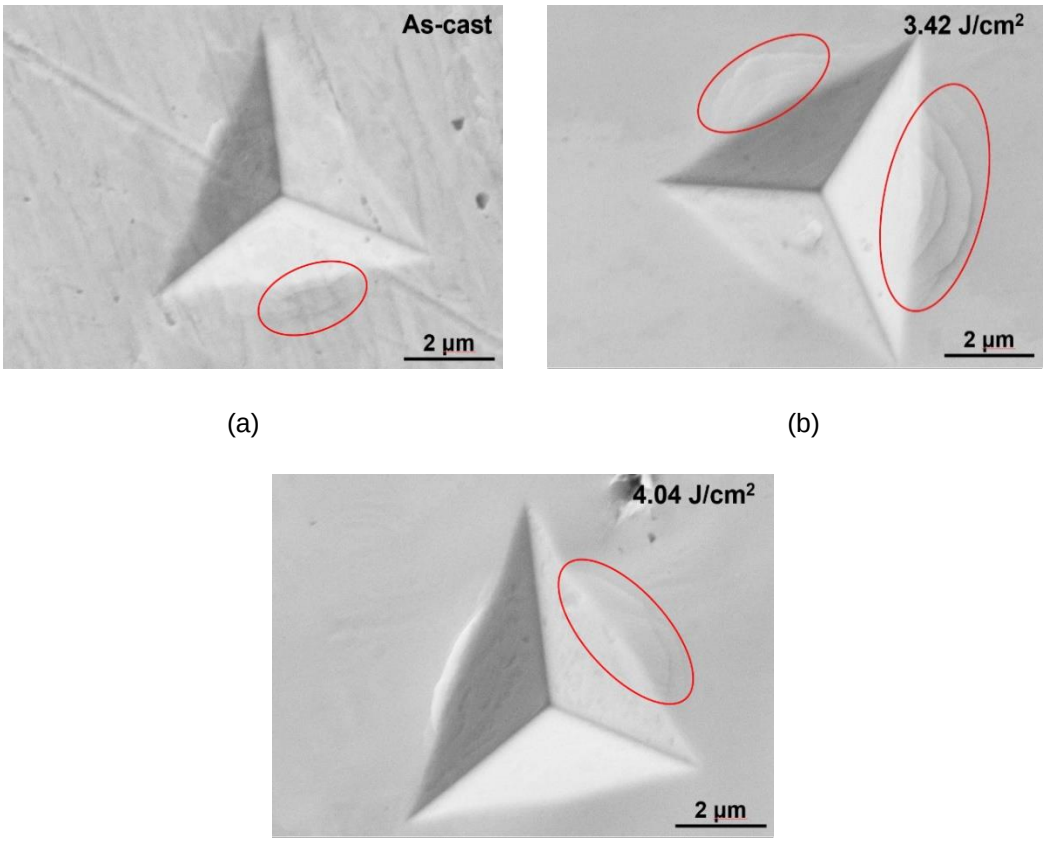

Figure 7.9: Representative SEM micrographs of the residual indent morphology on the surface of (a) as-cast sample; (b) LSMed sample treated with 3.42 J/cm^2; (c) LSMed sample treated with 4.04 J/cm^2.

7.4 Discussion

7.4.1. Effect of LSM on the hardness of Vitreloy 105

An important outcome of the study reported in this chapter is the experimental finding that, depending on the applied laser parameters, and especially the laser fluence, the surface of the irradiated Vitreloy 105 BMG could not only be softened but also hardened as a result of conducting LSM in ambient environment. It was

also found that tensile residual stress was present on the softened surface, while compressive residual stress was measured on the hardened surface. Previous studies that focussed on the effect of residual stress on hardness generally tackled such investigations by measuring the hardness on the cross section of BMG beams pre-stressed elastically in bending (Chen et al., 2008; Wang et al., 2011a). Findings from these reports suggest that a reduction in hardness takes place in regions of induced tensile stress, while such a correlation tends to be less obvious between increased pre-existing compressive stress and increased hardness, except at relatively high stress level (Haag et al., 2014). Thus, the observed increase in hardness following LSM treatment may have been driven more substantially by the increase in the fraction of crystalline precipitates rather than by residual compressive residual stress. As reported earlier, the influence of the microstructure was also observed by Tariq et al. (2009), Mudry et al. (2013), and Huang et al. (2019), albeit in the laser ablation regime for these former studies. Such a correlation was also found here as the hardened surface exhibited a more prominent $CuZr_2$ phase and the introduction of the Al_2NiZr_6 phase as well. With the increase in fluence, the prominence of crystalline precipitates was found to be reduced. As suggested earlier, this might be due to the increased cooling rate during the repeated cycles of irradiation at higher fluence. In addition, it is possible that the more pronounced laser thermal shock events, resulting from the increased fluence, could also have contributed to the reduced hardness via the introduction of shear bands within the material. Thus, in addition to the influence of the tensile residual stress, this could have led to further reduction of the hardness via shear band-induced softening (Huang et al., 2019).

7.4.2. Effect of LSM on the shear banding behaviour of Vitreloy 105

Following laser ablation of the Zr-based BMG Vitreloy 1, Huang et al. (2019) found that laser-induced surface hardening was accompanied by a lack of shear bands reaching the surface during nanoindentation tests. In comparison, such shear bands could still be observed by these authors for as-cast and softened samples. Clearly, a different outcome is observed with the results presented in this chapter as the sample for which LSM led to surface hardening displayed the more pronounced surface shear bands. Huang et al. (2019) suggested that the lack of surface shear band in their case could have been due to the introduced secondary phase which impeded their propagation. In the current study, the higher proportion of crystalline precipitates for the sample in question did not prevent it from also being the specimen with the higher proportion of shear bands reaching the surface. The discrepancy between this outcome and that of Huang et al. (2019) is explained by the role that the measured compressive residual stress should play in the present study. In particular, based on nanoindentation tests conducted on Cu-Zr-based BMG beams pre-stressed elastically, Haag et al. (2014) reported that compressive residual stress could lead to a confined plastic deformation zone, increased material flow towards or at the sample surface and also higher pile-ups around indents. These authors also noted that, with tensile residual stress, no shear steps were found on the BMG surface following nanoindentation. Figure 7.10, which is reproduced and adapted from these authors, illustrates this effect. Figure 7.10(b) in particular shows how compressive residual stress can lead to shear band activity being localised near the surface around the indent. The results presented here are also consistent with these findings from Haag et al. (2014) when the effect of residual stress is considered. In addition, similarly to these authors, higher pile-ups were also associated with the presence of compressive residual stress while

a relatively smooth surface and lower pile-ups around the indents was observed for the sample exhibiting tensile residual stress (see Figure 7.8).

However, one particular experimental result from the current study, which is different from the data presented by Haag et al. (2014) is concerned with the observed serration behaviour between the as-cast sample and the specimen with compressive residual stress. Indeed, these authors found that both compressive and tensile residual stress led to an increase in the total serration length during nanoindentation when compared to the behaviour of the as-cast sample. This particular outcome was only verified here in the case of the specimen with tensile residual stress. Indeed, the sample displaying compressive residual stress showed a reduced overall distance of serrated flows (see Table 7.2). It is suggested that this discrepancy with Haag et al. (2014) could be due to the difference in microstructure between the as-cast and LSMed samples in the current study. Indeed, it seems reasonable to suggest that the higher fraction of crystalline precipitates following LSM at the lowest fluence of 3.42 J/cm^2 impeded the propagation of shear bands and thus, led to a reduction of the measured total length of serrated flow events.

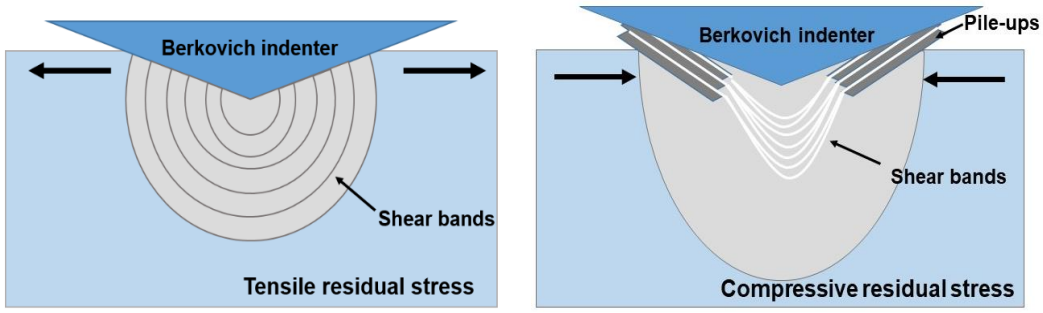

(a) (b)

Figure 7.10: Schematic diagram illustrating the influence of residual stress on the shear banding behaviour of the BMG: (a) tensile residual stress; (b) compressive residual stress. Figure adapted from Haag et al. (2014)

7.5 Conclusions

In this chapter, nanosecond laser surface melting operations in ambient atmosphere were conducted to modify the hardness and the shear banding behaviour of Vitreloy 105. The Vickers micro-hardness and the residual stress on sample surfaces treated with different laser parameters were assessed. Moreover, the resulting microstructure on different irradiated surfaces was studied via X-ray diffraction and scanning electron microscopy. Finally, nanoindentation tests were conducted to evaluate the shear banding activity of the samples, while AFM and SEM were employed to characterise the residual indent morphology. Based on the obtained experimental results, the following conclusions can be made:

1. It was demonstrated that laser surface melting can not only soften the material but also harden it, depending on the applied laser parameters. Among the parameters considered here, the laser fluence appeared to have the most prominent effect on the micro-hardness compared to the scanning speed and the number of irradiation cycles.

2. For a fixed value of scanning speed and irradiation cycle, surface hardening was achieved with the lowest laser fluence considered. This outcome was accompanied with the introduction of compressive residual stress and an increased proportion of crystalline precipitates on the surface of the BMG. Based on the analysis of relevant literature, it may be possible that the increase in the crystalline fraction was the more important driving mechanism behind the observed hardening effect. In addition, with the introduction of compressive residual stress following LSM, overall reduced serrated flow but increased surface shear bands suggest that plastic deformation underneath the indenter became a highly localised activity.

3. For a fixed value of scanning speed and irradiation cycle, the well-known surface softening effect was achieved for higher values of laser fluence. In this case, the presence of tensile residual stress and a reduction in the fraction of crystalline phases were also observed. The introduction of tensile residual stress post-LSM operations promoted serrated flows and the likely distribution of shear banding activity well throughout the volume beneath the indenter.

Chapter 8 Conclusions and Future Work

This chapter presents the main contributions of the research conducted in this thesis and suggests directions for the future work.

8.1 Conclusions

This work was concerned with investigating the utilisation of laser processing techniques, including laser micromachining, laser surface texturing and laser surface melting, on Vitreloy 105 with a view to study whether this combination of process and material could be employed to promote the potential orthopaedic implant applications of this Zr-based bulk metallic glass. The main high-level contributions of this research are as follow:

i) Development of a theoretical model for laser micromachining of Vitreloy 105 in single pulse and multiple moving pulse machining scenarios;

ii) Exploitation of the ns laser surface texturing to modify the surface wettability of Vitreloy 105;

iii) Implementation of laser surface texturing to enhance the bio-compatibility of Vitreloy 105;

vi) Experimental insight into the underlying mechanisms associated with laser surface melting which lead to changes in hardness and shear banding behaviour of irradiated Vitreloy 105 surfaces.

More specific contributions and associated conclusions achieved are given below in light of the knowledge gaps identified in Chapter 2.

Knowledge gap: Investigations in nanosecond laser micromachining on Vitreloy 105 via a combined experimental and theoretical study.

- A 2D theoretical model was created to analyse the temporal and spatial evolution of the temperature on the surface, and within, the target material. This model was also used to predict the thermal history of the BMG specimens and the dimensions of machined craters when processed under different laser parameters so that the underlying removal mechanism and the influence of laser parameters during the laser machining could be revealed.
- The material response during single and multiple pulse processing was investigated under different parameters both theoretically and experimentally; The possible thermal processes on the BMG surface irradiated by single pulse with different pulse durations were studied and it was found that a reduced pulse duration led to a slight decrease in diameter of the melted region, which was attributed to reduced heating time provided by the shorter pulse. On the other hand, the corresponding heating and cooling rate of the short pulse is relatively high, which can be used for the microstructure modification of BMGs. In addition, the effects of laser fluence on the single crater size, and scanning speed on the groove size, and track distance on the material removal rate for the cavity machining were also analysed. In the micromachining scenario considered, it was found that the evolution of the material removal rate, for the fluence and pulse duration values identified, was dominated by the processing time rather than by variation in the volume of removed material.

Knowledge gap: Investigations in the fabrication of surface patterns for wettability modification on Vitreloy 105 by nanosecond laser surface texturing.

- Nanosecond laser surface texturing was successfully used to modify the surface wettability of Vitreloy 105, as a function of fabricated surface patterns, i.e. dimples and grooves, and selected process parameters;
- The effect of distance between two consecutive grooves or craters on the surface roughness of groove patterned or dimple patterned surface could be neglected. However, the scanning speed had a great influence on the surface roughness of the groove textured sample, while the laser fluence also affected the dimple textured surface roughness significantly;
- An important conclusion drawn from the results is that the surface hydrophilicity of the as-cast Vitreloy 105 surface could be enhanced by laser-induced groove patterns while deteriorated by the laser-induced dimple patterns. This enhanced hydrophilicity by the laser-induced groove patterns is generally in line with former reports where laser texturing was applied to other types of metallic materials;
- Based on 3D surface measurements and XPS data, it is suggested that, the enhanced hydrophilicity of the groove patterns is a result of the dominant role played by the laser-induced large surface roughness;
- In contrast, the reduced hydrophilicity observed following the laser texturing of dimple patterns is attributed to the more dominant role that surface chemistry modification plays in this case, and in particular, to the reduction of the hydrophilic carbonyl bonds (C=O) and carboxyl species (O=C-O).

Knowledge gap: Demonstration that laser surface texturing can be exploited to enhance the bio-compatibility of Zr-based BMGs.

- It was found that the laser-induced groove pattern could improve the viability of MG63 cells as well as their attachment on the irradiated Vitreloy 105 surface, and also guide their alignment;

- The enhanced bio-compatibility of the groove textured surface is attributed to the combined effects of LST-induced rough surface, improved hydrophilicity and also the increased presence of metallic oxides, which included TiO_2, Al_2O_3 and ZrO_2, on the surface of laser irradiated areas;
- Laser surface texturing with groove patterns was demonstrated to be a promising technique to improve the bio-compatibility of the Vitreloy 105 BMG;
- The obtained bio-compatibility results agreed well with the assessed wettability of the Vitreloy 105 surfaces.

Knowledge gap: Investigations in hardness, residual stress distribution, shear banding behaviour and microstructure evolution of Vitreloy 105 after laser surface melting.

- Nanosecond laser surface melting in ambient atmosphere was successfully exploited to modify the mechanical properties and microstructure of Vitreloy 105. It was found that laser surface melting not only can soften, as was already known, but also harden the surface layer of Vitreloy 105, depending on the applied laser parameters, especially the laser fluence;
- It was found that, for a fixed value of scanning speed and irradiation cycle, compressive residual stress and an increased proportion of crystalline precipitates were introduced using the lowest laser fluence and that this also corresponded to conditions leading to the hardening of the sample surface;
- In addition, with the introduction of compressive residual stress following LSM, the observation of overall reduced serrated flow but increased surface shear bands suggest that plastic deformation underneath the indenter became a highly localised activity;

- In contrast, laser surface melting with a higher fluence induced tensile residual stress and a reduction in the fraction of crystalline phases. This processing condition also resulted in the softening of the sample surface. The introduction of tensile residual stress post-LSM operations promoted serrated flows and the likely distribution of shear banding activity well throughout the volume beneath the indenter.

8.2 Future work

Based on the research investigations reported in this Thesis, several potential directions for future work have been identified as follows:

1. As discussed in Chapter 4, the recoil pressure and surface tension force caused by the viscous nature of the molten material have not been taken into account in the developed thermal model although they should affect the shape and dimensions of laser-machined craters. In order to improve the accuracy of the simulations, one possible avenue of further research is to introduce the fluid-solid interaction to the current model.
2. Investigations in the bio-corrosion behaviour and in the *in-vivo* bio-compatibility of the laser textured Vitreloy 105 should be further explored. Bio-corrosion behaviour determines the service life of orthopaedic implants for the long-term use. *In-vivo* animal tests are indispensable prior to clinical tests.
3. The evolution of free volume is also an important factor that can affect the mechanical and electrochemical properties of the BMGs. Therefore, further investigations on the free volume evolution of Vitreloy 105 before and after laser surface melting should be conducted.

Bibliography

Andrade, J.D., Smith, L.M., Gregonis, D.E., 1985. The contact angle and interface energetics, Surface and interfacial aspects of biomedical polymers. Springer, pp. 249-292.

Anselme, K., Bigerelle, M., Noel, B., Iost, A., Hardouin, P., 2002. Effect of grooved titanium substratum on human osteoblastic cell growth. Journal of Biomedical Materials Research: An Official Journal of The Society for Biomaterials, The Japanese Society for Biomaterials, and The Australian Society for Biomaterials and the Korean Society for Biomaterials 60, 529-540.

Ashby, M., Greer, A., 2006. Metallic glasses as structural materials. Scripta Materialia 54, 321-326.

Baier, R., Meyer, A., Natiella, J., Natiella, R., Carter, J., 1984. Surface properties determine bioadhesive outcomes: methods and results. Journal of Biomedical Materials Research 18, 337-355.

Bian, Z., Chen, G., He, G., Hui, X., 2001. Microstructure and ductile–brittle transition of as-cast Zr-based bulk glass alloys under compressive testing. Materials Science and Engineering: A 316, 135-144.

Bian, Z., Pan, M.X., Zhang, Y., Wang, W.H., 2002. Carbon-nanotube-reinforced $Zr_{52.5}Cu_{17.9}Ni_{14.6}Al_{10}Ti_5$ bulk metallic glass composites. Applied Physics Letters 81, 4739-4741.

Bizi-Bandoki, P., Valette, S., Audouard, E., Benayoun, S., 2013. Time dependency of the hydrophilicity and hydrophobicity of metallic alloys subjected to femtosecond laser irradiations. Applied Surface Science 273, 399-407.

Boyan, B.D., Hummert, T.W., Dean, D.D., Schwartz, Z., 1996. Role of material surfaces in regulating bone and cartilage cell response. Biomaterials 17, 137-146.

Cai, Y., Chang, W., Luo, X., Sousa, A.M.L., Lau, K.H.A., Qin, Y., 2018. Superhydrophobic structures on 316L stainless steel surfaces machined by nanosecond pulsed laser. Precision Engineering 52, 266-275.

Cao, Y., Xie, X., Antonaglia, J., Winiarski, B., Wang, G., Shin, Y.C., Withers, P.J., Dahmen, K.A., Liaw, P.K., 2015. Laser shock peening on zr-based bulk metallic glass and its effect on plasticity: experiment and modeling. Sci Rep 5, 10789.

Cassie, A., Baxter, S., 1944. Wettability of porous surfaces. Transactions of the Faraday Society 40, 546-551.

Chen, B., Li, Y., Yi, M., Li, R., Pang, S., Wang, H., Zhang, T., 2012. Optimization of mechanical properties of bulk metallic glasses by residual stress adjustment using laser surface melting. Scripta Materialia 66, 1057-1060.

Chen, B., Pang, S., Han, P., Li, Y., Yavari, A.R., Vaughan, G., Zhang, T., 2010. Improvement in mechanical properties of a Zr-based bulk metallic glass by laser surface treatment. Journal of Alloys and Compounds 504, S45-S47.

Chen, J., Mwenifumbo, S., Langhammer, C., McGovern, J.P., Li, M., Beye, A., Soboyejo, W., 2007. Cell/surface interactions and adhesion on Ti-6Al-4V: Effects of surface texture. Journal of Biomedical Materials Research Part B: Applied Biomaterials: An Official Journal of The Society for Biomaterials, The Japanese Society for Biomaterials, and The Australian Society for Biomaterials and the Korean Society for Biomaterials 82, 360-373.

Chen, J., Ulerich, J., Abelev, E., Fasasi, A., Arnold, C.B., Soboyejo, W., 2009. An investigation of the initial attachment and orientation of osteoblast-like cells on laser grooved Ti-6Al-4V surfaces. Materials Science and Engineering: C 29, 1442-1452.

Chen, L.Y., Ge, Q., Qu, S., Jiang, J.Z., 2008. Stress-induced softening and hardening in a bulk metallic glass. Scripta Materialia 59, 1210-1213.

Chen, M., 2011. A brief overview of bulk metallic glasses. NPG Asia Materials 3, 82-90.

Chen, Q., Thouas, G.A., 2015. Metallic implant biomaterials. Materials Science and Engineering: R: Reports 87, 1-57.

Chen, Y.C., Chu, J.P., Jang, J.S.C., Hsieh, C.W., Yang, Y., Li, C.L., Chen, Y.M., Jeng, J.Y., 2013. Replication of nano/micro-scale features using bulk metallic glass mold prepared by femtosecond laser and imprint processes. Journal of Micromechanics and Microengineering 23, 035030.

Cheng, Y., Pang, S., Chen, C., Zhang, T., 2016a. Size-dependent enhancement of plasticity by laser surface melting in $Zr_{55}Al_{10}Ni_5Cu_{30}$ bulk metallic glass. Journal of Alloys and Compounds 658, 49-54.

Cheng, Y., Pang, S., Chen, C., Zhang, T., 2016b. Tensile plasticity in monolithic bulk metallic glass with sandwiched structure. Journal of Alloys and Compounds 688, 724-728.

Chesmel, K., Clark, C., Brighton, C., Black, J., 1995. Cellular responses to chemical and morphologic aspects of biomaterial surfaces. II. The biosynthetic and migratory response of bone cell populations. Journal of biomedical materials research 29, 1101-1110.

Chrzanowski, W., Neel, E.A.A., Armitage, D.A., Knowles, J.C., 2008. Effect of surface treatment on the bioactivity of nickel–titanium. Acta Biomaterialia 4, 1969-1984.

Costa, H., Hutchings, I., 2007. Hydrodynamic lubrication of textured steel surfaces under reciprocating sliding conditions. Tribology International 40, 1227-1238.

Cunha, A., Elie, A.-M., Plawinski, L., Serro, A.P., Botelho do Rego, A.M., Almeida, A., Urdaci, M.C., Durrieu, M.-C., Vilar, R., 2016. Femtosecond laser surface texturing of titanium as a method to reduce the adhesion of Staphylococcus aureus and biofilm formation. Applied Surface Science 360, 485-493.

Demetriou, M.D., Johnson, W.L., 2004. Modeling the transient flow of undercooled glass-forming liquids. Journal of Applied Physics 95, 2857-2865.
Demetriou, M.D., Wiest, A., Hofmann, D.C., Johnson, W.L., Han, B., Wolfson, N., Wang, G., Liaw, P.K., 2010. Amorphous metals for hard-tissue prosthesis. JOM 62, 83-91.
Eberl, C., 2019. Digital Image Correlation and Tracking - File Exchange - MATLAB Central.
Ebnesajjad, S., Ebnesajjad, C., 2013. Surface treatment of materials for adhesive bonding. William Andrew.
Etsion, I., 2005. State of the art in laser surface texturing. J. Trib. 127, 248-253.
Fasasi, A.Y., Mwenifumbo, S., Rahbar, N., Chen, J., Li, M., Beye, A.C., Arnold, C.B., Soboyejo, W.O., 2009. Nano-second UV laser processed micro-grooves on Ti6Al4V for biomedical applications. Materials Science and Engineering: C 29, 5-13.
Fu, J., Zhu, Y., Zheng, C., Liu, R., Ji, Z., 2016. Effect of laser shock peening on the compressive deformation and plastic behavior of Zr-based bulk metallic glass. Optics and Lasers in Engineering 86, 53-61.
Fucheng Li, J.G., Min Song, Song Ni, Shengfeng Guo, 2014. The evolution of local mechanical properties of bulk metallic glasses caused by structural inhomogeneity. Journal of Alloys and Compounds 591, 315-319.
Fucheng Li, M.S., Song Ni, Shengfeng Guo, Xiaozhou Liao, 2016. Correlation between hardness and shear banding of metallic glasses under nanoindentation. Material science and engineering A 657, 38-42.
Gao, M., Dong, J., Huan, Y., Wang, Y.T., Wang, W.-H., 2016. Macroscopic tensile plasticity by scalarizating stress distribution in bulk metallic glass. Scientific reports 6, 21929.
Gasper, A.N.D., Szost, B., Wang, X., Johns, D., Sharma, S., Clare, A., Ashcroft, I., 2018. Spatter and oxide formation in laser powder bed fusion of Inconel 718. Additive Manufacturing 24, 446-456.
Glade, S.C., Busch, R., Lee, D.S., Johnson, W.L., Wunderlich, R.K., Fecht, H.J., 2000. Thermodynamics of $Cu_{47}Ti_{34}Zr_{11}Ni_8$, $Zr_{52.5}Cu_{17.9}Ni_{14.6}Al_{10}Ti_5$ and $Zr_{57}Cu_{15.4}Ni_{12.6}Al_{10}Nb_5$ bulk metallic glass forming alloys. Journal of Applied Physics 87, 7242-7248.
Golovin, Y.I., Ivolgin, V., Khonik, V., Kitagawa, K., Tyurin, A., 2001. Serrated plastic flow during nanoindentation of a bulk metallic glass. Scripta Materialia 45, 947-952.
González, S., Fornell, J., Pellicer, E., Suriñach, S., Baró, M.D., Greer, A.L., Belzunce, F.J., Sort, J., 2013. Influence of the shot-peening intensity on the structure and near-surface mechanical properties of $Ti_{40}Zr_{10}Cu_{38}Pd_{12}$ bulk metallic glass. Applied Physics Letters 103, 211907.
Greer, A., Rutherford, K., Hutchings, I., 2002. Wear resistance of amorphous alloys and related materials. International Materials Reviews 47, 87-112.
Gu, D., Hagedorn, Y.-C., Meiners, W., Meng, G., Batista, R.J.S., Wissenbach, K., Poprawe, R., 2012. Densification behavior, microstructure evolution, and wear

performance of selective laser melting processed commercially pure titanium. Acta Materialia 60, 3849-3860.
Haag, F., Beitelschmidt, D., Eckert, J., Durst, K., 2014. Influences of residual stresses on the serrated flow in bulk metallic glass under elastostatic four-point bending – A nanoindentation and atomic force microscopy study. Acta Materialia 70, 188-197.
Hallab, N., Jacobs, J., Katz 2nd, J., 2004. In Biomaterials Science, ; Ratner, BD; Hoffman, AS; Schoen, FJ; Lemons, JE, Eds. Elsevier Academic Press: San Diego.
Hallab, N.J., Bundy, K.J., O'Connor, K., Moses, R.L., Jacobs, J.J., 2001. Evaluation of metallic and polymeric biomaterial surface energy and surface roughness characteristics for directed cell adhesion. Tissue engineering 7, 55-71.
Hitz, C.B., Ewing, J.J., Hecht, J., 2012. Introduction to laser technology. John Wiley & Sons.
Horton, J., Parsell, D., 2002. Bulk metallic glass medical instruments, implants, and methods of using same. US Patent.
Hsiao, W.-T., Chang, H.-C., Nanci, A., Durand, R., 2016. Surface microtexturing of Ti–6Al–4V using an ultraviolet laser system. Materials & Design 90, 891-895.
Hua, N., Huang, L., Wang, J., Cao, Y., He, W., Pang, S., Zhang, T., 2012. Corrosion behavior and in vitro biocompatibility of Zr–Al–Co–Ag bulk metallic glasses: an experimental case study. Journal of Non-Crystalline Solids 358, 1599-1604.
Huang, H.-H., Sun, Y.-S., Wu, C.-P., Liu, C.-F., Liaw, P.K., Kai, W., 2012a. Corrosion resistance and biocompatibility of Ni-free Zr-based bulk metallic glass for biomedical applications. Intermetallics 30, 139-143.
Huang, H., Jiang, M., Yan, J., 2018. Softening of Zr-based metallic glass induced by nanosecond pulsed laser irradiation. Journal of Alloys and Compounds 754, 215-221.
Huang, H., Jiang, M., Yan, J., 2019. The coupling effects of laser thermal shock and surface nitridation on mechanical properties of Zr-based metallic glass. Journal of Alloys and Compounds 770, 864-874.
Huang, H., Jun, N., Jiang, M., Ryoko, M., Yan, J., 2016. Nanosecond pulsed laser irradiation induced hierarchical micro/nanostructures on Zr-based metallic glass substrate. Materials & Design 109, 153-161.
Huang, H., Yan, J., 2017. Surface patterning of Zr-based metallic glass by laser irradiation induced selective thermoplastic extrusion in nitrogen gas. Journal of Micromechanics and Microengineering 27, 075007.
Huang, H., Zhao, H., Zhang, Z., Yang, Z., Ma, Z., 2012b. Influences of Sample Preparation on Nanoindentation Behavior of a Zr-Based Bulk Metallic Glass. Materials (Basel) 5, 1033-1039.
Huang, L., Cao, Z., Meyer, H.M., Liaw, P.K., Garlea, E., Dunlap, J.R., Zhang, T., He, W., 2011. Responses of bone-forming cells on pre-immersed Zr-based bulk metallic glasses: Effects of composition and roughness. Acta Biomater 7, 395-405.

Huang, L., Pu, C., Fisher, R.K., Mountain, D.J., Gao, Y., Liaw, P.K., Zhang, W., He, W., 2015. A Zr-based bulk metallic glass for future stent applications: Materials properties, finite element modeling, and in vitro human vascular cell response. Acta Biomater 25, 356-368.

Huang, L., Qiao, D., Green, B.A., Liaw, P.K., Wang, J., Pang, S., Zhang, T., 2009. Bio-corrosion study on zirconium-based bulk-metallic glasses. Intermetallics 17, 195-199.

Huerta-Murillo, D., García-Girón, A., Romano, J., Cardoso, J., Cordovilla, F., Walker, M., Dimov, S., Ocaña, J., 2019. Wettability modification of laser-fabricated hierarchical surface structures in Ti-6Al-4V titanium alloy. Applied Surface Science 463, 838-846.

Igarashi, K., Afrashtehfar, K.I., 2018. Clinical assessment of fractured implant abutment screws: The Bernese silicone replica technique. The Journal of prosthetic dentistry 119, 717-719.

Inoue, A., Zhang, T., Masumoto, T., 1989. Zr–Al–Ni Amorphous Alloys with High Glass Transition Temperature and Significant Supercooled Liquid Region. materials transactions 31, 177-183.

Iyengar, V.V., Nayak, B.K., Gupta, M.C., 2010. Ultralow reflectance metal surfaces by ultrafast laser texturing. Applied optics 49, 5983-5988.

Jiang, M.Q., Wei, Y.P., Wilde, G., Dai, L.H., 2015. Explosive boiling of a metallic glass superheated by nanosecond pulse laser ablation. Applied Physics Letters 106, 021904.

Junker, R., Dimakis, A., Thoneick, M., Jansen, J.A., 2009. Effects of implant surface coatings and composition on bone integration: a systematic review. Clinical oral implants research 20, 185-206.

Kaiser, R., Williamson, K., O'Brien, C., Ramirez-Garcia, S., Browne, D., 2015. Effects of hot isostatic pressing and heat treatment on cast cobalt alloy. Materials Science and Technology 31, 1298-1304.

Kannatey-Asibu Jr, E., 2009. Principles of laser materials processing. John Wiley & Sons.

Kietzig, A.-M., Hatzikiriakos, S.G., Englezos, P., 2009. Patterned superhydrophobic metallic surfaces. Langmuir 25, 4821-4827.

Kolev, N.I., 2011. Thermo-physical properties for severe accident analysis, Multiphase Flow Dynamics 5. Springer, pp. 617-807.

Korsunsky, A.M., Sui, T., Salvati, E., George, E.P., Sebastiani, M., 2016. Experimental and modelling characterisation of residual stresses in cylindrical samples of rapidly cooled bulk metallic glass. Materials & Design 104, 235-241.

Kumari, R., Scharnweber, T., Pfleging, W., Besser, H., Majumdar, J.D., 2015. Laser surface textured titanium alloy (Ti–6Al–4V) – Part II – Studies on bio-compatibility. Applied Surface Science 357, 750-758.

Kuriakose, S., Patowari, P.K., Bhatt, J., 2017. Machinability study of Zr-Cu-Ti metallic glass by micro hole drilling using micro-USM. Journal of Materials Processing Technology 240, 42-51.

Lee, B.E., Exir, H., Weck, A., Grandfield, K., 2018. Characterization and evaluation of femtosecond laser-induced sub-micron periodic structures generated on titanium to improve osseointegration of implants. Applied Surface Science 441, 1034-1042.

Li, B.-j., Li, H., Huang, L.-j., Ren, N.-f., Kong, X., 2016. Femtosecond pulsed laser textured titanium surfaces with stable superhydrophilicity and superhydrophobicity. Applied Surface Science 389, 585-593.

Li, H., Zheng, Y., Xu, F., Jiang, J., 2012. In vitro investigation of novel Ni free Zr-based bulk metallic glasses as potential biomaterials. Materials Letters 75, 74-76.

Li, H.F., Xie, X.H., Zhao, K., Wang, Y.B., Zheng, Y., Wang, W., Qin, L., 2013a. In vitro and in vivo studies on biodegradable CaMgZnSrYb high-entropy bulk metallic glass. Acta Biomaterialia 9, 8561-8573.

Li, H.F., Zheng, Y.F., 2016. Recent advances in bulk metallic glasses for biomedical applications. Acta Biomater 36, 1-20.

Li, J., Ai, H.-j., 2014. The responses of endothelial cells to Zr61Ti2Cu25Al12 metallic glass in vitro and in vivo. Materials Science and Engineering: C 40, 189-196.

Li, J., Shi, L.-l., Zhu, Z.-d., He, Q., Ai, H.-j., Xu, J., 2013b. Zr61Ti2Cu25Al12 metallic glass for potential use in dental implants: Biocompatibility assessment by in vitro cellular responses. Materials Science and Engineering: C 33, 2113-2121.

Li, T., Wong, P., Chang, S., Tsai, P., Jang, J., Huang, J., 2017. Biocompatibility study on Ni-free Ti-based and Zr-based bulk metallic glasses. Materials Science and Engineering: C 75, 1-6.

Liaw, P.K., Miller, M.K., 2008. Bulk Metallic Glasses. Springer.

Lin, C., Huang, C., Chuang, J., Lee, H., Liu, M., Du, X., Huang, J., Jang, J., Chen, C., 2012a. Simulated body-fluid tests and electrochemical investigations on biocompatibility of metallic glasses. Materials Science and Engineering: C 32, 2578-2582.

Lin, H.-K., Lee, C.-J., Hu, T.-T., Li, C.-H., Huang, J., 2012b. Pulsed laser micromachining of Mg–Cu–Gd bulk metallic glass. Optics and Lasers in Engineering 50, 883-886.

Lin, X.H., Johnson, W.L., Rhim, W.K., 1997. Effect of oxygen impurity on crystallization of an undercooled bulk glass forming Zr–Ti–Cu–Ni–Al alloy. Materials Transactions 38, 473-477.

Liu, C., Heatherly, L., Horton, J., Easton, D., Carmichael, C., Wright, J., Schneibel, J., Yoo, M., Chen, C., Inoue, A., 1998. Test environments and mechanical properties of Zr-base bulk amorphous alloys. Metallurgical and Materials Transactions A 29, 1811-1820.

Liu, J., 1982. Simple technique for measurements of pulsed Gaussian-beam spot sizes. Optics letters 7, 196-198.

Liu, L., Qiu, C., Chen, Q., Chan, K., Zhang, S., 2008. Deformation behavior, corrosion resistance, and cytotoxicity of Ni-free Zr-based bulk metallic glasses. Journal of Biomedical Materials Research Part A: An Official Journal of The Society

for Biomaterials, The Japanese Society for Biomaterials, and The Australian Society for Biomaterials and the Korean Society for Biomaterials 86, 160-169.
Liu, L., Qiu, C., Chen, Q., Zhang, S., 2006. Corrosion behavior of Zr-based bulk metallic glasses in different artificial body fluids. Journal of Alloys and Compounds 425, 268-273.
Liu, L., Qiu, C., Huang, C., Yu, Y., Huang, H., Zhang, S., 2009. Biocompatibility of Ni-free Zr-based bulk metallic glasses. Intermetallics 17, 235-240.
Liu, W.D., Ye, L.M., Liu, K.X., 2011a. Micro-nano scale ripples on metallic glass induced by laser pulse. Journal of Applied Physics 109, 043109-043109-043105.
Liu, Y., Jiang, M.Q., Yang, G.W., Guan, Y.J., Dai, L.H., 2011b. Surface rippling on bulk metallic glass under nanosecond pulse laser ablation. Applied Physics Letters 99, 191902.
Liu, Y., Wang, Y.-M., Pang, H.-F., Zhao, Q., Liu, L., 2013. A Ni-free ZrCuFeAlAg bulk metallic glass with potential for biomedical applications. Acta Biomaterialia 9, 7043-7053.
Löffler, J.F., 2003. Bulk metallic glasses. Intermetallics 11, 529-540.
Long, M., Rack, H., 1998. Titanium alloys in total joint replacement—a materials science perspective. Biomaterials 19, 1621-1639.
Long, W.J., Nayyar, S., Chen, K.K., Novikov, D., Davidovitch, R.I., Vigdorchik, J.M., 2018. Early aseptic loosening of the Tritanium primary acetabular component with screw fixation. Arthroplasty Today 4, 169-174.
Lunt, A.J., Baimpas, N., Salvati, E., Dolbnya, I.P., Sui, T., Ying, S., Zhang, H., Kleppe, A.K., Dluhoš, J., Korsunsky, A.M., 2015. A state-of-the-art review of micron-scale spatially resolved residual stress analysis by FIB-DIC ring-core milling and other techniques. The Journal of Strain Analysis for Engineering Design 50, 426-444.
Lunt, A.J., Korsunsky, A.M., 2015. A review of micro-scale focused ion beam milling and digital image correlation analysis for residual stress evaluation and error estimation. Surface and Coatings Technology 283, 373-388.
Luo, Y., Zhao, Y., Duan, Y., Du, S., 2011. Surface and wettability property analysis of CCF300 carbon fibers with different sizing or without sizing. Materials & Design 32, 941-946.
Ma, F., Yang, J., XiaonongZhu, Liang, C., Wang, H., 2010. Femtosecond laser-induced concentric ring microstructures on Zr-based metallic glass. Applied Surface Science 256, 3653-3660.
Man, H., Chiu, K., Guo, X., 2010. Laser surface micro-drilling and texturing of metals for improvement of adhesion joint strength. Applied Surface Science 256, 3166-3169.
Meagher, P., O'Cearbhaill, E.D., Byrne, J.H., Browne, D.J., 2016. Bulk Metallic Glasses for Implantable Medical Devices and Surgical Tools. Adv Mater 28, 5755-5762.

Morrison, M., Buchanan, R., Peker, A., Peter, W.H., Horton, J., Liaw, P.K., 2004. Cyclic-anodic-polarization studies of a $Zr_{41.2}Ti_{13.8}Ni_{10}Cu_{12.5}Be_{22.5}$ bulk metallic glass. Intermetallics 12, 1177-1181.

Mudry, S., Nykyruy, Y.S., Kulyk, Y.O., Stotsko, Z., 2013. Influence of pulse laser irradiation on structure and mechanical properties of amorphous $Fe_{73.1}Nb_3Cu_{1.0}Si_{15.5}B_{7.4}$ alloy. Journal of Achievements in Materials and Manufacturing Engineering 61, 7-11.

Mukherjee, S., Dhara, S., Saha, P., 2013. Enhancing the biocompatibility of Ti6Al4V implants by laser surface microtexturing: an in vitro study. The International Journal of Advanced Manufacturing Technology 76, 5-15.

Niinomi, M., 1998. Mechanical properties of biomedical titanium alloys. Materials Science and Engineering: A 243, 231-236.

Noyan, I.C., Cohen, J.B., (2013). Residual stress: measurement by diffraction and interpretation. Springer.

O'Brien, B., Carroll, W., 2009. The evolution of cardiovascular stent materials and surfaces in response to clinical drivers: a review. Acta Biomaterialia 5, 945-958.

Ochsenbein, A., Chai, F., Winter, S., Traisnel, M., Breme, J., Hildebrand, H.F., 2008. Osteoblast responses to different oxide coatings produced by the sol–gel process on titanium substrates. Acta Biomaterialia 4, 1506-1517.

Ohtsu, N., Kozuka, T., Hirano, M., Arai, H., 2015. Electrolyte effects on the surface chemistry and cellular response of anodized titanium. Applied Surface Science 349, 911-915.

Ohtsu, N., Kozuka, T., Yamane, M., Arai, H., 2017. Surface chemistry and osteoblast-like cell response on a titanium surface modified by a focused Nd: YAG laser. Surface and Coatings Technology 309, 220-226.

Owens, D.K., Wendt, R., 1969. Estimation of the surface free energy of polymers. Journal of Applied Polymer Science 13, 1741-1747.

Peker, A., Johnson, W.L., 1993. A highly processable metallic glass: Zr41. 2Ti13. 8Cu12. 5Ni10. 0Be22. 5. Applied Physics Letters 63, 2342-2344.

Pfleging, W., Kumari, R., Besser, H., Scharnweber, T., Majumdar, J.D., 2015. Laser surface textured titanium alloy (Ti–6Al–4V): part 1 – surface characterization. Applied Surface Science 355, 104-111.

Ponsonnet, L., Reybier, K., Jaffrezic, N., Comte, V., Lagneau, C., Lissac, M., Martelet, C., 2003. Relationship between surface properties (roughness, wettability) of titanium and titanium alloys and cell behaviour. Materials Science and Engineering: C 23, 551-560.

Qiu, C., Chen, Q., Liu, L., Chan, K., Zhou, J., Chen, P., Zhang, S., 2006. A novel Ni-free Zr-based bulk metallic glass with enhanced plasticity and good biocompatibility. Scripta Materialia 55, 605-608.

Quintana, I., Dobrev, T., Aranzabe, A., Lalev, G., Dimov, S., 2009. Investigation of amorphous and crystalline Ni alloys response to machining with micro-second and pico-second lasers. Applied Surface Science 255, 6641-6646.

R.Maab, K.S., W.Arnold, and C.A. Volkert, 2014. A single shear band in a metallic glass Local core and wide soft zone. Applied Physics Letters 105.

Rae, T., 1986. The biological response to titanium and titanium-aluminium-vanadium alloy particles: I. tissue culture studies. Biomaterials 7, 30-36.

Raimbault, O., Benayoun, S., Anselme, K., Mauclair, C., Bourgade, T., Kietzig, A.M., Girard-Lauriault, P.L., Valette, S., Donnet, C., 2016. The effects of femtosecond laser-textured Ti-6Al-4V on wettability and cell response. Mater Sci Eng C Mater Biol Appl 69, 311-320.

Ratner, B.D., Hoffman, A.S., Schoen, F.J., Lemons, J.E., 2004. Biomaterials science: an introduction to materials in medicine. Elsevier.

Rautray, T.R., Narayanan, R., Kim, K.-H., 2011. Ion implantation of titanium based biomaterials. Progress in Materials Science 56, 1137-1177.

Ready, J., 1965. Effects due to absorption of laser radiation. Journal of Applied Physics 36, 462-468.

Salvati, E., Lunt, A.J., Sui, T., Korsunsky, A.M., 2015. An investigation of residual stress gradient effects in FIB-DIC micro-ring-core analysis, Proceedings of the International MultiConference of Engineers and Computer Scientists.

Samant, A.N., Dahotre, N.B., 2009. Laser machining of structural ceramics—A review. Journal of the European Ceramic Society 29, 969-993.

Sarapirom, S., Lee, J., Jin, S., Song, D., Yu, L., Han, J., Chaiwong, C., 2013. Wettability effect of PECVD-SiOx films on poly (lactic acid) induced by oxygen plasma on protein adsorption and cell attachment, Journal of Physics: Conference Series. IOP Publishing, p. 012042.

Satriano, C., Carnazza, S., Guglielmino, S., Marletta, G., 2003. Surface free energy and cell attachment onto ion-beam irradiated polymer surfaces. Nuclear Instruments and Methods in Physics Research Section B: Beam Interactions with Materials and Atoms 208, 287-293.

Schrader, M.E., 1981. On adhesion of biological substances to low energy solid surfaces. J. Colloid Interface Sci. 88, 296-297.

Schroers, J., Kumar, G., Hodges, T.M., Chan, S., Kyriakides, T.R., 2009. Bulk metallic glasses for biomedical applications. JOM 61, 21-29.

Schuh, C., Hufnagel, T., Ramamurty, U., 2007. Mechanical behavior of amorphous alloys. Acta Materialia 55, 4067-4109.

Schwarz, F., Wieland, M., Schwartz, Z., Zhao, G., Rupp, F., Geis‐Gerstorfer, J., Schedle, A., Broggini, N., Bornstein, M.M., Buser, D., 2009. Potential of chemically modified hydrophilic surface characteristics to support tissue integration of titanium dental implants. Journal of Biomedical Materials Research Part B: Applied Biomaterials: An Official Journal of The Society for Biomaterials, The Japanese Society for Biomaterials, and The Australian Society for Biomaterials and the Korean Society for Biomaterials 88, 544-557.

Shen, X., Shukla, P., Swanson, P., An, Z., Prabhakaran, S., Waugh, D., Nie, X., Mee, C., Nakhodchi, S., Lawrence, J., 2019. Altering the wetting properties of

orthopaedic titanium alloy (Ti–6Al–7Nb) using laser shock peening. Journal of Alloys and Compounds 801, 327-342.

Steen, W.M., Mazumder, J., 2010. Laser material processing. springer science & business media.

Sun, Y., Huang, Y., Fan, H., Liu, F., Shen, J., Sun, J., Chen, J.J., 2014. Comparison of mechanical behaviors of several bulk metallic glasses for biomedical application. Journal of Non-Crystalline Solids 406, 144-150.

Ta, D.V., Dunn, A., Wasley, T.J., Kay, R.W., Stringer, J., Smith, P.J., Connaughton, C., Shephard, J.D., 2015. Nanosecond laser textured superhydrophobic metallic surfaces and their chemical sensing applications. Applied Surface Science 357, 248-254.

Tariq, N.H., Hasan, B.A., Akhter, J.I., 2009. Evolution of microstructure in $Zr_{55}Cu_{30}Al_{10}Ni_5$ bulk amorphous alloy by high power pulsed Nd:YAG laser. Journal of Alloys and Compounds 485, 212-214.

Telford, M., 2004. The case for bulk metallic glass. Materials Today 7, 36-43.

Trexler, M.M., Thadhani, N.N., 2010. Mechanical properties of bulk metallic glasses. Progress in Materials Science 55, 759-839.

Tsai, P., Lin, Y., Li, J., Jian, S., Jang, J., Li, C., Chu, J., Huang, J., 2012. Sharpness improvement of surgical blade by means of ZrCuAlAgSi metallic glass and metallic glass thin film coating. Intermetallics 31, 127-131.

Vella, P.C., Dimov, S.S., Brousseau, E., Whiteside, B.R., 2014. A new process chain for producing bulk metallic glass replication masters with micro- and nano-scale features. The International Journal of Advanced Manufacturing Technology 76, 523-543.

Vogler, E.A., 1998. Structure and reactivity of water at biomaterial surfaces. Advances in Colloid and Interface Science 74, 69-117.

Vora, H.D., Rajamure, R.S., Soundarapandian, S., Srinivasan, S., Dahotre, N.B., 2013. Dilution of molybdenum on aluminum during laser surface alloying. Journal of Alloys and Compounds 570, 133-143.

Wahab, J., Ghazali, M.J., Yusoff, W.M.W., Sajuri, Z., 2016. Enhancing material performance through laser surface texturing: a review. Transactions of the IMF 94, 193-198.

Wang, C., Zeng, X., 2007. Study of laser carving three-dimensional structures on ceramics: Quality controlling and mechanisms. Optics & Laser Technology 39, 1400-1405.

Wang, J.Y., Wicklund, B.H., Gustilo, R.B., Tsukayama, D.T., 1997. Prosthetic metals interfere with the functions of human osteoblast cells in vitro. Clinical Orthopaedics and Related Research 339, 216-226.

Wang, L., Bei, H., Gao, Y.F., Lu, Z.P., Nieh, T.G., 2011a. Effect of residual stresses on the hardness of bulk metallic glasses. Acta Materialia 59, 2858-2864.

Wang, L., Wang, L., Nie, Z., Ren, Y., Xue, Y., Zhu, R., Zhang, H., Fu, H., 2016. Evolution of residual stress, free volume, and hardness in the laser shock peened Ti-based metallic glass. Materials & Design 111, 473-481.

Wang, Q., Yang, Y., Jiang, H., Liu, C.T., Ruan, H.H., Lu, J., 2014. Superior tensile ductility in bulk metallic glass with gradient amorphous structure. Sci Rep 4, 4757.
Wang, X., Lu, P., Dai, N., Li, Y., Liao, C., Zheng, Q., Liu, L., 2007. Noncrystalline micromachining of amorphous alloys using femtosecond laser pulses. Materials Letters 61, 4290-4293.
Wang, Y., Zheng, Y., Wei, S., Li, M., 2011b. In vitro study on Zr‐based bulk metallic glasses as potential biomaterials. Journal of Biomedical Materials Research Part B: Applied Biomaterials 96, 34-46.
Waugh, D.G., Lawrence, J., 2010. On the use of CO2 laser induced surface patterns to modify the wettability of poly (methyl methacrylate)(PMMA). Optics and Lasers in Engineering 48, 707-715.
Wenzel, R.N., 1936. Resistance of solid surfaces to wetting by water. Industrial & Engineering Chemistry 28, 988-994.
Williams, E., Brousseau, E.B., 2016. Nanosecond laser processing of Zr41.2Ti13.8Cu12.5Ni10Be22.5 with single pulses. Journal of Materials Processing Technology 232, 34-42.
Williams, E., Lavery, N., 2017. Laser processing of bulk metallic glass: a review. Journal of Materials Processing Technology 247, 73-91.
Wu, G., Li, R., Liu, Z., Chen, B., Li, Y., Cai, Y., Zhang, T., 2012. Induced multiple heterogeneities and related plastic improvement by laser surface treatment in CuZr-based bulk metallic glass. Intermetallics 24, 50-55.
Yang, C.-j., Mei, X.-s., Tian, Y.-l., Zhang, D.-w., Li, Y., Liu, X.-p., 2016. Modification of wettability property of titanium by laser texturing. The International Journal of Advanced Manufacturing Technology 87, 1663-1670.
Yang, Y., Cavin, R., Ong, J.L., 2003. Protein adsorption on titanium surfaces and their effect on osteoblast attachment. Journal of Biomedical Materials Research Part A: An Official Journal of The Society for Biomaterials, The Japanese Society for Biomaterials, and The Australian Society for Biomaterials and the Korean Society for Biomaterials 67, 344-349.
Yang, Y., Kim, K.-H., Ong, J.L., 2005. A review on calcium phosphate coatings produced using a sputtering process—an alternative to plasma spraying. Biomaterials 26, 327-337.
Yang, Z., Tian, Y., Yang, C., Wang, F., Liu, X., 2017. Modification of wetting property of Inconel 718 surface by nanosecond laser texturing. Applied Surface Science 414, 313-324.
Yokoyama, Y., Fujita, K., Yavari, A.R., Inoue, A., 2009. Malleable hypoeutectic Zr–Ni–Cu–Al bulk glassy alloys with tensile plastic elongation at room temperature. Philosophical Magazine Letters 89, 322-334.
Yoo, B.-G., Kim, J.-Y., Jang, J.-i., 2007. Influence of indenter geometry on the deformation behavior of $Zr_{60}Cu_{30}Al_{10}$ bulk metallic glass during nanoindentation. Materials transactions 48, 1765-1769.

Yu, H.B., Shen, X., Wang, Z., Gu, L., Wang, W.H., Bai, H.Y., 2012. Tensile plasticity in metallic glasses with pronounced beta relaxations. Phys Rev Lett 108, 015504.

Yu, Z., Hu, J., Li, K., 2019. Investigating the multiple-pulse drilling on titanium alloy in picosecond laser. Journal of Materials Processing Technology 268, 10-17.

Yu, Z., Yang, G., Zhang, W., Hu, J., 2018. Investigating the effect of picosecond laser texturing on microstructure and biofunctionalization of titanium alloy. Journal of Materials Processing Technology 255, 129-136.

Zhang, L., Pauly, S., Zhu, Z.W., Gemming, T., Fu, H.M., Eckert, J., Zhang, H.F., 2016. Ion milling-induced micrometer-sized heterogeneities and partial crystallization in a TiZrCuFeBe bulk metallic glass. Intermetallics 73, 5-11.

Zhang, Y., Wang, W.H., Greer, A.L., 2006. Making metallic glasses plastic by control of residual stress. Nat Mater 5, 857-860.

Zhu, Y., Fu, J., Zheng, C., Ji, Z., 2016. Effect of nanosecond pulse laser ablation on the surface morphology of Zr-based metallic glass. Optics & Laser Technology 83, 21-27.

Zuo, L., Li, R., Cheng, Y., Meng, M., Zhang, T., Inoue, A., 2018. Influence of laser surface melting treatment on the surface composition and mechanical properties of a $Zr_{65}Al_{7.5}Ni_{10}Cu_{12.5}Ag_5$ bulk metallic glass. Journal of Non-Crystalline Solids 488, 63-68.